Sub-wavelength Grating Components for Silicon-on-insulator Platform

by

Yun Wang

B.Sc., Shenzhen University, 2011
M.ASc., The University of British Columbia, 2013

A DISSERTATION SUBMITTED IN PARTIAL FULFILLMENT OF
THE REQUIREMENTS FOR THE DEGREE OF

DOCTOR OF PHILOSOPHY

in

The Faculty of Graduate and Postdoctoral Studies

(Electrical and Computer Engineering)

THE UNIVERSITY OF BRITISH COLUMBIA

(Vancouver)

December 2016

© Yun Wang 2016

Abstract

This dissertation is a theoretical and experimental study of sub-wavelength grating (SWG) based photonic devices for the silicon-on-insulator (SOI) platform, including high-efficiency sub-wavelength grating couplers (SWGCs), broadband SWGCs, broadband SWG directional couplers, and an SWG polarization splitter-rotator.

High-efficiency SWGCs with improved operating bandwidths and suppressed back reflections have been demonstrated to couple light into and out of SOI based photonic integrated circuits (PICs). One-dimensional SWGs have been proposed and experimentally demonstrated for the first time to make fully-etched grating couplers, which have performances comparable to the state-of-the-art fully-etched grating couplers, but with better fabrication tolerance, reduced fabrication complexity, and less cost.

A theoretical study of the operating bandwidths for grating couplers has been presented and a design methodology has been demonstrated for designing SWGCs with design-intent operating bandwidths. SWGCs with 1-dB bandwidths up to 90 nm have been demonstrated, which have improved the operating bandwidth of fully-etched grating couplers by a factor of 3. Such broadband SWGCs are essential components for applications such as wavelength-division multiplexing (WDM) PICs and bio-sensing.

Compact directional couplers, with dimensions about 10 times smaller

than its alternatives, i.e., adiabatic couplers and multimode interference couplers have been demonstrated for various power splitting ratios. The operating bandwidths of our directional couplers have been improved by a factor of 2 as compared to conventional directional couplers. The dispersion properties of SWGs have been explored and applied to engineer the wavelength dependancy of conventional directional couplers for broad operating bandwidths, which is the first experimental demonstration of such devices.

Polarization splitter and polarization rotators are essential components to address the polarization diversity of PICs. An ultra-compact mode-coupling based polarization splitter-rotator (PSR), which combines functionalities of a polarization splitter and a polarization rotator, with dimensions 15-20 times smaller than its alternative, i.e., mode-evolution based PSRs, has been experimentally demonstrated for the first time, where an asymmetric waveguide system consisting of a strip waveguide and an SWG waveguide were used to improve the fabrication tolerance of such devices. A measured peak polarization conversion efficiency of $-0.3\,\mathrm{dB}$ with crosstalks below $-10\,\mathrm{dB}$ over the C-band has been achieved.

Preface

Parts of the dissertation are based on the author's manuscripts, which have been or will be published, resulting from collaborations with multiple researchers. A complete list of publications is given in Appendix A.

A version of Section 2.1 has been published:

1. Yun Wang, Xu Wang, Jonas Flueckiger, Han Yun, Wei Shi, Richard Bojko, Nicolas A. F. Jaeger, and Lukas Chrostowski, "Focusing subwavelength grating coupler with low back reflections for rapid prototyping of silicon photonic circuits", Optics Express, Vol. 22, Issue 17, pp.20652-20662, 2014

   The author contributed the idea, conducted the devices' design, conducted the measurement, conducted the data processing and analysis, and wrote the manuscript. Xu Wang helped with many discussions on the design methodology. Jonas Flueckiger helped on building the measurement setup. Han Yun helped with the measurement. Wei Shi helped with discussion on the design and assisted in editing the manuscript. Richard Bojko fabricated the design and took SEM pictures of the fabricated devices. Prof. Chrostowski and Prof. Jaeger helped with many suggestions in the course of the project and assisted in editing the manuscript.

   A version of Section 2.2 has been published:

2. Yun Wang, Han Yun, Zeqin Lu, Richard Bojko, Wei Shi, Xu Wang, Jonas Flueckiger, Fan Zhang, Michael Caverley, Nicolas A. F. Jaeger, Lukas Chrostowski, "Apodized focusing fully etched sub-wavelength grating couplers", Photonics Journal, IEEE, Vol. 7, No. 3, 2400110, 2015

   The author contributed the idea, conducted the devices' design, conducted the measurement, conducted the data processing and analysis, and wrote the manuscript. Han Yun and Zeqin Lu helped with discussions on the design. Richard Bojko fabricated the design and took SEM pictures of the fabricated devices. Wei Shi and Xu Wang assisted in editing the manuscript. Jonas Flueckiger helped with the measurement setup. Fan Zhang and Michael Caverley helped with the measurement. Prof. Chrostowski and Prof. Jaeger helped with many suggestions in the course of the project and assisted in editing the manuscript.

   A version of Chapter 3 has been published:

3. Yun Wang, Wei Shi, Xu Wang, Zeqin Lu, Michael Caverley, Richard Bojko, Lukas Chrostowski, and Nicolas A. F. Jaeger, "Design of broadband sub-wavelength grating couplers with low back reflection", Optics Letters, Vol. 40, Issue 20, pp.4647-4650, 2015

   The author contributed the idea, conducted the devices' design, conducted the measurement, conducted the data processing and analysis, and wrote the manuscript. Wei Shi helped with the motivation with the design. Xu Wang helped with the simulation of the design. Zeqin Lu helped with discussion about the design. Michael Caverley helped with the measurement. Richard Bojko fabricated the design and took

SEM pictures of the fabricated devices. Prof. Chrostowski and Prof. Jaeger helped with many suggestions in the course of the project and assisted in editing the manuscript.

A version of Chapter 4 has been published:

4. Yun Wang, Zeqin Lu, Minglei Ma, Han Yun, Fan Zhang, Nicolas A. F. Jaeger, and Lukas Chrostowski, "Compact Broadband Directional Couplers Using Sub-wavelength Gratings," Photonics Journal, IEEE, Vol. 8, Issue 3, 2016

   The author contributed the idea, conducted the devices' design, conducted the measurement, conducted the data processing and analysis, and wrote the manuscript. The author Zeqin Lu and Minelei Ma helped with the mask layout of the design. Han Yun and Fan Zhang helped with the measurement. Prof. Chrostowski and Prof. Jaeger helped with many suggestions in the course of the project and assisted in editing the manuscript.

A version of Chapter 5 has been published:

5. Yun Wang, Minglei Ma, Han Yun, Zeqin Lu, Xu Wang, Nicolas A. F. Jaeger, and Lukas Chrostowski, "Ultra-Compact Sub-Wavelength Grating Polarization Splitter-Rotator for Silicon-on-Insulator Platform," Photonics Journal, IEEE, Vol. 8, Issue 6, 2016

   The author contributed the idea, conducted the devices' design, conducted the measurement, conducted the data processing and analysis, and wrote the manuscript. The author Minelei Ma helped with the mask layout and the measurement. Han Yun helped with the measurement, Zeqin Lu helped with the layout. Xu Wang helped with

the simulation methodology. Prof. Chrostowski contributed on the design methodology. Prof. Chrostowski and Prof. Jaeger helped with many suggestions in the course of the project and assisted in editing the manuscript.

Table of Contents

Abstract ii

Preface iv

Table of Contents viii

List of Tables xi

List of Figures xii

List of Abbreviations xix

Acknowledgements xxi

Dedication xxii

1 Introduction 1

1.1 Silicon Photonics 1

1.1.1 Silicon-on-Insulator 2

1.1.2 Challenges and State of the Art 2

1.2 Sub-wavelength Structures 8

1.2.1 The Sub-wavelength Regime 8

1.2.2 Effective Medium Theory 10

1.2.3 Applications of Sub-wavelength Structures on SOI . . 11

1.3 About This Dissertation 13
1.3.1 Objective 13
1.3.2 Dissertation Organization 13

2 High-Efficiency Fully-etched Sub-wavelength Grating Couplers 16
2.1 Uniform Sub-wavelength Grating Couplers 16
2.1.1 Challenges of Fully-etched Grating Couplers 16
2.1.2 2D SWGs vs. 1D SWGs 18
2.1.3 Design and Simulation 21
2.1.4 Fabrication and Measurement 31
2.2 Apodized Sub-wavelength Grating Couplers 39
2.2.1 Design and Simulation 39
2.2.2 Design of Apodized SWGCs 41
2.2.3 Measurement Results 44

3 Broadband Sub-wavelength Grating Couplers 49
3.1 Bandwidth Analysis 49
3.2 Design Methodology 51
3.3 Measurement Results 56

4 Broadband Sub-wavelength Directional Couplers 61
4.1 Wavelength Dependency of Directional Couplers 62
4.2 Dispersion Engineering 64
4.3 Measurement Results 70

5 Sub-wavelength Polarization Splitter Rotator 76
5.1 Design of SWG PSR 77

5.2 Fabrication and Measurement 85

6 Conclusion and Future Work 88

6.1 Conclusion 88

6.1.1 Technical Contributions 88

6.1.2 Design Methodology Contributions 90

6.1.3 Theoretical Contributions 93

6.2 Future Work 93

Bibliography 97

Appendices

A Publications 113

A.1 Book Chapters 113

A.2 Journal Publications 113

A.3 Conference Proceedings 116

List of Tables

2.1 Simulated and measured sensitivities of the central wavelength as a function of Λ, Λ_{H}, and l_{sub}. 33
2.2 Λ and l_{sub} values for the apodized SWGCs. 41
2.3 Parameters used for corner analysis for SWGCs. 46

3.1 Optimization steps and design parameters 54
3.2 Design variations 57

5.1 Parameter Variations. 85

6.1 Comparison of SWGCs for the SOI platform. CE, coupling efficiency; BW, bandwidth. 90

List of Figures

1.1 Schematic of the cross-section of a silicon-on-insulator wafer. 2

1.2 A schematic of the cross-section of an SOI waveguide with dimensions of 500 nm x 220 nm and an optical fiber with a diameter of 10 µm drawn to scale. 3

1.3 Schematics of (a) a shallow-etched grating coupler and (b) a regular fully-etched grating coupler. 5

1.4 Schematics of (a) an adiabatic coupler, (b) an multimode interference coupler, and (c) a directional coupler. (drawn to scale) 6

1.5 Schematic of a polarization diverse PICs. 7

1.6 Schematic of the cross-section of a periodic waveguide structure. 9

1.7 SEM images of (a) an SWG waveguide, and (b) an SWG waveguide with an SWG waveguide taper. 12

1.8 SEM images of (a) a directional coupler consisting of strip waveguides, and (b) a directional coupler consisting of a strip waveguide and an SWG waveguide. 13

1.9 SEM images of (a) a straight SWGC with two-dimensional SWGs and (b) a focusing SWGC with one-dimensional SWGs. 14

2.1 Measured transmission spectra for a pair of shallow-etched grating couplers and fully-etched grating coupler. 17
2.2 A Schematics of a fully-etched grating couplers with effective index regions. 18
2.3 Schematics of a fully-etched SWGCs with one-dimensional SWGs. 18
2.4 (a) 2D energy distribution of an SWGC formed by two-dimensional SWGs; (b) energy distribution along the 1-D cutline across the 2-D simulation of an SWGC formed by two-dimensional SWGs; (c) 2D energy distribution of an SWGC formed by one-dimensional SWGs; (d) energy distribution along 1-D cutlines across the 2-D simulations of SWGCs formed by one-dimensional SWGs. 20
2.5 Schematic of the cross-section of an SWGC with (a) a positive incident angle and (b) a negative incident angle. 22
2.6 Simulations of SWGCs in *FDTD Solutions.* 24
2.7 Simulated coupling efficiency and back reflection for the TE SWGC and a shallow-etched grating coupler. SWGC-T and SWGC-R denote the coupling efficiency and the back reflection of the optimized TE SWGC, Shallow-T and Shallow-R denote the coupling efficiency and the back reflection of the optimized shallow-etched grating coupler. 25

2.8 The simulated coupling efficiency and the back reflection for the TM SWGC and a shallow-etched grating coupler. SWGC-T and SWGC-R denote the coupling efficiency and the back reflection of the optimized TM SWGC, Shallow-T and Shallow-R denote the coupling efficiency and the back reflection of the optimized shallow-etched grating coupler. 26

2.9 (a) Schematic of the input-waveguide-output circuit in *Interconnect*, and (b) simulated transmission spectra of input-waveguide-ouput circuits for TE and TM SWGCs. 28

2.10 Mask layouts of (a) a grating coupler with straight grating lines and a linear taper, and (b) an SWGC with focusing grating lines. 29

2.11 Schematics for SWGCs with focusing grating lines and (a) positive incident angles, and (b) negative incident angles. . . 30

2.12 SEM images of (a) the top view of a fabricated SWGC and (b) the side view of a fabricated SWGC. 32

2.13 (a) Simulated sensitivities of Λ, Λ_{H}, and l_{sub} for the TE SWGCs; (b) measured sensitivities for the TE SWGCs; (c) simulated sensitivities for the TM SWGCs; (d) measured sensitivities for the TM SWGCs. 34

2.14 Simulated and measured transmission spectra of a fabricated TE SWGC assuming $l_{\mathrm{sub}} = 89$nm; inset is the spectrum near the central wavelength. 36

2.15 (a) Measured spectra of 11 TM SWGCs; (b) comparison of measured and simulated coupling efficiencies of the TM SWGCs; (c) comparison of the measured and simulated 1-dB bandwidths of the TM SWGCs; (d) measured spectra of TM SWGCs with various Λ_{H} values; (e) measured spectra of TM SWGCs with various Λ values; (f) measured spectra of TM SWGCs with various l_{sub} values. 38

2.16 α as functions of l_{sub} and Λ_{H} for the TE SWGCs, and (b) α as functions of l_{sub} and Λ_{H} for the TM SWGCs. 40

2.17 Simulated coupling efficiencies and back reflections of the apodized and the un-apodized (a) TE SWGCs using 2D FDTD simulation, and (b)TM SWGCs using 2D FDTD simulation. . 42

2.18 Simulated transmission spectra of (a) the apodized TE SWGCs, and (b) the apodized TM SWGCs. 43

2.19 (a) Measured spectra of an apodized TE SWGC and an un-apodized TE SWGC; (b) coupling efficiencies of apodized and un-apodized TE SWGCs; (c) 1-dB bandwidths of apodized and un-apodized TM SWGCs; (d) central wavelengths of the apodized and un-apodized TE SWGCs. 45

2.20 (a) Measured spectra of an apodized TM SWGC and an un-apodized TM SWGC; (b) coupling efficiencies of apodized and un-apodized TM SWGCs; (c) 1-dB bandwidths of apodized and un-apodized TM SWGCs; (d) central wavelengths of the apodized and un-apodized TM SWGCs. 47

3.1 Schematic of the cross-section of a broadband SWGC with one-dimensional SWGs. 50

3.2 Optimal incident angle, θ_{opt}, as a function of the group index of a grating coupler, n_{g}. 52
3.3 Schematics of (a) an SWGC with refractive index regions of n_{H} and n_{L}, (b) an SWGC with one-dimensional SWGs. . . . 53
3.4 Simulated transmission and reflection spectra of the SWGC with the design parameters shown in Table 3.1. 55
3.5 Simulated 1-dB bandwidth and peak coupling efficeincy as a function of ff_{L}. 56
3.6 SEM images of the as-fabricated focusing and straight SWGCs. (For the straight SWGC, the taper is not shown.) 57
3.7 Transmission spectra of the simulated SWGC (red), the measured focusing SWGC (blue), and the measured straight SWGC (green). 58
3.8 Measured (a) 1-dB bandwidths and (b) coupling efficiencies of the fabricated focusing SWGCs with ff_L ranging from 0.1 to 0.19; measured (c) 1-dB bandwidths and (d) coupling efficiencies of the fabricated straight SWGCs with ff_L ranging from 0.1 to 0.18. 60

4.1 Schematic of an SWG DC with design parameters labelled. . 62
4.2 Field profiles of (a) the TE_0 mode, and (b) the TE_1 mode for a conventional DC. 63
4.3 (a) n_{eff1} and n_{eff2} as functions of λ for a conventional DC, (b) L_π as a function of λ for a conventional DC. The simulated DC has $w = 450\,\mathrm{nm}$, $g = 220\,\mathrm{nm}$, based on an SOI wafer with a silicon layer of 220 nm. 64
4.4 n_{eff} as a function of λ for an SWG with $\Lambda = 285\,\mathrm{nm}$, $ff = 0.5$. 65

4.5 (a) Schematic of the simulated structure for an SWG DC in *FDTD Solutions*, (b) simulated band diagram for an SWG DC with $\Lambda = 285\,\text{nm}$ and $ff = 0.28$. 66

4.6 (a) Simulated transmission spectra from the cross ports of SWG DCs with $ff = 0.25$, $NG = 47$, and various Λ values, (b) simulated transmission spectra from the cross ports of SWG DCs with $\Lambda = 285\,\text{nm}$, $NG = 47$, and various ff values. 67

4.7 (a) n_{eff1} and n_{eff2} as functions of λ for an SWG DC with $\Lambda = 285\,\text{nm}$ and $ff = 0.28$, (b) calculated L_π as a function of λ based on the n_{neff1} and n_{eff2} shown in (a). 68

4.8 (a) Simulated spectra for an SWG DC with a designed power splitting ratio of 50/50 (η_1 and η_2 are the normalized output power for the cross and through ports, respectively), (b) simulated IL as a function of λ for the SWG DC with a designed power splitting ratio of 50/50. 69

4.9 Simulated ILs as a function of ff for SWG DCs with $\Lambda = 285\,\text{nm}$. 70

4.10 Mask layout of the test structure for SWG DCs. 71

4.11 SEM images of (a) a fabricated SWG DC, (b) a zoom-in of the central portion of the fabricated SWG DC with the design parameters labelled. 73

4.12 (a) Measured spectra for a test structure with SWG DCs which had power splitting ratios close to 50/50, and (b) normalized optical powers for a fabricated SWG DC using the measurement data shown in (a). 74

4.13 Normalized optical powers for fabricated SWG DCs with power splitting ratios of (a) 40/60, (b) 30/70, and (c) 20/80. 75

5.1 Schematic of the top view of an SWG PSR. 78

5.2 $n_{\text{eff-TM}}$ as a function of W_{A} for a strip waveguide and $n_{\text{eff-TE}}$ as a function of W_{B} for an SWG waveguide. 79

5.3 The X and Y field distributions for the first three supermodes. (a) Y component of the E_0^{xy} mode, (b) X component of the E_0^{xy} mode; (c) X component of the E_1^{xy} mode, (d) Y component of the E_1^{xy} mode; (e) X component of the E_2^{xy} mode, (f) Y component of the E_2^{xy} mode. 81

5.4 n_{eff} as a function of λ for the E_1^{xy} and the E_2^{xy} modes of the two waveguide system comprising the coupling section of the SWG PSR. 82

5.5 Schematic of the top view of an SWG taper. 83

5.6 (a) Simulated $\text{IL}_{\text{TE-TE}}$ and $\text{PCE}_{\text{TM-TE}}$ as functions of λ, and (b) simulated $\text{XT}_{\text{TE-TE}}$ and $\text{XT}_{\text{TM-TM}}$ as functions of λ. . . 84

5.7 $\text{PCE}_{\text{TM-TE}}$ as functions of δW_X and $\delta W_{\text{Y-Z}}$. 85

5.8 SEM images of a fabricated SWG PSR with zoomed images of the coupling section, the SWG taper, and the S bend waveguide. 86

5.9 (a) Measured $\text{IL}_{\text{TE-TE}}$ and $\text{PCE}_{\text{TM-TE}}$ as functions of λ, and (b) measured $\text{XT}_{\text{TE-TE}}$ and $\text{XT}_{\text{TM-TM}}$ as functions of λ. . . . 87

6.1 Schematic of the cross-section of an SWGC with sub-wavelength structures comprising both the coupling region and the taper region. 95

List of Abbreviations

BOX	Buried Oxide
CMOS	Complementary Metal-Oxide-Semiconductor
DC	Directional Coupler
EME	Eigen Mode Expansion
EMT	Effective Medium Theory
ER	Extinction Ratio
FDTD	Finite-Difference Time-Domain
FOM	Figure-of-Merit
FSR	Free Spectrum Range
IL	Insertion Loss
MMI	Multimode Interferometer
MPW	Multi-Project Wafer
MZI	Mach Zehnder Interferometer
NA	Numerical Aperture
NG	Number of Grating
PCE	Polarization Conversion Efficiency
PIC	Photonic Integrated Circuit
PM	Polarization Maintaining
PSA	Particle Swarm Algorithm
PSF	Point Spread Function

PSR	Polarization Splitter-Rotator
SEM	Scanning Electron Microscope
SOI	Silicon-on-Insulator
SWG	Sub-Wavelength Grating
SWGC	Sub-Wavelength Grating Coupler
TE	Transverse Electric
TM	Transverse Magnetic
XT	Crosstalk

Acknowledgements

I would like to thank my supervisor Dr. Lukas Chrostowski for guiding me through a fantastic journey that I have enjoyed so much. I want to thank him for supporting me from every aspects he can and providing me with the freedom to do the research that I am interested. To me, he is a passionate researcher, a great supervisor, a talented educator and a good friend.

I would like to thank Dr. Nicolas A. F. Jaeger for the dedicated help he provided through my PhD journey. Part of the most enjoyable time during my PhD was sitting with Dr. Jaeger in his front yard, editing my manuscripts and discussing various research ideas. Beyond the help from the research side, he has been a mentor to me since I joined the photonics research group at UBC. Through out the years, he has shown me what is wisdom, kindness, and generosity.

I would also like to thank all my colleagues that I have been working with for their help and support, especially Dr. Wei Shi, Dr. Xu Wang, and Dr. Jonas Flueckiger.

Dedication

To my familiy.

Chapter 1

Introduction

1.1 Silicon Photonics

Silicon photonics is an emerging technology for building complex photonic integrated circuits (PICs). The great promise of silicon photonics lies in integrating multiple functions into a single package, and manufacturing most or all of them using the same fabrication facilities that are used to build advanced microelectronics, namely the complementary metal-oxide-seminconductor (CMOS) technology, as part of a single chip or chip stack [19]. Historically, photonic devices with different functionalities are designed and fabricated based on different materials, i.e., lithium niobate for high speed modulators, indium phosphide for lasers, germanium for photodectors, glass for optical multiplexers. Though discrete photonic devices can be connected using standard optical fibers, a large fraction of the final device cost emerges from the the photonic packaging processes [19]. Silicon photonics provides the possibility to integrate all of these functionalities into the same platform, which is the silicon-on-insulator (SOI) platform. During the past two decades, various photonic designs at the component level, with competitive performances, have been demonstrated for the SOI platform, including low loss waveguides [63], multiplexers and demultiplexers [67, 76], high-speed electrooptic modulators [61], photodetectors [52], etc.

1.1.1 Silicon-on-Insulator

A schematic of the cross-section of an SOI wafer is shown in Fig. 1.1, which consists of a silicon substrate for mechanical support, a buried oxide (BOX) layer acting as the insulator layer, and another thin silicon layer on top of the BOX where the waveguides and devices are defined. A cladding oxide are normally applied on top of the top silicon layer for protection. The thickness of silicon substrate is about 700 µm, the thickness of the BOX layer is normally between 1 µm to 3 µm, as long as it is thick enough to avoid penetration loss of optical waves from the top silicon layer into the silicon substrate. The thickness of the top silicon layer is about few hundred nanometers and the optimal thickness is application dependent [92]. The designs shown in this dissertation are based on SOI wafers with a 220 nm silicon layer and a 3 µm BOX layer. The thickness of the top silicon layer we used are the same with those provided by the multiple-project wafer (MPW) foundries, such as imec, LETI, IME and IHP [1, 36, 39, 42].

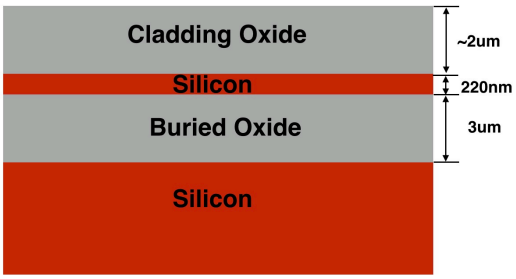

Figure 1.1: Schematic of the cross-section of a silicon-on-insulator wafer.

1.1.2 Challenges and State of the Art

Although significant progress has been achieved, many challenges remain for the silicon photonics community to be solved. Due to the fact that silicon

is an indirect-band semiconductor which is inefficient at light generation, external lasers are often used as the power supplies for the SOI PICs, where optical fibers are often used to couple light into and out of the SOI PICs. Due to the large refractive index contrast between the top silicon layer and its cladding, propagation modes can be highly confined within the waveguides, with cross-sectional dimensions on the order of a few hundred nanometers. However, the small feature sizes of the waveguide raise the problem of large mode mismatch when coupling light from an optical fiber to the sub-micron silicon waveguide core. A schematic of the cross-section of an SOI waveguide and an optical fiber drawn to scale is shown in Fig. 1.2.

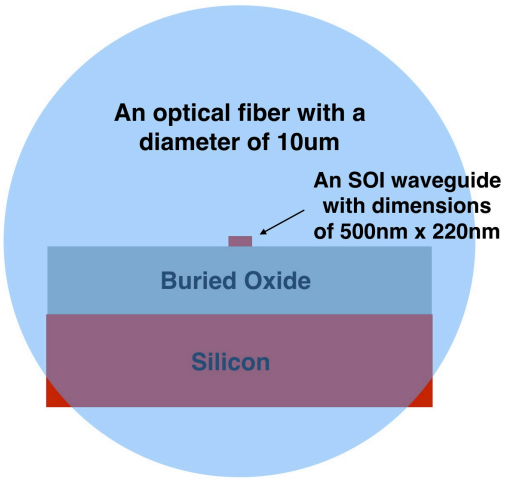

Figure 1.2: A schematic of the cross-section of an SOI waveguide with dimensions of 500 nm x 220 nm and an optical fiber with a diameter of 10 µm drawn to scale.

Edge coupling and surface coupling are the two approaches that have been used to address the mode mismatch issue, and both approaches have demonstrated below 1 dB loss per device [75, 99]. Using edge coupling technique has the advantages of broad operating bandwidth with ultra-low cou-

pling loss. It also couples both the transverse electric (TE) mode and the transverse magnetic (TM) mode at the same time. In addition, using edge coupling technique can take advantages of the mature packaging solution. Compared with the edge coupling technique, surface coupling using grating couplers has the following advantages: firstly, the cost of using grating couplers is lower because post processing of the chip, i.e., deep etching on the edges of chips and edge polishing, and expensive components, i.e., lensed fibers or high numerical aperture (NA) fibers, are not required for the measurement; secondly, grating couplers are easy to align to during measurement; thirdly, grating couplers have more compact design shape and also provide the flexibility to be located anywhere on a chip, which enables better architectural design; last but not least, grating couplers enable wafer-scale automated measurement, without the need to dice the wafer.

Depending on the required etch-steps for fabrication, grating couplers can be divided into shallow-etched grating couplers and fully-etched grating couplers. Schematics of a shallow-etched grating coupler and a fully-etched grating coupler are shown in Fig. 1.3. Coupling efficiency and operating bandwidth are the two most important figures-of-merits (FOMs) for a grating coupler. Both shallow-etched grating couplers and fully-etched grating couplers with coupling efficiencies higher than $-1\,\mathrm{dB}$ have been demonstrated [5, 24, 99]. However, fabricating shallow-etched grating couplers, with various etch depths, increases both the fabrication complexity and the cost. When combining fundamental building blocks that can be fabricated in a single, fully-etched step, having fully-etched grating couplers provides an efficient and economical solution for rapid prototyping. High-efficiency fully-etched grating couplers will be demonstrated in Chapter 2 of this dissertation and fully-etched grating couplers with ultra-broad operating band-

widths will be demonstrated in Chapter 3 of this dissertation.

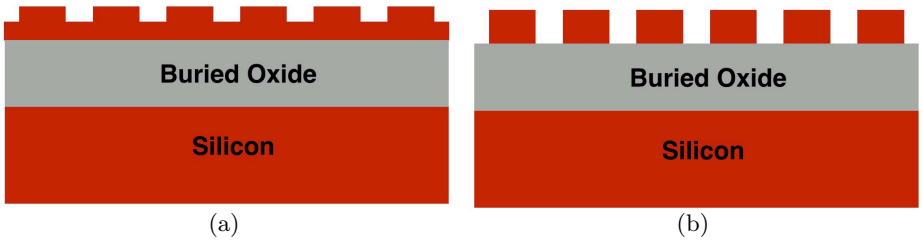

Figure 1.3: Schematics of (a) a shallow-etched grating coupler and (b) a regular fully-etched grating coupler.

Optical couplers are essential for coupling light between waveguides in PICs, which are often used in applications such as wavelength-division-multiplexing [12] and optical switching [2]. Dealing with the dispersion effects in various optical couplers is a great challenge since we are interested in designing devices for a variety of wavelengths, and the wavelength dependence of the devices should be taken into account. There are two sources for the dispersion effects: the material dispersion, i.e., dispersion comes from the material property, and the waveguide dispersion, i.e., dispersion comes from the geometry of the waveguide. Such dispersion effects limit the operating bandwidth of a device. Adiabatic couplers [71, 98], multimode interference (MMI) couplers [48, 70], and directional couplers (DCs) [47, 55] are three types of optical coupler that are often used in PICs, and the schematics of them are shown in Fig. 1.4. Adiabatic couplers have the advantage of broad operating bandwidth, and they have been used to form 3-dB couplers [98] and thermo-optic switches [86]. However, in order to avoid the excitation of higher order modes, the lengths of adiabatic couplers are much longer than MMI couplers and DCs. MMI couplers are shorter than adiabatic couplers, but are much larger than DCs. In addition, MMI based devices are

much less predictable when used for low coupling ratios, i.e., power splitting ratios of 2/98 or 5/95 [21]. Conventional DCs, consisting of two parallel waveguides, are very compact in size, but they are also very sensitive to the wavelength and polarization state of the light. Several methods have been proposed to improve the bandwidths of DCs, such as connecting couplers in a Mach-Zehnder interferometer (MZI)[44], using a plasmonic waveguide to compensate the wavelength dependancy [55], or using cascaded DCs with additional phase shifter [47], but at a cost of increased device footprint, increased fabrication complexity, and increased cost. Compact directional couplers, with a single etch step for fabrication, which have broad operating bandwidths will be demonstrated in Chapter 4 of this dissertation.

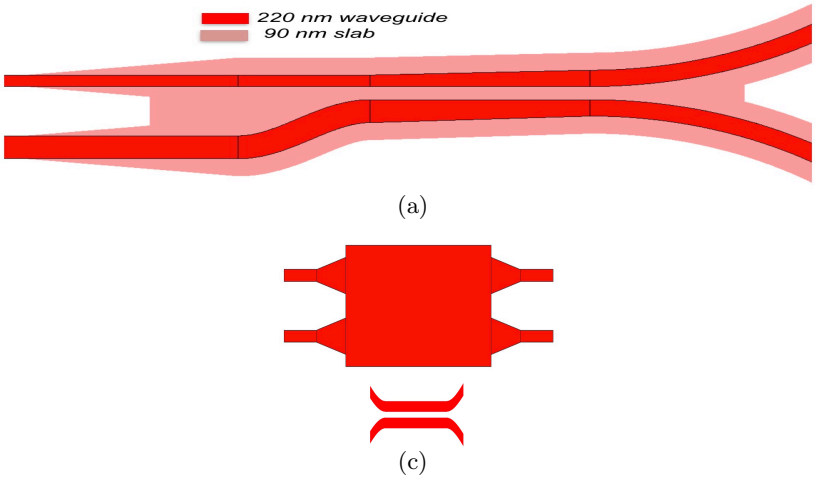

Figure 1.4: Schematics of (a) an adiabatic coupler, (b) an multimode interference coupler, and (c) a directional coupler. (drawn to scale)

Dealing with the polarization is another challenge. The high index contrast and aspect ratio of SOI waveguides result in a large modal birefrin-

gence, which means SOI based photonic devices often behave differently with different polarizations of light. Such birefringence makes SOI PICs incompatible with optical fiber systems that use non-polarization-maintaining, single mode fibers, in which the polarization state of the optical modes at the outputs of the fibers can change randomly. A polarization diversity [3] approach has been demonstrated to address the modal birefringence issue of the SOI PICs, which takes the advantages of polarization splitter [88] and polarization rotator [87]. Recently, polarization splitter-rotators have been demonstrated for the SOI platform [20, 23, 45, 65, 80, 81, 97], which combines the two functionalities, i.e., polarization splitting and polarization rotating, into one device. An ultra-compact polarization splitter-rotator with improved fabrication tolerance will be demonstrated in Chapter 5 of this dissertation.

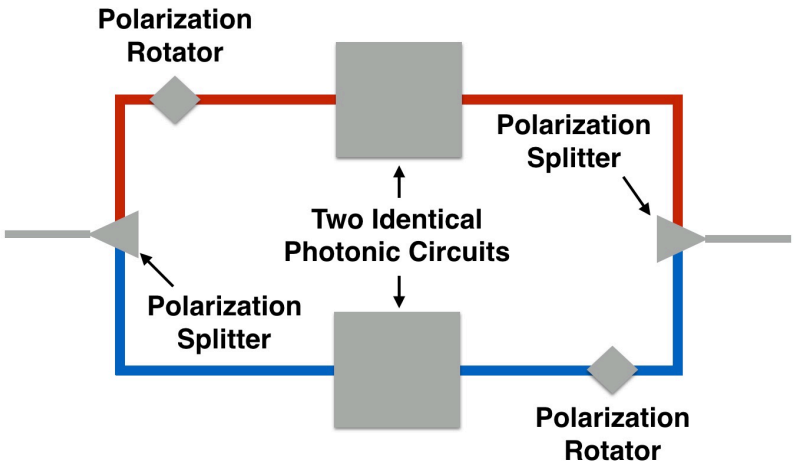

Figure 1.5: Schematic of a polarization diverse PICs.

1.2 Sub-wavelength Structures

Sub-wavelength periodic structures are arrangements of different materials with a pitch small enough to suppress the diffraction effects arising from their periodicity [32]. With the development of high-resolution lithography, sub-wavelength structures have seen widespread application in photonic integrated circuits for the SOI platform. Currently, sub-wavelength structures have been used to optimize grating couplers [4–6, 14, 16, 17, 22, 24, 29, 33, 46, 59, 83–85, 93–95, 101], wavelength multiplexers [13], and to design low-loss waveguide crossings [9], high Q resonators [26, 82], biosensors [25, 26], broadband power splitters and combiners [30, 48], and polarization splitter-rotators (PSRs) [91], etc.

1.2.1 The Sub-wavelength Regime

The electromagnetic properties of the sub-wavelength structures considered in this dissertation are fully described by the theory developed for photonic crystals [37] and the principle and applications of sub-wavelength structures for the SOI platform are detailed in a review paper by Halir [32]. Here, we only provide a simplified theory about the sub-wavelength structure to facilitate the understanding of this dissertation. Consider the periodic grating structures for the SOI platform as shown in Fig. 1.6, which consists of rectangles with alternating indices of n_1 and n_2, and a substrate which has an index of n_3. In our case, $n_1 = 3.47$, $n_3 = 1.45$, and $n_2 = 1.45$ or 1 when oxide/air cladding is used. The fill factor, or duty cycle of the structure, ff, is defined as $ff = l/\Lambda$, where l denotes the length of one grating and Λ denotes the period of the grating. The thickness of the top silicon layer is denoted by t, and $t = 220\,\text{nm}$ in our case. Depending on the ratio of Λ and

the operating wavelength, λ, the periodic structure shown in Fig. 1.6 can generally operate in the following regimes [32]:

- the diffraction regime, where the incoming beam is scattered in different orders;
- the reflection regime, where the incoming beam is reflected backwards;
- the sub-wavelength regime, where diffraction effects due to the periodicity of the structure are suppressed.

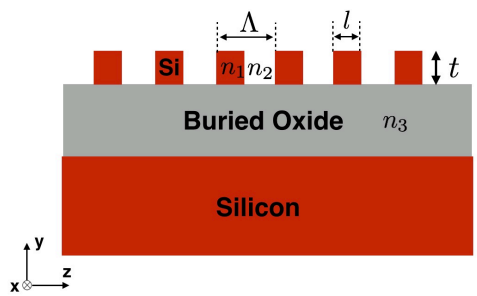

Figure 1.6: Schematic of the cross-section of a periodic waveguide structure.

When light incident on the grating structure shown in Fig 1.6, the angle of diffraction orders can be expressed as:

$$n_{\mathrm{d}} \cdot sin(\theta_k) = k \cdot \frac{\lambda}{\Lambda} \tag{1.1}$$

where θ_k denote the diffraction angle, k denotes the diffraction order, and $n_{\mathrm{d}} = \{n_2, n_3\}$ for diffractions into the cladding and substrate, respectively [60]. For the SOI platform, all diffraction orders will be eliminated when

$$\frac{\lambda}{\Lambda} > n_{\mathrm{d}} = 1.45 \tag{1.2}$$

In this dissertation, a periodic structure where all diffraction orders are suppressed is referred to as a sub-wavelength structure. In the sub-wavelength regime, both the reflection and the diffraction effects are suppressed and light will propagate through the sub-wavelength structure without affected by the discontinuities along the propagation direction.

1.2.2 Effective Medium Theory

Sub-wavelength structures can be approximated as a homogeneous material with an equivalent refractive index when $\lambda \gg \Lambda$, and the equivalent refractive index of the sub-wavelength structure can be calculated with a zeroth-order approximation given by Rytov [64]:

$$n_{\parallel}^{(0)} = \left[n_1^2 \cdot ff + n_2^2 \cdot (1 - ff)\right]^{1/2} \tag{1.3}$$

$$\frac{1}{n_{\perp}^{(0)}} = \left[\frac{ff}{n_1^2} + \frac{(1 - ff)}{n_2^2}\right]^{1/2} \tag{1.4}$$

where $n_{\parallel}^{(0)}$ denotes the zeroth order approximation of the equivalent refractive index for the polarization along the x direction, and $n_{\perp}^{(0)}$ denotes the zeroth order approximation of the equivalent refractive index for the polarization along the z direction. In the case when the ratio of λ and Λ are smaller, higher order approximations can be used to calculate the equivalent refractive indices more accurately [40, 41]. It should be noted that in the calculation given by Rytov, the assumption has been made that the structure is infinite in the x and y directions. When designing a sub-wavelength structure, Rytov's formulas can be used as a starting point for further optimizations of the design using more accurate numerical calculations.

1.2.3 Applications of Sub-wavelength Structures on SOI

One of the fundamental building blocks, using sub-wavelength structures, is the sub-wavelength grating (SWG) waveguide. Scanning electron microscope (SEM) images of an SWG waveguide and an SWG waveguide taper are shown in Fig. 1.7. A theoretical study has confirmed that the SWG waveguide is lossless in the absence of fabrication imperfections [69]. As compared to the conventional silicon wire waveguides, SWG waveguides provide some features that are beneficial in specific applications. Due to the fact that SWG waveguides consist of rectangles with alternating indices, SU-8 polymer has been used as the cladding material to make athermal SWG waveguides [35, 66]. Due to the fact that SU-8 has a negative thermo-optic coefficient while silicon has a positive thermo-optic coefficient, a athermal SWG waveguide can be created by interleaving specific amounts of these two materials. Silicon oxide is normally used as the cladding material for SOI devices, and the material dispersion of silicon oxide is 6X lower than in silicon. Therefore, SWG waveguides are less wavelength dependent than silicon waveguides. Experimental demonstration of SWG waveguide, which has propagation loss as low as 2.1 dB/cm with negligible polarization and wavelength dependent loss has been demonstrated in [8]. In addition, SWG waveguides also have a much smaller effective indices as compared to the conventional silicon wire waveguide. The reduced effective indices leads to loosely confined optical modes in the waveguides, which are ideal for applications such as bio-sensing [25]. Fig. 1.8 shows the SEM images of a directional coupler consisting of strip waveguides and a directional coupler consisting of a strip waveguide and an SWG waveguide, where SWG waveguide is used to improve the sensitivity of bio-sensors [27].

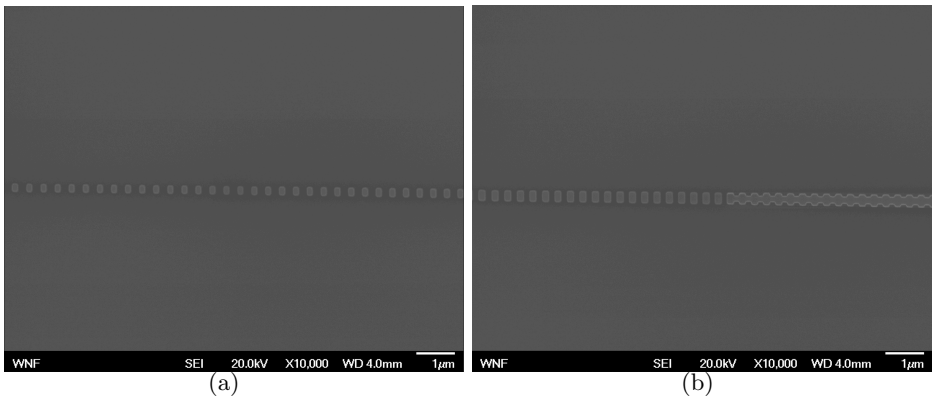

(a) (b)

Figure 1.7: SEM images of (a) an SWG waveguide, and (b) an SWG waveguide with an SWG waveguide taper.

Sub-wavelength structures have also been used to optimize grating couplers. When combining fundamental building blocks that can be fabricated in a single, fully-etched step, having fully-etched sub-wavelength grating couplers (SWGCs) provides an efficient and economical solution for rapid prototyping. Various types of sub-wavelengths structures have been used in grating couplers [4–6, 14, 16, 17, 22, 24, 29, 33, 46, 59, 83–85, 93–95, 101]. Depending on the dimensions of the sub-wavelength structures, SWGs can be divided as two-dimension SWGs and one-dimensional SWGs. Depending on the shape of an SWGC, they can also be divided as straight SWGCs and focusing SWGCs. SEMs images of a straight SWGC with two-dimension SWGs and a focusing SWGC with one-dimensional SWGs are shown in Fig. 1.9.

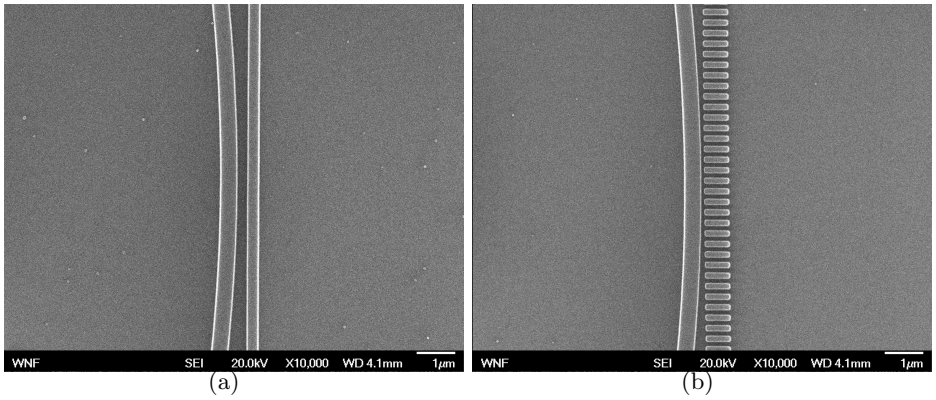

(a) (b)

Figure 1.8: SEM images of (a) a directional coupler consisting of strip waveguides, and (b) a directional coupler consisting of a strip waveguide and an SWG waveguide.

1.3 About This Dissertation

1.3.1 Objective

The objective of this dissertation is to investigate the properties of sub-wavelength structures on the SOI platform and use the design flexibility they provide to improve the performance of existing photonic devices and design novel photonic devices on the SOI platform. The long-term objective of this work is to apply the benefits from sub-wavelength structures to develop large-scale PICs with enhanced performance and enriched functionalities for various applications, such as high-speed optical interconnects and enhanced bio-sensing systems.

1.3.2 Dissertation Organization

In Chapter 2 we demonstrate compact, high-efficiency, fully-etched sub-wavelength grating couplers (SWGCs) for both the fundamental transverse electric, TE_0, mode and the fundamental transverse magnetic, TM_0, mode.

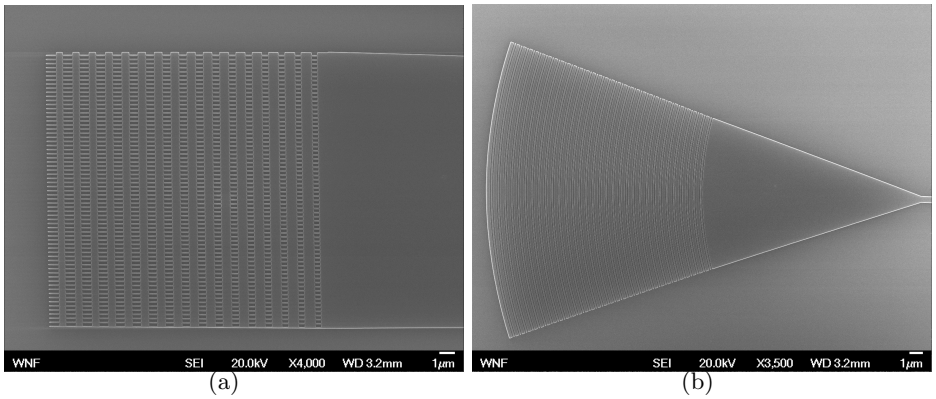

(a) (b)

Figure 1.9: SEM images of (a) a straight SWGC with two-dimensional SWGs and (b) a focusing SWGC with one-dimensional SWGs.

There are different forms of mode notations used in literatures. In this dissertation, we used the same form as Yariv [96], where the notation denotes the number of nodes for a mode. The design methodology for SWGCs with one-dimensional sub-wavelength gratings (SWGs) are demonstrated. The index profile of an SWGC is engineered using SWGs for improved coupling efficiency and suppressed back reflections. The design, simulation, and characterization of SWGCs with uniform gratings are demonstrated in the Section 2.1 of Chapter 2 and apodized SWGCs with improved coupling efficiency are demonstrated in Section 2.2 of Chapter 2.

In Chapter 3, we demonstrate compact SWGCs with ultra-broad operating bandwidths for the SOI platform. We first derive the analytical expression for the bandwidth of a grating coupler, in which we show the relation between the group index and the operating bandwidth of a grating coupler. Based on the theoretical study, we propose a methodology to design broadband SWGCs with design-intent operating bandwidth. The design, simulation, and characterization of broadband SWGCs are demonstrated. In addition, broadband SWGCs with different design shapes, i.e., SWGCs

with straight gratings lines and focusing grating lines, are compared.

In Chapter 4, we demonstrate compact, broadband directional couplers using SWGs for the SOI platform. The dispersion properties of the optical modes in a conventional directional coupler are engineered using SWGs, which allows broadband operation. Finite-difference time-domain (FDTD) based band structure calculations, with reduced simulation time, are used to analyze the design, which includes both the material and the waveguide dispersions. Compact broadband direction couplers, with device lengths shorter than 14 µm, which cover bandwidths of 100 nm, for power splitting ratios of 50/50, 40/60, 30/70, and 20/80, are designed and fabricated for the TE_0 mode with λ of 1550 nm.

In Chapter 5, we demonstrate an ultra-compact SWG polarization splitter-rotator for the SOI platform, where an SWG waveguide is used to manage the polarization of light. An asymmetric directional coupler, consists of a regular strip waveguide and an SWG waveguide, is used to couple the TM_0 mode of the strip waveguide into the TE_0 mode of the SWG waveguide. The SWGs provides the freedom to engineer the dispersion properties of the supermodes, which allow the design to be fabrication tolerant to the waveguide width variations. A high-efficiency, space-efficient SWG taper is also demonstrated to couple the light from the SWG waveguide into a strip waveguide. The design, simulation, and characterization of the SWG PSR are shown as well.

The dissertation is concluded in Chapter 6 with a brief summary and discussions about future research directions.

Chapter 2

High-Efficiency Fully-etched Sub-wavelength Grating Couplers

In this chapter, we demonstrate high-efficiency, fully-etched sub-wavelength grating couplers (SWGCs) for the TE_0 mode and the TM_0 mode. From here on, we call the SWGCs designed for the TE_0 mode as TE SWGCs and the SWGCs designed for the TM_0 mode as TM SWGCs for simplicity. SWGCs with uniform gratings are shown in Section 2.1 and apodized SWGCs with improved coupling efficiencies are shown in Section 2.2.

2.1 Uniform Sub-wavelength Grating Couplers

2.1.1 Challenges of Fully-etched Grating Couplers

The critical issues faced by fully-etched grating couplers include high insertion loss and strong back reflections from the grating to the waveguide. The high insertion loss is mainly caused by the penetration loss into the substrate and the mode mismatch between the optical fiber and the grating. The large back reflection results mainly from Fresnel reflections caused by the refractive index contrast between the high and low index regions in the grating.

Fig. 2.1 shows the typical measurement spectra for a pair of shallow-etched grating couplers and fully-etched grating couplers, as shown in Fig. 1.3. The calculated Fresnel reflection coefficients for the shallow-etched grating, with an etch depth of 70 nm into a 220 nm-thick silicon layer, and a fully-etched grating, with a 220 nm silicon layer and oxide cladding, at 1550 nm, are 0.6% and 17%, respectively, which correspond to oscillation ripples with extinction ratios (ERs) of 0.1 dB and 3 dB, respectively. The calculated ERs of the ripples agree with those of the the measured results shown in Fig. 2.1.

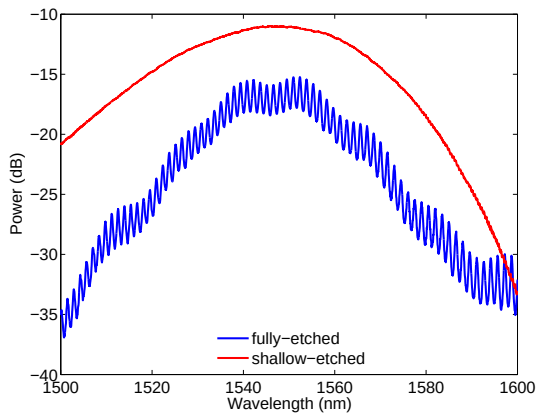

Figure 2.1: Measured transmission spectra for a pair of shallow-etched grating couplers and fully-etched grating coupler.

The refractive index contrast in a regular fully-etched grating coupler is much larger than that of a shallowed-etched grating coupler, which motivates the need for an effective index material using sub-wavelength gratings (SWGs) to approximate the shallow-etched regions in a fully-etched grating coupler. A schematic of a fully-etched grating coupler with effective index regions is shown in Fig. 2.2, where n_H and n_L denote the effective refractive indices of the high and low index regions, respectively. Two dimensional SWGs have been demonstrated to obtain the low index regions in a grating coupler [4–6, 14, 16, 17, 22, 24, 29, 33, 46, 59, 93–95, 101]. Here, we demon-

strated grating couplers using one-dimensional SWGs to obtain the low index regions for the first time [84, 85]. A schematic of a fully-etched grating coupler with low index regions obtained using one-dimensional SWGs is shown in Fig. 2.3. The high index regions, denoted by n_H in Fig. 2.3 is silicon in this case. From here on, we will simply refer to the fully-etched SWGCs as SWGCs in the rest of this dissertation.

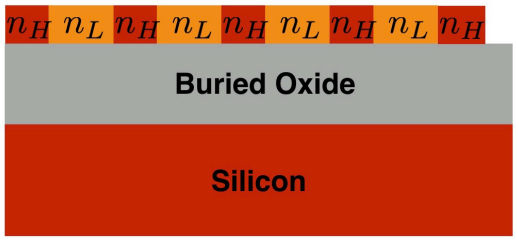

Figure 2.2: A Schematics of a fully-etched grating couplers with effective index regions.

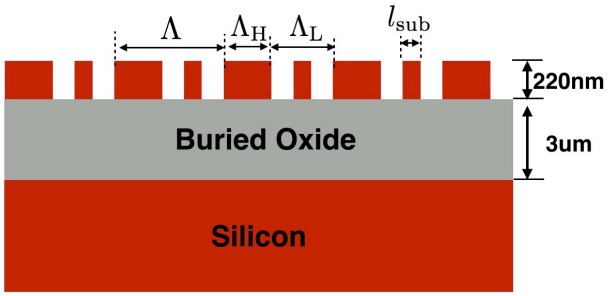

Figure 2.3: Schematics of a fully-etched SWGCs with one-dimensional SWGs.

2.1.2 2D SWGs vs. 1D SWGs

It is advantageous to use one-dimensional SWGs (sub-wavelength grating lines), as compared to two-dimensional SWGs (sub-wavelength quasi-squares), to achieve the low effective index regions in SWGCs for several reasons.

From the fabrication perspective, the one-dimensional SWGs are less challenging to produce because they benefit from higher exposure contrasts [84] and shorter fabrication times, resulting in higher fabrication accuracy and lower fabrication cost. Figure 2.4 shows the simulated energy distribution from *BEAMER*, a electron-beam lithography software from *GenISys GmbH* [34], for fabricating two-dimensional SWGs and one-dimensional SWGs using electron beam lithography. The simulator used a defined Point Spread Function (PSF) for 100 kV electrons on silicon, then produced a 2-D plot of energy distribution after exposure for the pattern data. The PSF shows energy as a function of radial distance from the electron beam, which is caused by electron backscattering and secondary electron generation in the silicon. The lithography simulation applies the PSF to the pattern data, to produce the 2-D energy distribution for different geometries. Figure 2.4(a) and (c) show the respective energy distributions of the two-dimensional SWGs, sub-wavelength holes with uniform diameters, and one-dimensional SWGs, where the blue denotes the least energy and the red denotes the most energy. The 1-D cutlines across the 2-D simulations show the differences associated with fabricating different type of structures. We get 30% exposure in the two-dimensional SWGs as shown in Fig. 2.4(b) where no exposure is required, whereas for the one-dimensional SWGs, we only get about 10% exposure as shown in Fig. 2.4(d) in the region where no exposure is required. Even though a high contrast resist process was used, the 30% exposure shown in the two-dimensional SWGs is still enough energy to at least partially expose the resist, which results in a high variability in feature size. It can be noted that the exposure contrast in the low effective index regions has been improved by implementing one-dimensional SWGs. From the design perspective, due to the use of one-dimensional SWGs that stretch the

entire width of the coupler, our SWGCs are simple and straightforward to draw and subsequently, to simulate in both 2D and 3D. By contrast, effective refractive indices were used in 2D simulations to approximate the effective index regions in SWGCs using two-dimensional SWGs, which over simplifies the situation and results in mismatches between simulations and measurements. In addition, SWGCs with one-dimensional SWGs also enable focusing gratings with smaller footprint using the method demonstrated in [77], which are difficult to be achieved with two-dimensional SWGs.

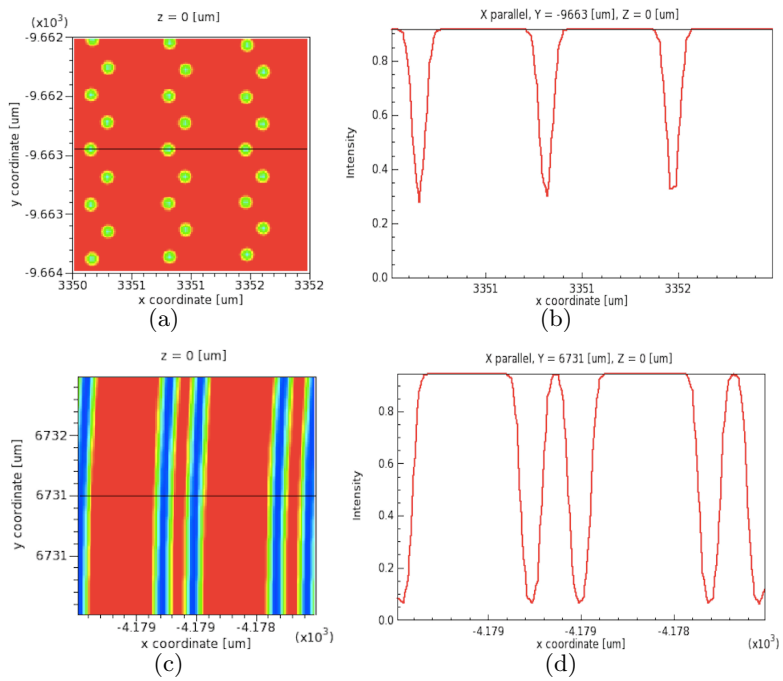

Figure 2.4: (a) 2D energy distribution of an SWGC formed by two-dimensional SWGs; (b) energy distribution along the 1-D cutline across the 2-D simulation of an SWGC formed by two-dimensional SWGs; (c) 2D energy distribution of an SWGC formed by one-dimensional SWGs; (d) energy distribution along 1-D cutlines across the 2-D simulations of SWGCs formed by one-dimensional SWGs.

2.1.3 Design and Simulation

As shown in Fig. 2.3, our SWGC has a grating period of Λ, and each grating period consist of a high index region with a width of Λ_{H} and a low index region with a width of Λ_{L}. The fill factor, ff, of the SWGC shown in Fig. 2.3 is defined as the ratio of Λ_{H} to Λ. The length of an SWG in the low index regions is denoted by l_{sub}.

Incident Angle

The incident angle of an SWGC is determined by the phase-match condition between the grating mode and the fiber mode. As shown in Fig. 2.5, if we denote θ as the incident angle, which is defined as the angle between the direction of the out-coupled wave and the normal to the grating, then the phase-match condition can be expressed as:

$$n_{\mathrm{eff}} \cdot \Lambda = n_f \cdot \Lambda \cdot sin\theta + N \cdot \lambda \tag{2.1}$$

where n_{eff} is the effective index of the mode propagating in the grating, n_f is the effective index of the fiber mode, λ is the operating wavelength, and N is the diffraction order. It should be noted that θ can be either positive or negative. θ is positive when the out-coupled wave has a component in the same direction as the input wave, as shown in shown in Fig. 2.5(a), while θ is negative when the out-coupled wave has a component in the opposite direction to the input wave, as shown in Fig. 2.5(b).

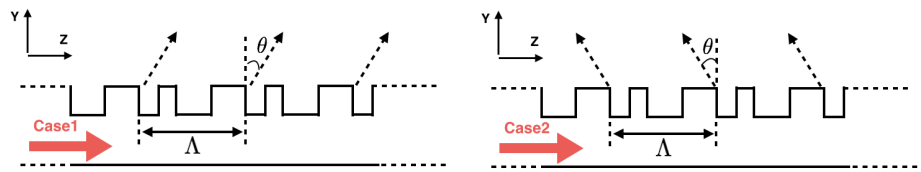

(a) (b)

Figure 2.5: Schematic of the cross-section of an SWGC with (a) a positive incident angle and (b) a negative incident angle.

Parameter Optimization

Our SWGCs are optimized using the finite-difference time-domain (FDTD) method combined with the particle swarm algorithm (PSA) [62]. PSA is a population based stochastic optimization technique, inspired by the social behavior of flocks of birds or schools of fish [57, 62], and has widely been used for various kinds of design optimization problems, including nanophotonic designs [49, 53, 68, 100]. In PSA, the potential solutions, called particles, are initialized at random positions, and then move within the parameter search space. The particles are subject to three forces as they move: a. spring force towards the personal best position, p, ever achieved by that individual particle; b. spring force towards the global best position, g, ever achieved by any particle; c. a frictional force, proportional to the velocity. A commercial FDTD-method Maxwell equation solver, *FDTD Solutions* [72], from *Lumerical Solutions, Inc.* with the built-in PSA was used to conduct the design optimizations.

The schematic of the simulated structures are shown in Fig. 2.6. First, the light was launched from the waveguide, as shown in Fig. 2.6(a), and diffracted by the grating. A power monitor was positioned on top of the grating to measure the power diffracted upward by the grating. Three design parameters, i.e., Λ, Λ_{H}, and l_{sub} as defined in Fig. 2.3, have been

optimized to achieve the highest directionality, which is defined as the ratio of the optical power diffracted upward by the grating to the input power. After we got the highest directionality, a far field calculation was done by the power monitor to calculate the diffraction angle of the light from the grating, which is the same as the incident angle of the SWGC. The optimized incident angles for the TE and TM SWGCs were -25° and 10°, respectively. Then, the light was launched from the fiber with the optimized angle, shown in Fig. 2.6(b). A power monitor was positioned in the waveguide to monitor the total power and another mode expansion monitor was used to calculate the power coupled into a specific mode. Again, Λ, Λ_{H}, and l_{sub} were optimized using PSA in *FDTD Solutions*. Eight simulation generations with eight variations within each generation were used to obtain SWGCs with the highest coupling efficiencies for the TE_0 mode and the TM_0 mode, respectively. The optimized TE SWGC has $\Lambda = 593\,\mathrm{nm}$, $\Lambda_{\mathrm{H}} = 237\,\mathrm{nm}$, and $l_{\mathrm{sub}} = 74\,\mathrm{nm}$. The optimized TM SWGC has $\Lambda = 960\,\mathrm{nm}$, $\Lambda_{\mathrm{H}} = 575\,\mathrm{nm}$, and $l_{\mathrm{sub}} = 140\,\mathrm{nm}$. The incident angles for the TE and TM SWGCs are -25° and 10°, respectively.

The simulated coupling efficiency and the back reflection of the optimized TE SWGC are shown in Fig. 2.7. For comparison purposes, the simulated coupling efficiency and the back reflection of a shallow-etched grating coupler, with a partial etching layer of 70 nm, are also shown in Fig. 2.7. The coupling efficiencies are simulated using the structure shown in Fig. 2.6(b), where a mode expansion monitor is used to calculate the power coupled to the fundamental TE mode. The back reflections are simulated using the structure shown in Fig. 2.6(a), where the mode expansion monitor was positioned in the opposite direction of the input mode to calculate the power coupled back forward into the fundamental TE mode. The shallow-etched

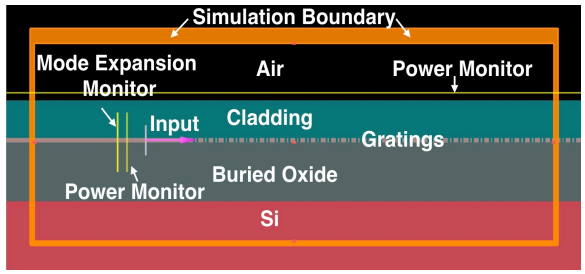

(a)

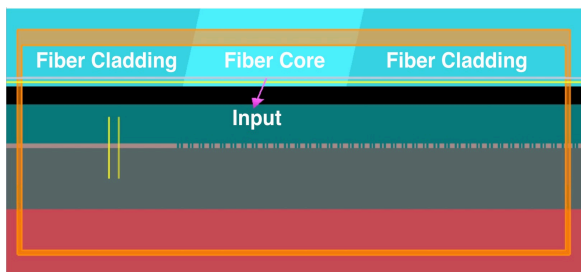

(b)

Figure 2.6: Simulations of SWGCs in *FDTD Solutions.*

grating coupler was optimized based on the same wafer type using the same algorithm as the TE SWGC. The optimized TE SWGC shows a simulated peak coupling efficiency of $-2.2\,\mathrm{dB}$ with a 1-dB bandwidth of $32.5\,\mathrm{nm}$ (3-dB bandwidth of $58\,\mathrm{nm}$), which are comparable to the performance of the optimized shallow-etched grating coupler.

The simulated coupling efficiency and the back reflection of the optimized TM SWGC are shown in Fig. 2.8. Again, the coupling efficiency and the back reflection for an optimized shallow-etched grating coupled for the same λ and polarization of light are shown in the same graph for comparison purposes. The TM SWGC not only has a higher coupling efficiency, but also shows a broader bandwidth than the shallow-etched grating coupler. The TM SWGC shows a simulated peak coupling efficiency of $-2.7\,\mathrm{dB}$ with a 1-dB bandwidth of $57\,\mathrm{nm}$ (3-dB bandwidth of $92\,\mathrm{nm}$). The optimization

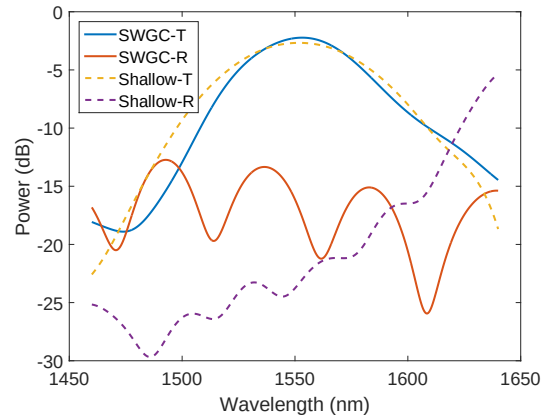

Figure 2.7: Simulated coupling efficiency and back reflection for the TE SWGC and a shallow-etched grating coupler. SWGC-T and SWGC-R denote the coupling efficiency and the back reflection of the optimized TE SWGC, Shallow-T and Shallow-R denote the coupling efficiency and the back reflection of the optimized shallow-etched grating coupler.

was based on uniform gratings, where further improvement can be obtained by apodizing the grating periods to achieve better mode overlap between the grating and the optical fiber.

It should be noted that the peak coupling efficiencies and operating bandwidths of the TE and TM SWGCs are different. The difference in the coupling efficiencies is caused by the different coupling strength of the two grating couplers. The power in the waveguide undergoes an exponential decay due to the presence of the grating:

$$P_{\mathrm{wg}}(z) = P_{\mathrm{wg}}(z = 0) \cdot \exp(-2\alpha z) \tag{2.2}$$

where α is the coupling strength or leakage factor of the grating, $P_{\mathrm{wg}}(z)$ denotes the power of the mode at z, assuming the wave is propagating along the z-axis. The directionality, which is the power diffracted upward

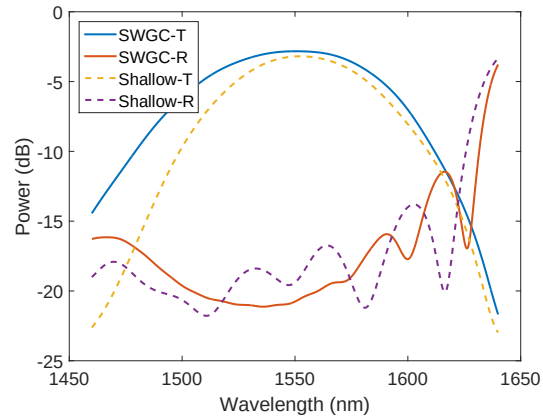

Figure 2.8: The simulated coupling efficiency and the back reflection for the TM SWGC and a shallow-etched grating coupler. SWGC-T and SWGC-R denote the coupling efficiency and the back reflection of the optimized TM SWGC, Shallow-T and Shallow-R denote the coupling efficiency and the back reflection of the optimized shallow-etched grating coupler.

by a grating coupler, of the TE and TM SWGCs are similar, which are about 69%. However, the α values of the TE and TM SWGCs are different, therefore, the coupling losses caused by the mode mismatches between the fiber and grating are different, which lead to the difference in the peak coupling efficiencies. According to [16], the 1-dB bandwidth of a grating coupler can be expressed as:

$$\Delta\lambda = \eta_{\mathrm{1dB}}|\frac{d\lambda}{d\theta}| = \eta_{\mathrm{1dB}}|\frac{-\Lambda \cdot n_c \cdot cos(\theta)}{1 - \Lambda \cdot \frac{dn_{\mathrm{eff}}(\lambda)}{d\lambda}}| \tag{2.3}$$

where η_{1dB} is the 1-dB bandwidth coefficient, n_c is the refractive index of the cladding material, $\mathrm{n_{eff}}$ is the effective index of the grating. The period of the TM SWGC is much larger than that of the TE SWGC, and the θ of the TM SWGC is smaller than the TE SWGC, which contribute to a broader bandwidth for the TM SWGC.

System simulation

In actual photonic circuits, a pair of grating couplers are typically used: one input grating coupler and one output grating coupler. A Fabry-Perot cavity forms between the input and output grating couplers, where the reflected wave propagates between the two grating couplers and introduces ripples in the spectral responses of the photonic circuits. Scattering parameters (S-parameters) can be used to describe the behaviour of the grating coupler [18]. Simulation of a full input-waveguide-output circuit has been performed using *Interconnect* [58], and Fig. 2.9(a) shows a schematic of the input-waveguide-output circuit in *Interconnect*. A virtual optical network analyzer is used to generate and measure the optical signal. The grating couplers are represented by two 2-port S-parameter matrices, which were exported from *FDTD Solutions*. The waveguide is a component that can be either loaded from *Interconnect* or imported from *Mode Solutions*, an eigenmode solver from *Lumerical Solutions, Inc.* The simulated transmission spectra for the input-waveguide-ouput circuits are shown in Fig. 2.9(b). The blue line shows the simulated transmission spectrum with two TE SWGCs, with 127 µm pitch, connected by a silicon wire waveguide, and the red line shows the same simulation results for the TM SWGCs. As shown in Fig. 2.9(b), the ERs of the ripples shown for our TE and TM SWGCs are only 0.3 dB and 0.15 dB, respectively.

Focusing Grating Lines

So far we have addressed the SWGC as a two-dimension structure and Equation 2.1 has assumed that the grating is linearly extended in the lateral direction, where a linear taper is required to couple the light from the grating

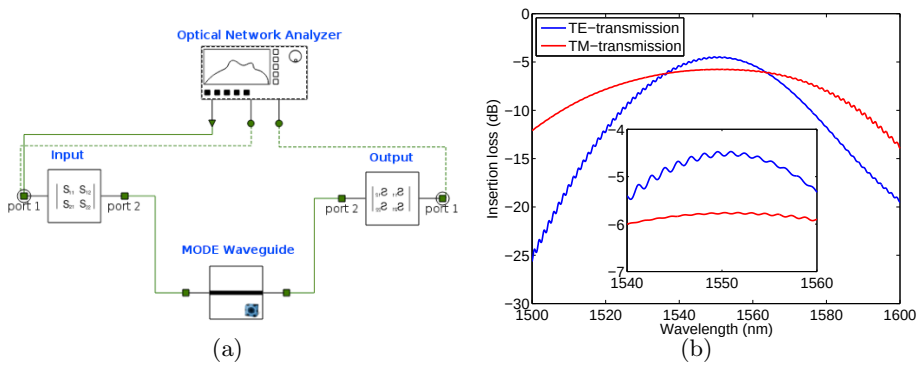

(a) (b)

Figure 2.9: (a) Schematic of the input-waveguide-output circuit in *Interconnect*, and (b) simulated transmission spectra of input-waveguide-ouput circuits for TE and TM SWGCs.

to a regular silicon wire waveguide. The layout of a grating coupler with straight grating lines and an a linear taper is shown in Fig. 2.10(a). To achieve adiabatic coupling, the required length for the taper is on the order of a few hundred microns. However, the long adiabatic tapers are not space efficient, consuming valuable on-chip real estate. Focusing grating lines are used as an alternative to achieve efficient mode size conversion [77]. The layout of a grating coupler with focusing grating lines is shown in Fig. 2.10(b). The phase-match condition for a focusing SWGC can be expressed as:

$$n_{\text{eff}} \cdot r = n_f \cdot r \cdot sin\theta \cdot cos\phi + N \cdot \lambda \tag{2.4}$$

where n_{eff} denotes the effective index of the grating, n_f is the effective index of the fiber mode, θ denotes the incident angle, r denote the distance from the end of the silicon-wire waveguide (O as shown in Fig. 2.11) to an arbitrary point (P shown in Fig. 2.11) in the X-Z plan, ϕ denotes the angle between the OP and the z-axis. From Equation 2.4, we can get the

expression for r as:

$$r = \frac{N \cdot \lambda}{n_{\text{eff}} - n_f \cdot sin\theta \cdot cos\phi} \tag{2.5}$$

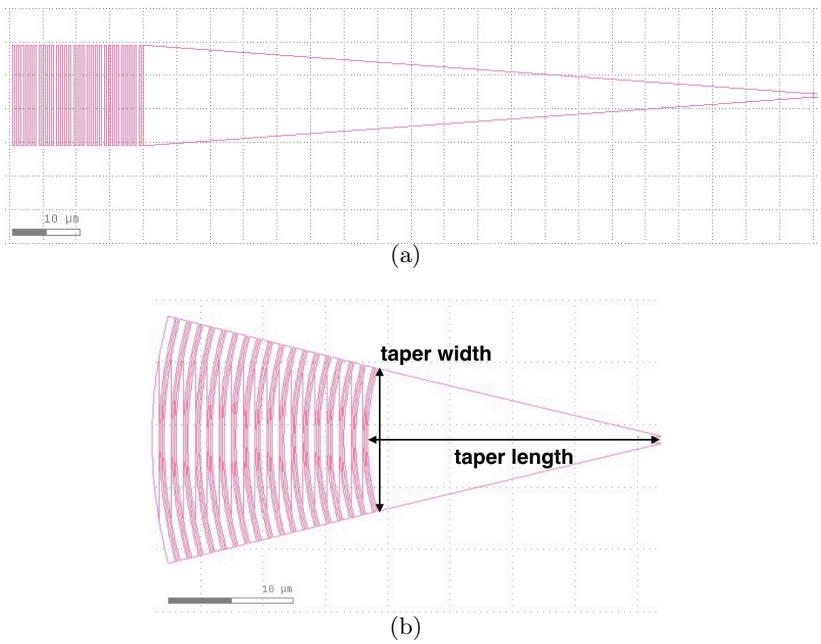

Figure 2.10: Mask layouts of (a) a grating coupler with straight grating lines and a linear taper, and (b) an SWGC with focusing grating lines.

Equation 2.4 defines a family of confocal ellipses with one of the focal points at the end of the waveguide. Schematics of the focusing grating lines for SWGCs are shown in Fig. 2.11. It should be noted that the grating pattern of the SWGCs with positive and negative incident angles are different. For SWGCs with positive incident angles, as shown in Fig. 2.11(a), the waveguide end overlaps with the left focal point of the confocal ellipses. For SWGCs with negative incident angles, as shown in Fig. 2.11(b), the waveguide end overlaps with the right focal point of the confocal ellipses. A parameterized device cell has been created in *Mentor Graphics's Pyxis* [18]

to generate the layout files for various SWGCs. The layout of an focusing SWGC is shown in Fig. 2.10(b).

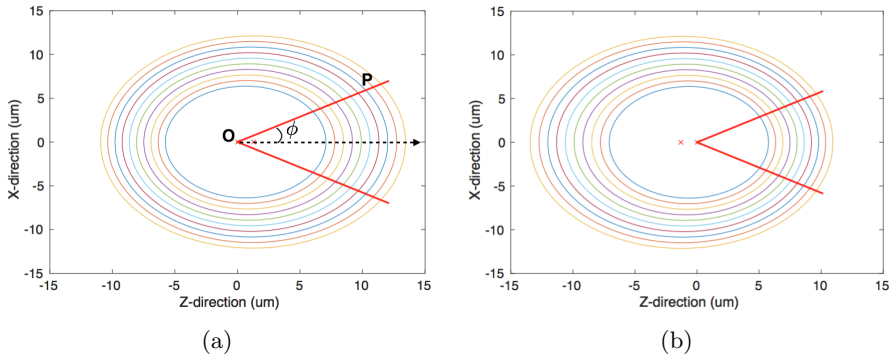

Figure 2.11: Schematics for SWGCs with focusing grating lines and (a) positive incident angles, and (b) negative incident angles.

The shape of the taper in a focusing SWGC needs to be optimized in order to avoid excess loss in the taper. In Eq. 2.4, N decides the taper length and for a given N, ϕ decides the taper width, as shown in Fig. 2.10(b). 3D FDTD simulations have been done to optimize the tapers of our SWGCs in the following steps. First, we fixed the value of N for a taper length of 22 µm, then we varied the value of ϕ. The highest coupling efficiency were achieved for both the TE and TM SWGCs when the taper widths are about 10.6 µm, which is similar to the diameter of the optical mode from the PM fiber we used. Next, we simulated SWGCs with different combinations of N and ϕ with the same taper width of 10.6 µm. The highest coupling efficiencies were achieved for the TE and TM SWGCs when the length to width ratios of the tapers were 2.76 and 2.24, respectively. The simulated coupling efficiencies of the optimized TE and TM SWGCs in 3D FDTD simulations are −2.5 dB and −2.8 dB, which are 0.3 dB and 0.1 dB lower than the simulated results in 2D FDTD simulations, respectively. Such differences are due to propagation

losses in the tapers, which can be improved by further design optimizations of the tapers.

2.1.4 Fabrication and Measurement

Test structures, consisting of an input SWGC and an output SWGC, with 127 µm pitch, connected by a strip waveguide have been fabricated using electron beam lithography at the University of Washington [11]. The fabrication used SOI wafers with 220 nm thick silicon on 3 µm thick silicon dioxide. The substrates were 25 mm squares diced from 150 mm wafers. Oxide cladding was used for the protection of the chip. After a solvent rinse and hotplate dehydration bake, hydrogen silsesquioxane resist (HSQ, Dow-Corning XP-1541-006) was spin-coated at 4000 rpm, then hotplate baked at 80 °C for 4 minutes. Electron beam lithography was performed using a JEOL JBX-6300FS system operated at 100 kV energy, 8 nA beam current, and 500 µm exposure field size. The machine grid used for shape placement was 1 nm, while the beam stepping grid, the spacing between dwell points during the shape writing, was 6 nm. An exposure dose of 2800 $\mu C/cm^2$ was used. The resist was developed by immersion in 25% tetramethylammonium hydroxide for 4 minutes, followed by a flowing deionized water rinse for 60 s, an isopropanol rinse for 10 s, and then blown dry with nitrogen. The silicon was removed from unexposed areas using inductively coupled plasma etching in an Oxford Plasmalab System 100, with a chlorine gas flow of 20 sccm, pressure of 12 mT, ICP power of 800 W, bias power of 40 W, and a platen temperature of 20 °C, resulting in a bias voltage of 185 V. During etching, chips were mounted on a 100 mm silicon carrier wafer using perfluoropolyether vacuum oil. The scanning electron microscope (SEM) images

of the fabricated SWGCs are shown in Fig. 2.12.

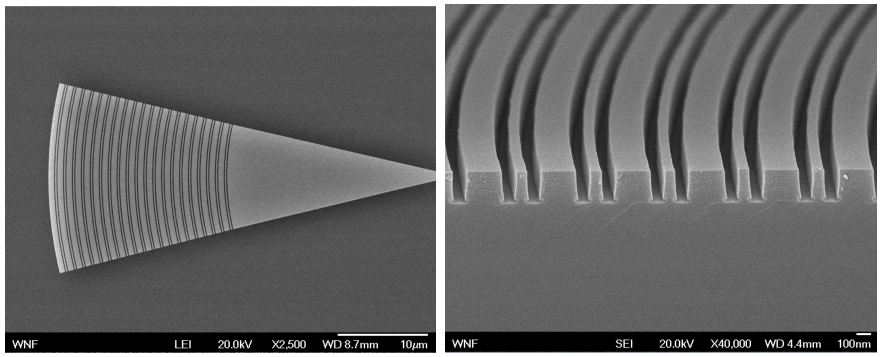

(a) (b)

Figure 2.12: SEM images of (a) the top view of a fabricated SWGC and (b) the side view of a fabricated SWGC.

To characterize the devices, a custom-built automated test setup [19] was used. An Agilent 81600B tunable laser, with a polarization maintaining (PM) fiber, was used as the input source, and Agilent 81635A optical power sensors, also with PM fibers, were used as the output detectors. A wavelength sweep from 1500 nm to 1600 nm in 10 pm steps was performed.

Fabrication Tolerance

Variations were applied to Λ, Λ_{H}, and l_{sub} to understand the sensitivities of these design parameters to the fabrication imperfections. Figure 2.13 shows the central wavelength shifts as a function of various design parameter variations for the TE and TM SWGCs, respectively. Figure 2.13(a) shows the simulated central wavelength offsets as a function of Λ, Λ_{H}, and l_{sub} for the TE SWGC. The blue circles indicate the central wavelength shift as a function of $\delta\Lambda$, the red crosses indicate the central wavelength shift as a function of the $\delta\Lambda_{\mathrm{H}}$, and the purple diamonds indicate the central wavelength shift as a function of δl_{sub}. Figure 2.13(b) shows the measurement results for

the as-fabricated TE SWGCs with the same design parameters. The same analysis has been applied to the TM SWGCs and the results are shown in Fig. 2.13(c) and Fig. 2.13(d). Linear-fits have been applied to compare the sensitivities of Λ, Λ_{H}, and l_{sub} and the corresponding slopes are shown in Table 2.1.

Table 2.1: Simulated and measured sensitivities of the central wavelength as a function of Λ, Λ_{H}, and l_{sub}.

	TE		TM	
	simulation (nm/nm)	experiment (nm/nm)	simulation (nm/nm)	experiment (nm/nm)
Λ	1.3	1.0	0.59	0.43
Λ_{H}	0.73	0.67	0.39	0.35
l_{sub}	2.1	2.06	0.31	0.24

It can be noted that the slopes extracted from the experimental results were slightly smaller than the simulated results for both the TE and TM SWGCs, but the comparative relation between those values were the same in both cases. From Table 2.1 we can see that Λ and l_{sub} were the key parameters affecting the central wavelength of the SWGCs. In addition, we can notice that the slopes of various design parameters for the TM SWGCs were smaller than that of the TE SWGCs, which indicate a lower sensitivity to fabrication imperfections.

TE SWGC

The measurement transmission spectrum of a TE SWGC is denoted by the red line shown in Fig. 2.14. The simulated transmission spectrum for the same design is denoted by the blue line shown in Fig. 2.14 for comparison purposes. The best device has a measured coupling efficiency of $-4.1\,\mathrm{dB}$

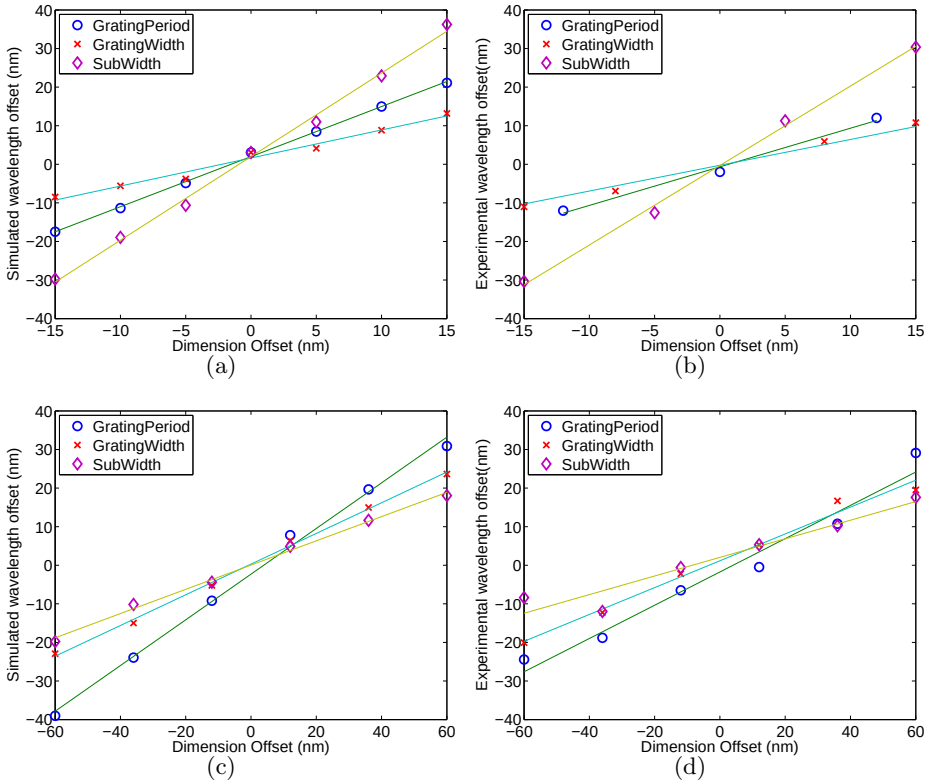

Figure 2.13: (a) Simulated sensitivities of Λ, Λ_{H}, and l_{sub} for the TE SWGCs; (b) measured sensitivities for the TE SWGCs; (c) simulated sensitivities for the TM SWGCs; (d) measured sensitivities for the TM SWGCs.

with a 1-dB bandwidth of 30.6 nm (3-dB bandwidth of 52.3 nm). The measured peak coupling efficiency is lower than the simulated value, which may come from two major sources. First, the insertion losses from the fiber array and all the optical connections, i.e., connection between the laser and the fiber array and connection between the fiber array and the detector, were not calibrated out from the measurement result. We did not calibrate out the insertion losses from the measurement system because we found that the uncertainty of the calibration process is around 1 dB, i.e., the tightness of

the connectors, the position of the fibers, the vibrations of the setup, etc. all have impacts on the accuracy of the calibration process. Given that the mismatch of between the simulated coupling efficiency and measured coupling efficiency is below 2 dB, we found it is not reasonable to calibrate the loss with an uncertainty at the same level as the loss we are trying to calibrate. In addition, the fiber array used for our measurement were intentionally polished to a larger angle than the required incident angle of the designed grating coupler. Therefore, the tip of the fiber array was not parallel to the surface of the grating coupler during measurement and an air gap existed between the fiber array and the chip surface. Such an air gap not only introduced excess loss but also narrowed the operating bandwidth of the measured grating coupler. The back reflection from the SWGC has been highly eliminated by using the SWGs, hence the ripples in our transmission spectrum caused by the Fabry-Perot cavity are significantly suppressed (< 0.25 dB), which is comparable to that of a shallow-etched grating coupler (about 0.1 dB). Due to fabrication inaccuracies, the measured central wavelength shifted to 1580 nm.

As shown in Table 2.1, the slope of l_{sub} is much larger than that of Λ and Λ_{H}. In addition, the value of l_{sub} (74 nm) is much smaller than the values of Λ (593 nm) and Λ_{H} (237 nm). The red shift of the spectrum is mainly caused by the fabrication inaccuracy in l_{sub}, though it may also be caused by the fabrication inaccuracies in Λ and Λ_{H}. The simulation results shown in Fig. 2.14 assumed that the central wavelength shift was caused by the fabrication imperfection in the SWGs, and a $\delta l_{\mathrm{sub}} = 15$ nm was assumed when the simulated central wavelength matches the measurement results. There were also mismatches in the coupling efficiency and the bandwidth between the simulated and measured results, which are mainly caused by

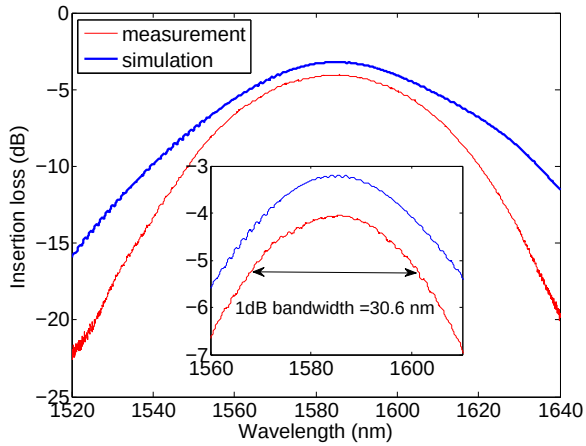

Figure 2.14: Simulated and measured transmission spectra of a fabricated TE SWGC assuming $l_{\text{sub}} = 89$nm; inset is the spectrum near the central wavelength.

the fiber array we used. We intentionally polished our fiber array with a large angle so that it can accommodate for various incident angles. The required θ for the TE SWGC and the TM SWGC were smaller than the polished angle, so the chip surface and the fiber tip were not parallel during the measurement. Therefore, an inevitable gap was introduced between the fiber tip and measured chip, which leads to a lower coupling efficiency and a smaller bandwidth. In addition, extra losses were also introduced from the transmission lines (optical fibbers) and the interfaces of the connectors used in the measurement system, which have not been calibrated out from the measurement results.

TM SWGC

The measurement results for the TM SWGCs are shown in Fig. 2.15. The measured transmission spectra of 11 TM SWGCs with the same design parameters are shown in Fig. 2.15(a). The inset of the graph shows the zoomed

spectra near the central wavelength. Fig. 2.15(b) and (c) show the comparison of the measured coupling efficiencies and 1-dB bandwidths of the 11 TM SWGCs with the simulated results. The green lines denote the simulation results and the blue diamonds and circles denote the measurement results extracted from the spectra shown in Fig. 2.15(a). The coupling efficiencies of the 11 TM SWGCs ranged from $-3.7\,\mathrm{dB}$ to $-3.8\,\mathrm{dB}$ with 1-dB bandwidth ranging from 45.8 nm to 47.5 nm, which shows good performance stability and device repeatability. The best device has an coupling efficiency of $-3.7\,\mathrm{dB}$ with a 1-dB bandwidth of 47.5 nm (3-dB bandwidth of 81.5 nm). Figure 2.15(d)-(f) show the measured transmission spectra of TM SWGCs with various values of Λ, Λ_{H}, and l_{sub}. The offsets versus central wavelength shifts of those design parameters have been shown in Fig. 2.13 and the linear-fits of those design parameters have been given in Table. 2.1. The central wavelengths of the TM SWGCs were proportional to Λ, Λ_{H}, and l_{sub}. The TM SWGCs did not have large central wavelength shifts as the TE SWGCs did for two reasons. The first reason is that the feature sizes of the SWGs in the TM SWGCs were much larger than the TE SWGC, which makes it less challenging for the fabrication process. The second reason is that, according to the linear-fits shown in Table. 2.1, the central wavelength of the TM SWGC is less sensitive to variations in Λ, Λ_{H}, and l_{sub}, which is caused by the weak confinement of the TM mode.

To summarize, in this section, we have demonstrated compact SWGCs for both the TE_0 mode and the TM_0 mode. The back reflections from our SWGCs have been significantly suppressed compared to the regular fully-etched grating couplers. It has also been shown by the simulation and experimental results that one-dimensional SWGs is an alternative to the two-dimensional SWGs to achieve effective index medium with better

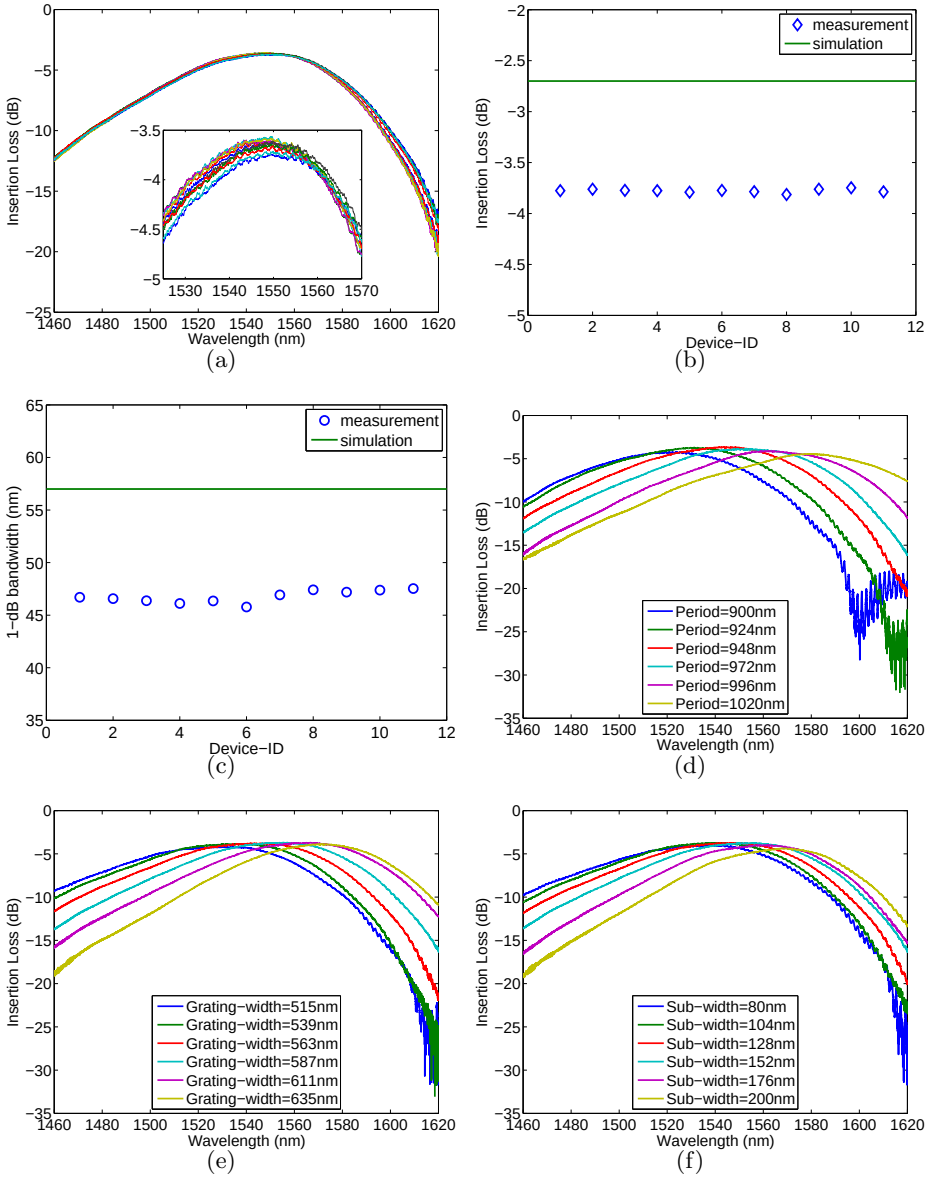

Figure 2.15: (a) Measured spectra of 11 TM SWGCs; (b) comparison of measured and simulated coupling efficiencies of the TM SWGCs; (c) comparison of the measured and simulated 1-dB bandwidths of the TM SWGCs; (d) measured spectra of TM SWGCs with various Λ_{H} values; (e) measured spectra of TM SWGCs with various Λ values; (f) measured spectra of TM SWGCs with various l_{sub} values.

fabrication accuracy and less complexity. Our TE SWGC had a measured peak coupling efficiency of −4.1 dB with a 1-dB bandwidth of 30.6 nm (3-dB bandwidth of 52.3 nm) and the TM SWGC had a measured peak coupling efficiency of −3.7 dB with a 1-dB bandwidth of 47.5 nm (3-dB bandwidth of 81.5 nm). Further improvement can be made by apodizing the grating periods, which will be shown in the next section.

2.2 Apodized Sub-wavelength Grating Couplers

Uniform gratings have been used in Section 2.1, where higher coupling efficiencies can be obtained for both the TE SWGC and the TM SWGC by apodizing the gratings to achieve better mode match between the grating and the optical fiber. The maximum theoretical coupling efficiency for a grating coupler with uniform gratings is nearly 80% [56], which means that the coupling efficiency of a grating couplers with uniform gratings can be improved by about 1dB using non-uniform gratings. In this section, we compare two different approaches to apodize SWGCs to reduce the mode mismatch loss and we experimentally demonstrate apodized SWGCs with improved coupling efficiencies for both the TE_0 and the TM_0 modes.

2.2.1 Design and Simulation

To achieve a Gaussian output beam, the leakage factor, α, is given by [74]:

$$\alpha(z) = \frac{G^2(z)}{2 \cdot (1 - \int_0^z G^2(t)dt)} \tag{2.6}$$

where G(z) is a normalized Gaussian profile determined by the fiber mode and z denotes the distance in the propagation direction. α of an SWGC

can be tuned by changing Λ_{H} and l_{sub} of the SWGC. Figure. 2.16(a) shows α as functions of Λ_{H} and l_{sub} for the TE SWGC that we obtained from Section 2.1. Figure. 2.16(b) shows α as functions of Λ_{H} and l_{sub} for the TM SWGC that we obtained from Section 2.1. To obtain the simulation results shown in Fig. 2.16, we kept all the other design parameters as constants when we swept Λ_{H} and l_{sub}, respectively. From Fig. 2.16 we can see that by changing l_{sub}, a larger tuning range for α can be obtained for our SWGCs, so we used the l_{sub} as the tuning factor to modify the α of our SWGCs.

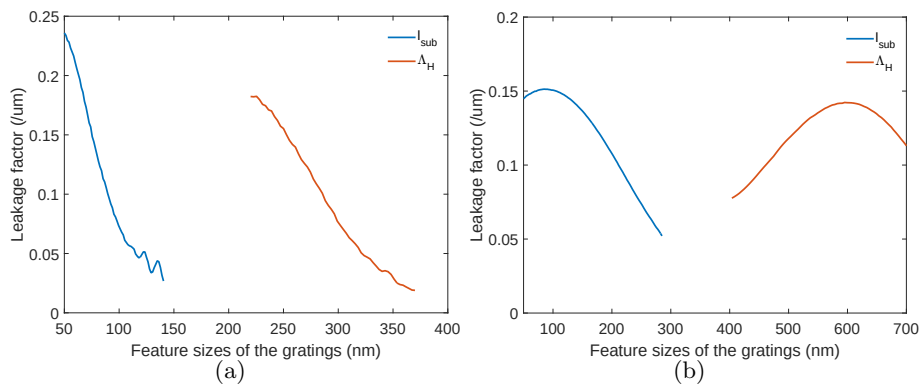

Figure 2.16: α as functions of l_{sub} and Λ_{H} for the TE SWGCs, and (b) α as functions of l_{sub} and Λ_{H} for the TM SWGCs.

With the relations shown in Fig. 2.16 and Eq. 2.2, we can get the required l_{sub} as a function of z. It should be noted that Eq. 2.2 is only accurate for long gratings with small α, which is not the case for our SWGCs. So we used the calculated l_{sub} as the starting point for further optimization. In order to achieve the phase-match condition between the adjacent grating periods, Λ also need to be modified. We used PSA in *FDTD Solutions* to optimize the values of l_{sub} and Λ for each grating period to achieve the maximum coupling efficiency. Each grating period has been treated as a

separate grating section for optimization starting from the interface of the waveguide and the grating. The optimized Λ and l_{sub} for each apodized grating section are shown in Table 2.2. Eight grating periods are required to be apodized for the TE SWGC and four grating periods are required to be apodized for the TM SWGC, which is due to the fact that the Λ of the TM SWGC is larger than that of the TE SWGC.

Table 2.2: Λ and l_{sub} values for the apodized SWGCs.

TE SWGC				**TM SWGC**			
Λ_1 (nm)	480	l_{sub1} (nm)	120	Λ_1 (nm)	895	l_{sub1} (nm)	220
Λ_2 (nm)	516	l_{sub2} (nm)	120	Λ_2 (nm)	895	l_{sub2} (nm)	189
Λ_3 (nm)	500	l_{sub3} (nm)	120	Λ_3 (nm)	917	l_{sub3} (nm)	173
Λ_4 (nm)	521	l_{sub4} (nm)	120	Λ_4 (nm)	914	l_{sub4} (nm)	200
Λ_5 (nm)	500	l_{sub5} (nm)	120				
Λ_6 (nm)	560	l_{sub6} (nm)	108				
Λ_7 (nm)	500	l_{sub7} (nm)	100				
Λ_8 (nm)	560	l_{sub8} (nm)	71				

2.2.2 Design of Apodized SWGCs

A parameterized device cell has been created in *Mentor Graphics's Pyxis* [18] to generate the layout files for various apodized SWGCs. The mask layouts were first exported from *Mentor Graphics*'s *Pyxis* and then imported into *FDTD Solutions* for 3D simulation. 3D FDTD simulations were done for the focusing SWGCs for both the TE_0 and the TM_0 modes. These simulations have been done for both apodized and un-apodized SWGCs for comparison purposes. Fig. 2.17(a) shows the simulated transmission and reflection spectra of the apodized and un-apodized SWGCs for the TE_0 mode. The apodized TE SWGC has a peak coupling efficiency of -2.1 dB, 0.6 dB lower than the un-apodized design, and a 1-dB bandwidth of 42 nm.

The reflections from the apodized and un-apodized SWGCs are both below -20 dB. Fig. 2.17(b) shows the simulated transmission and reflection spectra of the apodized and un-apodized SWGCs for the TM_0 mode. The apdized TM SWGC has a peak coupling efficiency of -2.2 dB, 0.7 dB lower than the un-apodized design, and a 1-dB bandwidth of 45 nm.

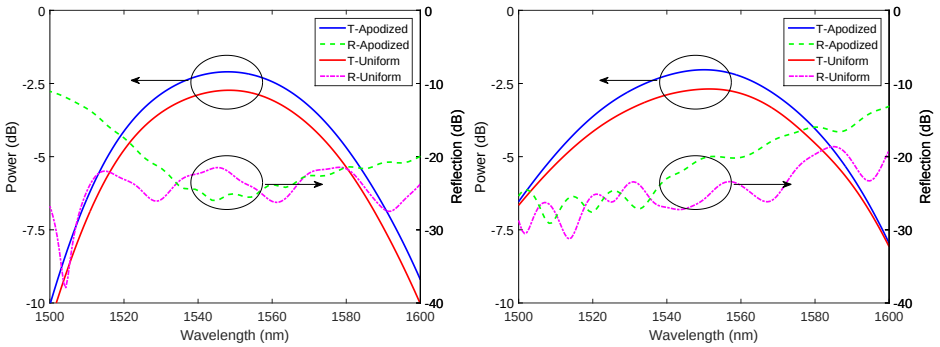

(a) (b)

Figure 2.17: Simulated coupling efficiencies and back reflections of the apodized and the un-apodized (a) TE SWGCs using 2D FDTD simulation, and (b)TM SWGCs using 2D FDTD simulation.

The principal loss in our SWGCs is the penetration loss to the substrate, which can be reduced by optimizing the thickness of the BOX or by adding a bottom mirror at the interface of the BOX and the silicon substrate. The optimization of our design parameters are based on the silicon wafer used for fabrication, which has a 220 nm silicon layer and a 3 µm BOX layer. Both the silicon thickness and the BOX thickness are not optimized to achieve high coupling efficiencies for our SWGCs. If we include the thickness of the BOX layer in our optimization process, then the coupling efficiencies of the SWGCs can be improved to be -1.5 dB and -1.7 dB, respectively (shown in Fig. 2.18). Furthermore, if we include a bottom mirror (i.e., either a metal mirror or a Bragg reflector) in our SWGCs, then the coupling efficiencies of

our TE SWGC and TM SWGC can be improved to −0.34 dB and −0.41 dB, respectively (show in Fig. 2.18). The back reflections can be further reduced using the technique demonstrated in [78], which is focusing the reflected light away from the entrance waveguide. It should be noted that the operating bandwidths of SWGCs are affected by apodizations. According to [16], the bandwidth of the grating coupler is proportional to Λ of the grating coupler. The Λ values in the apodized region of the TM SWGC decreases from 960 nm to 872 nm, which causes the decrease in bandwidth. Compared to the TM SWGC, the Λ values in the apodized regions of the TE SWGC only decreases from 556 nm to 505 nm. In addition, the back reflection from the apodized TM SWGC is larger than that of the un-apodized design, which is caused by the increased index contrast in the apodized region.

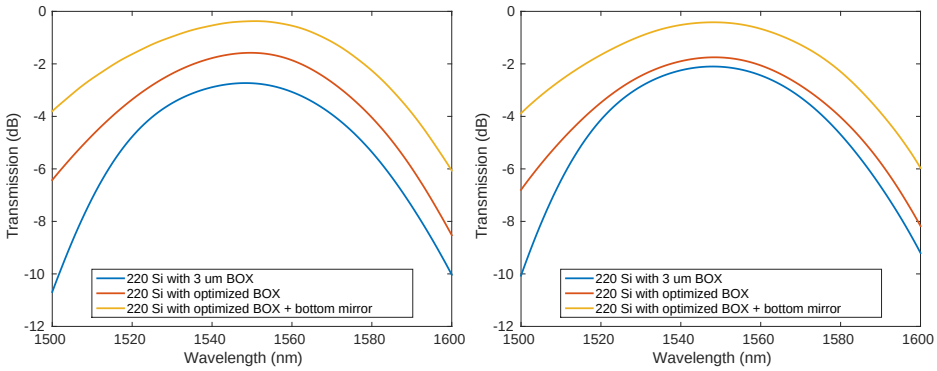

Figure 2.18: Simulated transmission spectra of (a) the apodized TE SWGCs, and (b) the apodized TM SWGCs.

2.2.3 Measurement Results

TE SWGCs

Figure. 2.19(a) shows the calibrated transmission spectra of an apodized and a un-apodized TE SWGCs. An HP 81525A high power optical head was used to calibrate the loss from the measurement system, including the loss in the fiber array, the connectors, and the additional fibres used for extension. The apodized design has a peak coupling efficiency of -3.2 dB, 0.6 dB higher than the un-apodized one, with a 1-dB bandwidth of 36 nm, which is similar to that of the un-apodized design. The ripple at the central wavelength of the apodized TE SWGC is about 0.07 dB, which corresponds to a back reflection of -24 dB. The highly suppressed back reflection from our SWGC is comparable to the state of the art shallow-etched grating couplers [51]. The same designs are fabricated multiple times on the same chip to test the performance stability. Figures 2.19(b)-(d) show the coupling efficiencies, 1-dB bandwidths, and the central wavelengths of apodized and un-apodized TE SWGCs having the same designs and measured at different locations on a particular chip. It should be noted from this comparison, that, the stabilities of the coupling efficiency, the bandwidth, and the central wavelength of the un-apodzied SWGCs are better than their stabilities for the apodized ones. This is the case because the apodized grating will only work if all of the apodized grating periods are in phase. Even a few nanometers offset in l_{sub} can degrade the performance of the SWGCs. Never the less, and despite the reduced stability, the average coupling efficiency of the apodized SWGCs was about 0.6 dB higher than the average coupling efficiency of un-apodized SWGCs with similar bandwidths and central wavelengths.

Corner analysis has been applied to predict the range of the key char-

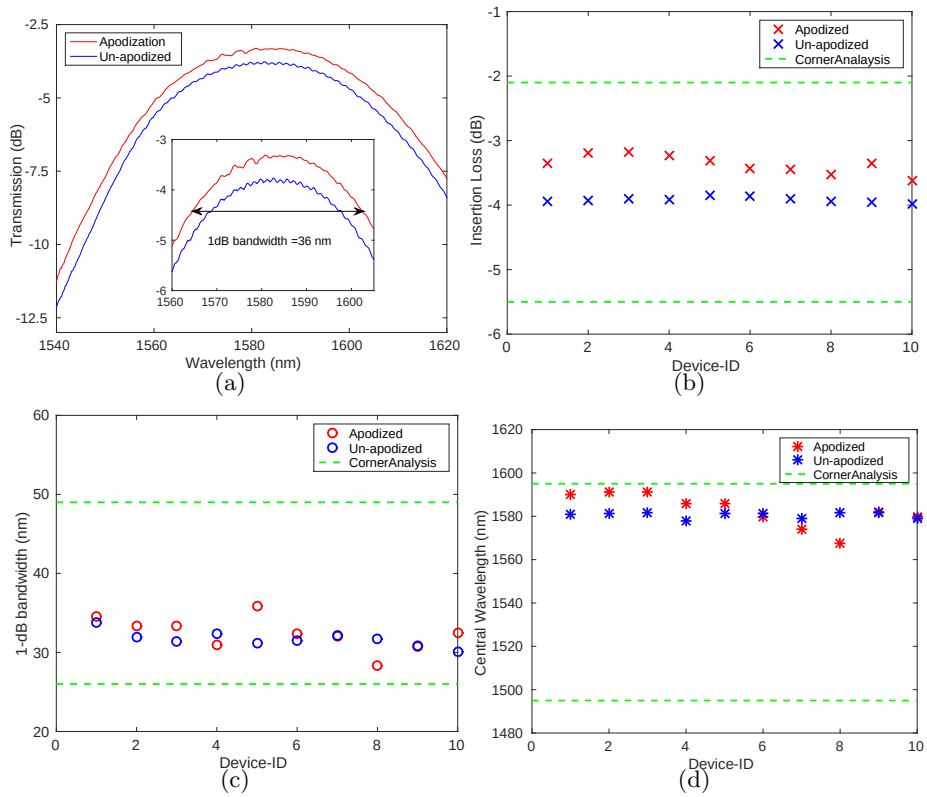

Figure 2.19: (a) Measured spectra of an apodized TE SWGC and an un-apodized TE SWGC; (b) coupling efficiencies of apodized and un-apodized TE SWGCs; (c) 1-dB bandwidths of apodized and un-apodized TM SWGCs; (d) central wavelengths of the apodized and un-apodized TE SWGCs.

acteristics of the as-designed SWGCs. Six parameters, θ, Λ_{H}, l_{sub}, the thickness of the silicon layer (Si), thickness of the BOX, and thickness of the oxide cladding (SiO_2) have been used in the corner analysis as shown in Table 2.3. The first three parameters shown in Table 2.3 mainly affect the central wavelength and the bandwidth of an SWGC, and the last three parameters shown in Table 2.3 mainly affect the coupling efficiencies of an SWGC, since they change the interference condition of the light diffracted by the grating. The gap between the fiber tip and the chip surface is another

important parameter that affect the coupling efficiency and bandwidth of an SWGC. Given the fact that we use angle polished fibers and leaving sufficient space to avoid scratching the chip surface, the gap between the fiber core and the chip surface is kept at about 15 µm. A 15 µm gap is also used in the corner analysis (Table 2.3). According to our simulation, the extra loss caused by this gap is about 0.5 dB. The measured coupling efficiencies can be further improved by polishing the fiber array to a particular angle so that the fiber tip and the chip surface can be parallel during the measurement. The dashed green lines in Figs. 2.19(b)-(d) denote the simulated boundaries in the corner analysis.

Table 2.3: Parameters used for corner analysis for SWGCs.

$\delta\theta$	$\delta\Lambda_{\mathbf{H}}$	$\delta l_{\mathbf{sub}}$	δ**Si**	δ**BOX**	δ**SiO**$_2$
$\pm$ 2°	$\pm$ 10 nm	$\pm$ 10 nm	$\pm$ 10 nm	$\pm$ 20 nm	$\pm$ 100 nm

TM SWGC

Figure 2.20 shows the calibrated measurement results for the TM SWGCs. Figure. 2.20(a) shows the measured transmission spectra of an apodized TM SWGC and a un-apodized TM SWGC. The apodized TM SWGC has a coupling effciency of −3.3 dB, 0.6 dB higher than the un-apodized one, with a 1-dB bandwidth of 37 nm. The ripple at the central wavelength is about 0.15 dB, which corresponds to a back reflection of −21 dB. Figures 2.20(b)-(d) show the coupling efficiencies, 1-dB bandwidths, and the central wavelengths of the apodized and un-apodized TM SWGCs having the same designs and measured at different locations on a particular chip. Both the apodized and un-apodzied TM SWGCs have good stability and reproducibility. This is

the case because the TM_0 mode is less sensitive than the TE_0 mode to the design parameter variations. The average coupling efficiency of the apodized TM SWGCs is about 0.6 dB higher than the average coupling efficiency of the un-apodized TM SWGCs. Same corner analysis have been done for the TM SWGCs, and a 30 µm gap was assumed in the simulation. The enlarged gap is caused by the increased angle difference between the polished angle and the required incident angle by the TM SWGCs.

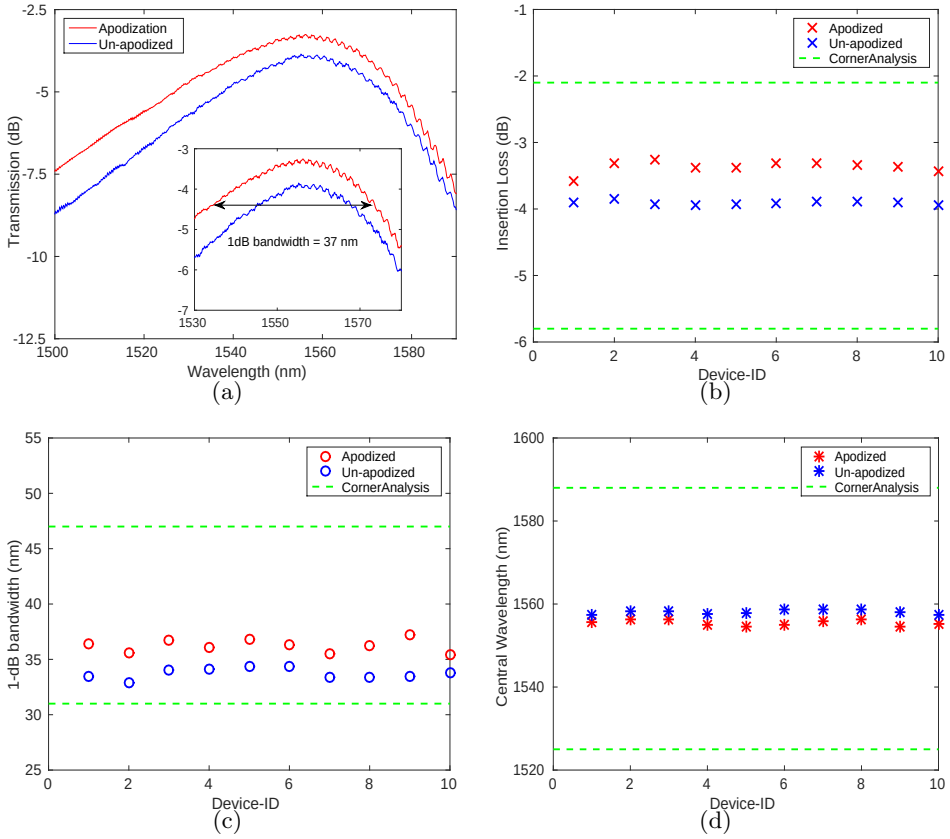

Figure 2.20: (a) Measured spectra of an apodized TM SWGC and an un-apodized TM SWGC; (b) coupling efficiencies of apodized and un-apodized TM SWGCs; (c) 1-dB bandwidths of apodized and un-apodized TM SWGCs; (d) central wavelengths of the apodized and un-apodized TM SWGCs.

As compared to the measured spectral response of the TE SWGCs, an asymmetry can be observed in the spectral response of the TM SWGCs, which is due to the fact that the surface of the fiber tip and the grating surface were not parallel during the measurement. The fiber ribbon used in our measurement has a polish angle of 23.2°, which means that we need to tilt the fiber ribbon by 24° to get the required incident angle for the TM SWGCs. Therefore, an acute angle exists between the fiber tip and the surface of the grating. Incident waves at different wavelengths are diffracted at different angles by the grating. Longer wavelengths are not coupled into the fiber as efficiently as shorter wavelengths, which results in the asymmetry observed in the spectra.

To summarize, in this section, we have experimentally demonstrated the apodized focusing SWGCs for both the TE_0 and TM_0 modes, which show a consistent improvement over the un-apodized designs. Corner analysis have been applied to the SWGCs, which shows that our devices are robust considering the manufacturing variations assumed. As the resolution of the CMOS fabrication becomes smaller, those SWGCs can even become alternatives to the shallow-etched grating couplers; therefore the fabrication cost and complexity can be reduced.

Chapter 3

Broadband Sub-wavelength Grating Couplers

Significant effort has been devoted to improve the coupling efficiency of grating couplers [24, 29, 50, 54, 79, 84, 85, 99], while only a few attempts have been made to improve the operating bandwidths [16, 89, 90, 95, 101]. In this chapter, the study on the operating bandwidth for a grating coupler is shown first. Then we present a methodology to obtain SWGCs with design-intent bandwidths. Finally, we experimentally demonstrate broadband SWGCs with both straight and focusing SWGs.

3.1 Bandwidth Analysis

Thorough bandwidth analyses of grating couplers have been presented in [89, 90], where the bandwidth of a grating coupler was attributed to the mismatch of the effective indices between the diffracted beam and the actual grating structure. Alternatively [16], the bandwidth of a grating coupler can be attributed to the wavelength dependent diffraction angle of the grating coupler. SWGs have been used to improve the bandwidths of grating couplers [16, 95, 101]. A schematic of the cross-section of a broadband SWGC is shown in Fig. 3.1.

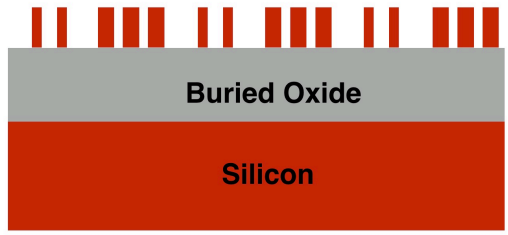

Figure 3.1: Schematic of the cross-section of a broadband SWGC with one-dimensional SWGs.

The phase-match condition for grating couplers, shown in Eq. 2.1, can also be expressed as [96]:

$$k_0 \cdot n_{\text{eff}} = k_0 \cdot n_{\text{c}} \cdot sin(\theta) + m \cdot \frac{2\pi}{\Lambda} \tag{3.1}$$

where $k_0 = \frac{2\pi}{\lambda}$, n_{eff} is the effective index of the grating, n_c is the refractive index of the cladding, θ is the incident angle in free space, Λ is the grating period, and m is an integer denoting the diffraction order (here m=1). We estimate the 1-dB bandwidth of a grating coupler using the wavelength dependent diffraction angle:

$$\Delta\lambda_{\text{1dB}} = \Delta\theta_{\text{1dB}} \cdot 2|\frac{d\lambda}{d\theta}| \tag{3.2}$$

where $\Delta\theta_{\text{1dB}}$ is a constant that depends solely on the fiber parameters and the calculated results match well with the measurement when $\Delta\theta_{\text{1dB}}$ equals 0.047. $|\frac{d\lambda}{d\theta}|$ can be obtained from Equation 3.1 and the factor of 2 accounts for the 1-dB bandwidth including the wavelength range both above and below the central operating wavelength. From Eq. 3.1, Λ can be expressed

as:

$$\Lambda = \frac{\lambda}{n_{\text{eff}} - n_c \cdot sin(\theta)} \tag{3.3}$$

We also know that n_{g} is defined as [96] :

$$n_{\text{g}} = n_{\text{eff}} - \lambda \frac{dn_{\text{eff}}}{d\lambda} \tag{3.4}$$

Using Eqs.2.2 - 2.4, $\Delta\lambda_{\text{1dB}}$ becomes:

$$\Delta\lambda_{\text{1dB}} = \Delta\theta_{\text{1dB}} \cdot 2|\frac{-\ n_{\text{c}} \cdot cos(\theta) \cdot \lambda}{n_{\text{g}} - n_{\text{c}} \cdot sin(\theta)}| \tag{3.5}$$

Given that $\Delta\theta_{\text{1dB}}$ and n_{c} are constants, we can see that the bandwidth is only dependent on n_{g} and θ for a given λ. Equation 3.5 shows us that the 1-dB bandwidth of a grating coupler can be increased by reducing the n_{g} of the grating. For a given n_{g}, an optimal θ, that gives the largest bandwidth, can also be calculated using Eq. 3.5.

3.2 Design Methodology

Our design methodology follows a four-step process. In the first step, we have derived an expression for the 1-dB bandwidth of a grating coupler, that depends on the group index, n_{g}, and θ of a grating coupler. Based on the derived expression, a specific θ is chosen for further design optimization. Then three more steps are followed to finalize various design parameters using the particle swarm algorithm [62] and effective medium theory (EMT) [28].

The optimal incident angle, θ_{opt}, as a function of n_{g} is shown in Fig. 3.2, for values of n_{g} between 2.2 and 4.2; the simulated n_{g} for a un-etched silicon

waveguide is about 4.2, and the simulated n_{g} for a one-dimensional SWG with an overall fill factor of 0.2 is about 2.2. (where the material dispersion was not included in the calculation due to the fact that we used a constant refractive index for the estimation based on EMT). As mentioned above, if we wish to increase the bandwidth, a larger θ is required. Here, we chose $\theta = 25°$, which is the optimal θ for an n_{g} near the middle of the n_{g} range from 2.2 to 4.2.

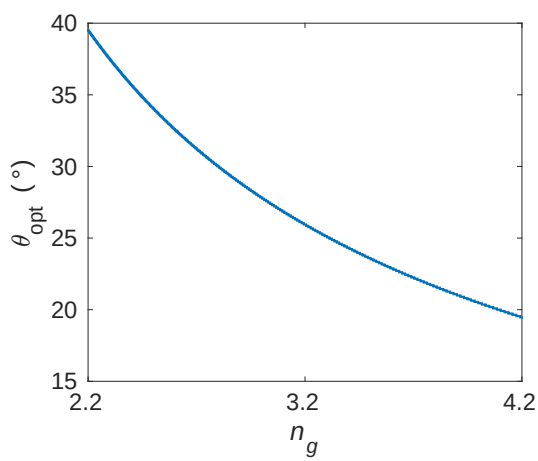

Figure 3.2: Optimal incident angle, θ_{opt}, as a function of the group index of a grating coupler, n_{g}.

As will become apparent from the discussion, the subsequent optimizations of our SWGC design parameters begins with the structure shown in Fig. 3.3(a). Our SWGCs are designed based on SOI wafers with 220 nm silicon layer and 3 µm BOX layer. Here, the grating of our SWGC is modelled as alternating regions of high and low refractive indices, where each grating period consists of a high index region with a refractive index of n_H and a low index region with a refractive index of n_L. The lengths of n_H and n_L are denoted as Λ_H and Λ_L. The length of the grating period is Λ, where $\Lambda = \Lambda_H + \Lambda_L$. The lengths of the SWGs in the high and the low index

regions are denoted as l_H and l_L, as shown in Fig. 3.3(b). The fill factor of the grating coupler, ff, is defined as the ratio of Λ_H to Λ. The numbers of gratings in each high and low index region are N_H and N_L, respectively. The fill factors of the high and low index regions, denoted as ff_H and ff_L, are defined as $N_H * l_H/\Lambda_H$ and $N_L * l_L/\Lambda_L$, respectively.

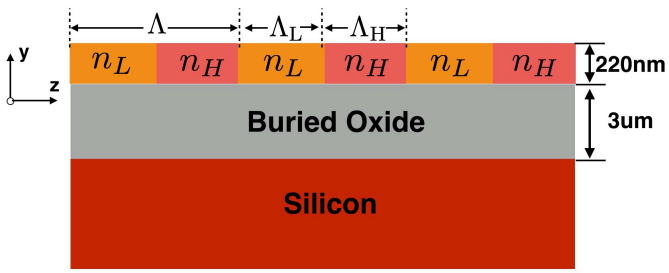

(a)

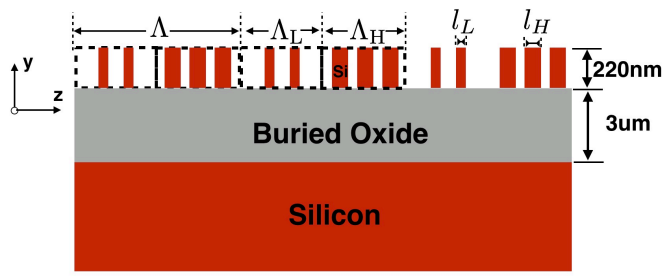

(b)

Figure 3.3: Schematics of (a) an SWGC with refractive index regions of n_{H} and n_{L}, (b) an SWGC with one-dimensional SWGs.

The two-dimensional FDTD method is used to optimize the design parameters of our SWGCs. A figure of merit (FOM), defined as the product of the 1-dB bandwidth and the coupling efficiency, is used to predict the performance of an SWGC. Having chosen $\theta = 25°$, we have completed the first step in our design methodology. We now optimize our SWGC design in three more steps. In the second step, we optimized four design parameters, Λ, ff , n_H, and n_L, to achieve the maximum FOM using the PSA in *FDTD Solu-*

tions. The design parameters, with the largest FOM for θ =25° are shown in row 2 of Table 3.1. In the third step, using our optimized n_H and n_L from the second step, ff_H and ff_L are calculated using zeroth-order EMT [14, 28]. The dimensions of the SWGs have both a lower limit, which comes from the fabrication limitations, and an upper limit, which is determined using EMT. Since the calculated ff_L and ff_H are only approximations, further optimizations with boundary conditions are done using the PSA, as before, with the optimized values shown in row 3 of Table 3.1. Finally, we determined the number of SWGs in the high and low index regions, i.e., N_H and N_L. The dimensions of the SWGs should be small enough to allow EMT to work and large enough to be fabricated. Based on the optimized values of ff_H and ff_L, we simulated the allowed combinations of N_H and N_L, and have given the optimized values in the last row of Table 3.1.

Table 3.1: Optimization steps and design parameters

Step 1:	$\theta = 25°$			
Step 2:	Λ =1130 nm	ff =0.5	n_H = 2.78	n_L = 1.8
Step 3:	ff_H=0.49	ff_L= 0.13		
Step 4:	N_H= 3	N_L=2		

The simulated transmission and reflection spectra of the optimized SWGC, having the parameters given in Table 3.1, are shown in Fig. 3.4. Since all of the design optimizations are done using 2D FDTD simulations, we then verify the designs using 3D simulations. The simulated transmission spectra for both the 2D and the 3D simulations are shown in Fig. 3.5(a). The simulated reflection spectra of the straight and focusing SWGCs are also shown in Fig. 3.5(a). As compared to the straight SWGC, the back reflection from the focusing SWGC is smaller, which means that the focusing design not only reduces the footprint, but also suppresses the back reflection. The SWGC

has an coupling efficiency of $-3.6\,\mathrm{dB}$ and a 1-dB bandwidth of $84\,\mathrm{nm}$. The FOM is defined as:

$$\mathrm{FOM} = \frac{\text{1-dB bandwidth } (nm)}{100\ (nm)} \cdot CE(\%) \tag{3.6}$$

which takes both the bandwidth and coupling efficiency into consideration, the result being that the SWGC with the largest FOM may not necessarily have the largest bandwidth.

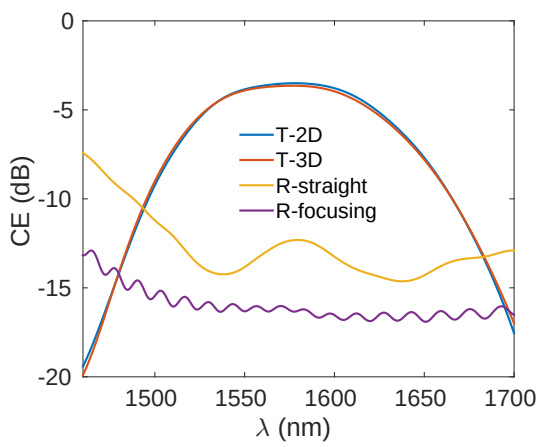

Figure 3.4: Simulated transmission and reflection spectra of the SWGC with the design parameters shown in Table 3.1.

Based on the design parameters in Table 3.1, we simulated the 1-dB bandwidths and the peak coupling efficiencies as we varied ff_L. As we varied ff_L, ff_H was also varied such that the operating wavelength of the grating coupler remained constant. Fig. 3.5 shows the simulated 1-dB bandwidth and peak coupling efficiency as a function of ff_L. We can see that the bandwidth of the grating coupler is inversely proportional to ff_L, and that broader bandwidths can be achieved with smaller ff_L values. However, the minimum ff_L is determined by the minimum feature size provided by the fabrication facility.

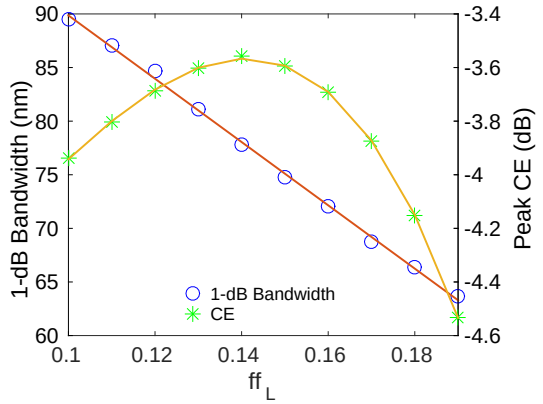

Figure 3.5: Simulated 1-dB bandwidth and peak coupling efficeincy as a function of $f f_{\mathrm{L}}$.

3.3 Measurement Results

Test structures, consisting of an input SWGC and an output SWGC, connected by a strip waveguide, were fabricated using electron beam lithography at the University of Washington [11]. Since it is known that focusing SWGCs are more space-efficient than straight SWGCs, both types were fabricated for comparison purposes. The purpose of comparing them is to determine which has the higher FOM and, also, to confirm whether the focusing SWGC has a lower back reflection than the straight SWGC. The straight SWGCs are 12 µm wide and in order to keep the total device length to a reasonable number, we used 150 µm long tapers to couple the light from the grating to the 500 nm wide waveguide. The focusing SWGCs were generated using the method demonstrated in [77, 85]. Scanning electron microscope (SEM) images of the as-fabricated straight and focusing SWGCs are shown in Fig. 3.6.

Based on the simulation results shown in Fig. 3.5(b), design variations were fabricated as shown in Table 3.2. The fabricated devices were measured using our fiber-array-based automated measurement setup, the fiber

array was polished at 24.7° to accommodate the required incident angles. Figure 3.7 shows the measured transmission spectra of the focusing and straight SWGCs with ff_L=0.1 and ff_H=0.52. The simulated transmission spectrum, using the same grating design as the measured device, is shown in the same figure. The measured focusing and straight SWGCs, have maximum coupling efficiencies of −5.5 dB and −5.8 dB, respectively. Both have 1-dB bandwidths of 90 nm, with central wavelengths of about 1578 nm.

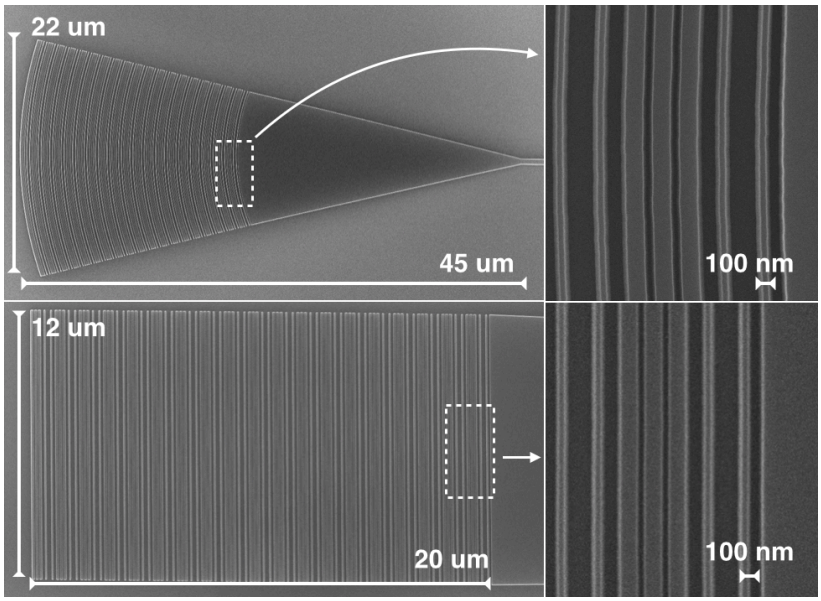

Figure 3.6: SEM images of the as-fabricated focusing and straight SWGCs. (For the straight SWGC, the taper is not shown.)

Table 3.2: Design variations

Focusing Grating	ff_L:	0.1 - 0.19	ff_H:	0.52 - 0.43
Straight Grating	ff_L:	0.1 - 0.18	ff_H:	0.52 - 0.44

The coupling efficiency of the straight SWGC is lower than that of the focusing one because we used a short linear taper in it. The length of the linear tapers used in our straight SWGC are 150 µm, which is not long

enough to allow adiabatic coupling between the grating and the waveguide. It should be noted that the oscillation ripples in the spectrum of the focusing SWGC are smaller than those in the spectrum of the straight SWGC, which confirms that the focusing design not only reduces the footprint of the device, but also suppresses the back reflection from the grating. This is the case because the focal point of the reflected wave is away from the entrance of the waveguide, and such technique is detailed in [78]. The ERs of the ripples near the central wavelength of the focusing SWGC are about 0.08 dB, which correspond to back reflections of less than −23 dB, whereas the ERs of the ripples near the central wavelength of the straight SWGC are about 0.2 dB, which correspond to back reflections of less than −19 dB. In addition, the back reflection of the focusing SWGCs are more consistent over the 1-dB bandwidth wavelength range, while the back reflection of the straight SWGCs increases gradually as the wavelength decreases, which matches the simulation results shown in Fig. 3.4.

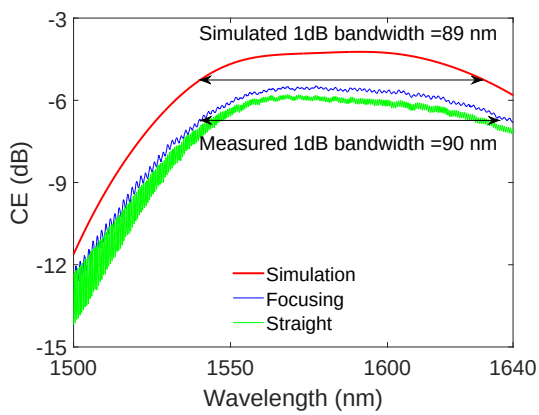

Figure 3.7: Transmission spectra of the simulated SWGC (red), the measured focusing SWGC (blue), and the measured straight SWGC (green).

Figure 3.8 shows the measured 1-dB bandwidths and coupling efficiencies

of the fabricated focusing and straight SWGCs with the design variations shown in Table 3.2. For the focusing SWGCs, as ff_L changed from 0.1 to 0.19, the 1-dB bandwidths changed from 90 nm to 48 nm and the coupling efficiencies varied between −5.5 dB and −3.8 dB. For the straight SWGCs, as ff_L changed from 0.1 to 0.18, the 1-dB bandwidths changed from 90 nm to 48 nm and the coupling efficiencies varied between −5.8 dB and −4.2 dB. The measured 1-dB bandwidths of both focusing and straight SWGCs follow the same trend as shown in Fig. 3.5(b) except that the slope of the measured 1-dB bandwidth variations were slightly larger than those of the simulations. The increased slope may result from the fact that the $\Delta\theta_{1\mathrm{dB}}$ of the fiber model that we used in the simulations is smaller than the $\Delta\theta_{1\mathrm{dB}}$ of the fibers that we used in the measurements. The measured coupling efficiencies of the focusing and straight SWGCs are lower than the simulated results, which may come from several sources, such as the measurement system, fabrication errors, *etc.* In addition, the measured peak coupling efficiency corresponds to a larger ff_L than was used in the simulation, which may come from the fact that the ff_Ls of the fabricated devices were smaller than the design values.

In conclusion, in this chapter we presented a methodology to design broadband SWGCs using one dimensional SWGs. Both straight SWGCs and focusing SWGCs with 1-dB bandwidths of 90 nm are designed and fabricated. Back reflections from the SWGCs are suppressed by using focusing SWG designs, and a measured back reflection below −23 dB is achieved, which is comparable to state of the art shallow-etched grating couplers [78].

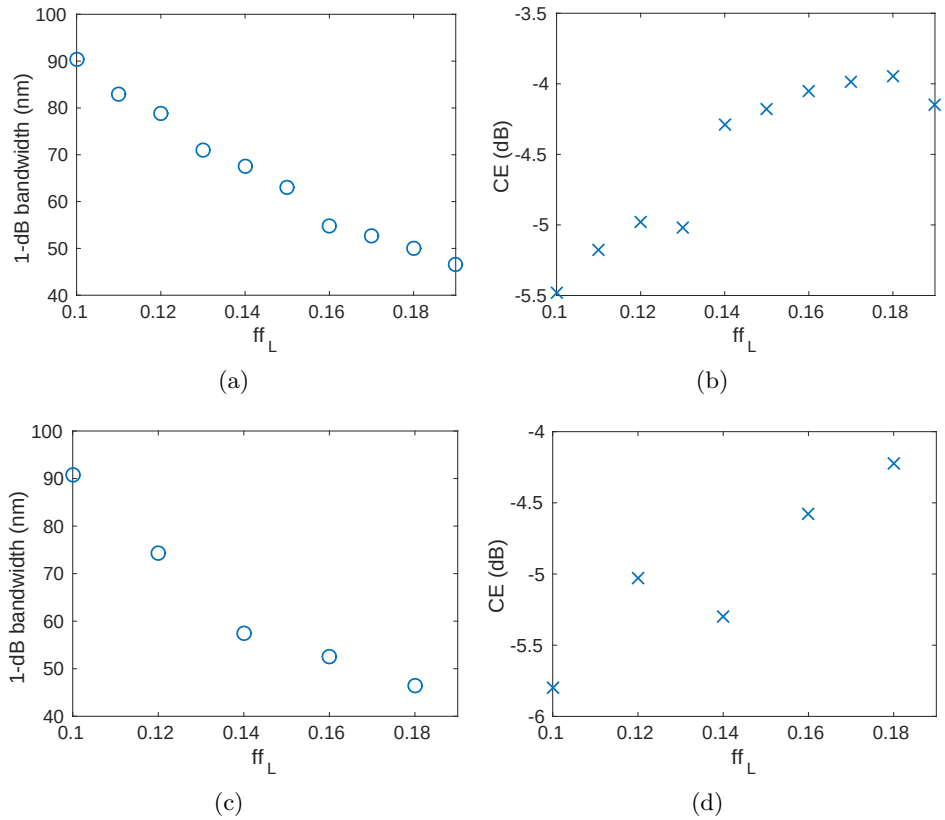

Figure 3.8: Measured (a) 1-dB bandwidths and (b) coupling efficiencies of the fabricated focusing SWGCs with ff_L ranging from 0.1 to 0.19; measured (c) 1-dB bandwidths and (d) coupling efficiencies of the fabricated straight SWGCs with ff_L ranging from 0.1 to 0.18.

Chapter 4

Broadband Sub-wavelength Directional Couplers

Sub-wavelength gratings (SWGs) provide the flexibility to engineer both their index profiles and their dispersion properties, which have been proposed to engineer the wavelength dependency of a conventional directional coupler (DC) for broad operating bandwidth [30]. However, the theoretical study shown in [30] was based on SOI wafers with 260 nm silicon layer, which is different than the 220 nm SOI wafters that are more commonly used by MPW foundry services. In addition, the minimum feature size in the proposed structure is only about 60 nm, which is challenging to fabricate even with the most advanced electron beam lithography [11].

In this chapter, we elaborate on the proposed work in [30] by experimentally demonstrating more compact broadband DCs using SWGs, with various power splitting ratios, for SOI wafers with silicon layers of 220 nm. The minimum feature size of our design is increased to 80 nm, which can be easily fabricated with electron beam lithography. The design can be also modified to have minimum feature size around 100 nm, which can be fabricated with CMOS technology using optical lithography [43]. In addition, a design methodology using FDTD-based band structure calculations is presented to design our SWG DCs.

A schematic of our SWG DC is shown in Fig. 4.1, which consists of a conventional DC with waveguide widths, w, separated by a spacing, g, and SWGs with a period, Λ, and a fill factor, ff, where ff is defined as the ratio of l_{sub} to Λ, and l_{sub} is the length of one grating tooth. The SWGs are extended outside of the waveguides by a distance, t. S bend waveguides are used at the input and output ports to decouple the two parallel waveguides.

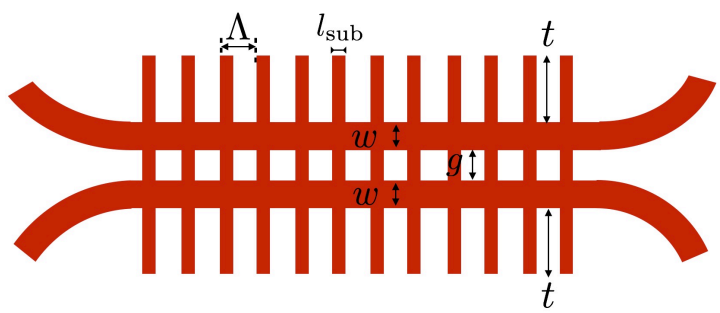

Figure 4.1: Schematic of an SWG DC with design parameters labelled.

4.1 Wavelength Dependency of Directional Couplers

A conventional DC consists of two parallel waveguides, where the coupling coefficient is controlled by both the length of the coupling region and the spacing between the two waveguides. The behaviour of a DC can be explained based on the phase matching condition between the TE_0 mode and the TE_1 mode of the two waveguide system. The TE_0 mode is also know as the even "supermode" or the symmetric mode and the TE_1 mode is also known as the odd "supermode" or the antisymmetric mode of the two waveguide system. The field profile for the TE_0 mode and the TE_1 mode

for a conventional DC are shown in Fig. 4.2.

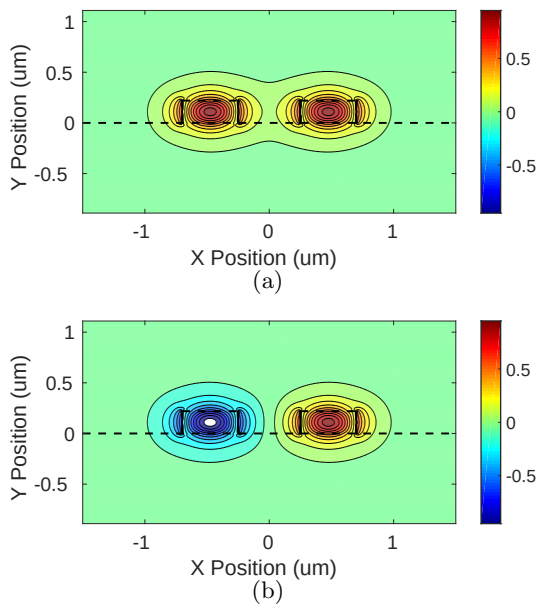

Figure 4.2: Field profiles of (a) the TE_0 mode, and (b) the TE_1 mode for a conventional DC.

As the TE_0 and the TE_1 modes travel, the optical power appears to beat back and forth between the two waveguides. The cross-over length, L_π, is a function of the difference in propagation constants, β_1 and β_2 of the TE_0 and the TE_1 modes, respectively, and is the minimum length required for the maximum optical power transfer from one waveguide to the other:

$$L_\pi = \frac{\pi}{\beta_1 - \beta_2} = \frac{\lambda/2}{n_{\text{eff1}} - n_{\text{eff2}}} \tag{4.1}$$

where λ is the operating wavelength, n_{eff1} and n_{eff2} are the effective indices of the TE_0 and TE_1 modes, respectively. The simulated n_{eff1} and n_{eff2} values, as functions of λ for a DC with $w = 450$nm and $g = 220$nm, are shown in Fig 4.3(a). It can be seen that both the TE_0 mode and the TE_1 mode have

normal dispersions ($dn/d\lambda < 0$), and the slope of n_{eff2} is larger than that of n_{eff1}. The difference between n_{eff1} and n_{eff2}, δn, increases as λ increases. Such a wavelength dependent δn leads to a wavelength dependent L_π, as shown in Fig. 4.3(b), which limits the operating bandwidth of conventional DCs.

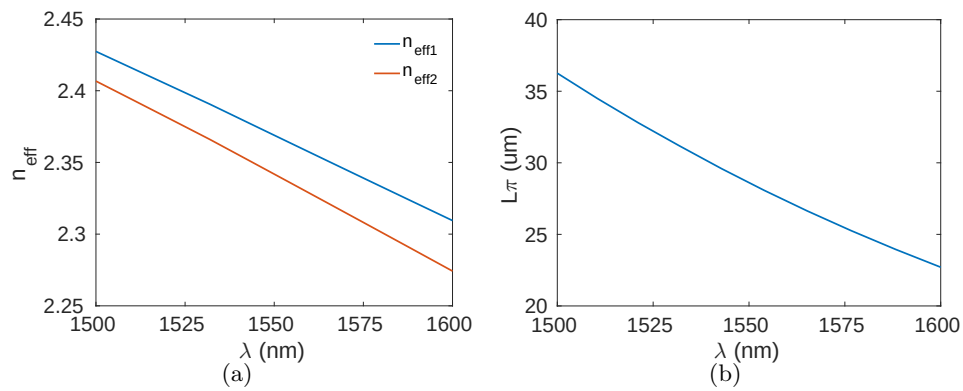

Figure 4.3: (a) n_{eff1} and n_{eff2} as functions of λ for a conventional DC, (b) L_π as a function of λ for a conventional DC. The simulated DC has $w = 450\,\text{nm}$, $g = 220\,\text{nm}$, based on an SOI wafer with a silicon layer of $220\,\text{nm}$.

4.2 Dispersion Engineering

SWGs can be used to engineer the slope of n_{eff1} so that it is matched to that of n_{eff2}; therefore, a δn that is less wavelength dependent in the wavelength range that we are interested in can be obtained. As shown in Fig. 4.4, when λ is approaching the Bragg wavelength, $\lambda_{\text{B}} = 2 \cdot n_{\text{eff}} \cdot \Lambda$, of an SWG, from the long wavelength side, the n_{eff} of the fundamental Floquet mode [7] increases dramatically. When the SWGs are applied to a conventional DC, the index perturbation of n_{eff2} is cancelled in the central region because the TE_1 mode has an antisymmetric field profile. On the other hand, n_{eff1}

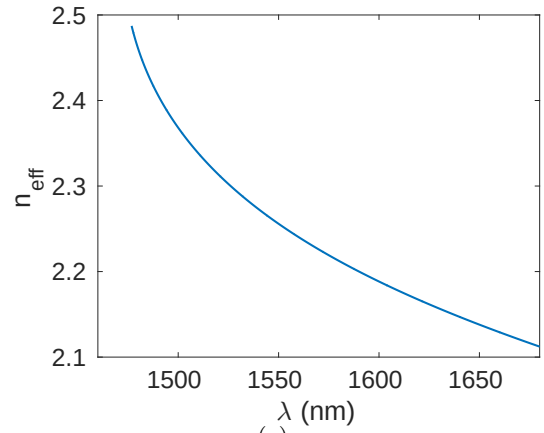

(a)

Figure 4.4: n_{eff} as a function of λ for an SWG with $\Lambda = 285\,\text{nm}$, $ff = 0.5$.

increases dramatically as λ approaches λ_{B}. Therefore, the slope of n_{eff1} can be increased to match with that of n_{eff2}. There are five parameters that need to be determined for SWG DCs: Λ, ff, g, t, and the number of grating, NG. In order to avoid the coupling in the S bend waveguides regions, we used $g = 500\,\text{nm}$ in our design. It has been found [30] that t should be greater than 400 nm to sufficiently suppress the optical power coupled to the higher order modes and we used $t = 500\,\text{nm}$ in our design. We used the "Bandstructure" model from the knowledge base provided by *Lumerical Solutions, Inc.* to analyze our designs. Compared to the commonly used eigenmode expansion (EME) method, in which the SWGs are estimated by the effective medium theory [64], our approach has the following advantages. Firstly, FDTD-based band structure calculations simulate the actual structure and take the material dispersion, the structure dispersion, and the Bragg effect into consideration. Our SWG DC can be simulated with using the EMT since the Bragg effect from the SWGs was omitted by the EMT method where SWGs are treated as uniform material with equivalent refractive indices. Secondly,

band structure calculations only require simulations of one unit cell of the structure, which significantly reduces simulation times as compared to full-structure FDTD simulations. A full-structure 3D FDTD simulation can take a few hours, while it only take a few minutes to simulate the structure using 3D FDTD band structure calculations, which makes device optimization possible. Our SWG DCs are designed for the TE_0 mode with λ of 1550 nm.

A schematic of the simulation structure for an SWG DC is shown in Fig. 4.5(a). Only one unit cell, one period of the SWG DC, was simulated and Bloch boundary conditions were used in the z direction, which is the propagation direction of the optical modes. The simulations were launched in the time domain and then transferred into the frequency domain using the Fourier transform. The band diagram of an SWG DC can be obtained by running a parameter sweep for various wave vectors, $kz = \frac{2\pi}{\Lambda}$. The band diagram of an SWG DC is shown in Fig. 4.5(b).

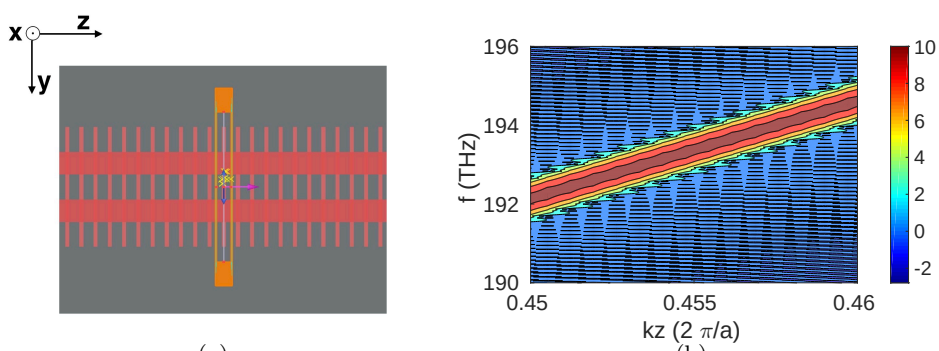

(a) (b)

Figure 4.5: (a) Schematic of the simulated structure for an SWG DC in *FDTD Solutions*, (b) simulated band diagram for an SWG DC with $\Lambda = 285$ nm and $ff = 0.28$.

The simulated transmission spectra from the cross ports as functions of λ for SWG DCs with $ff = 0.25$ and various Λ values, are shown Fig. 4.6(a),

where the troughs correspond to λ_B and the peak regions denote the wavelength regions where δn is over compensated. In order to achieve a broad operating bandwidth, in the wavelength range from 1500 nm to 1600 nm, we used $\Lambda = 285$ nm in our designs. The ff of the SWG DC has both a lower limit, which comes from the fabrication limitation, and an upper limit, which determines the optical power coupled into the higher order mode of the SWG [30]. Simulations shows that as the ff of the SWG DC increases, more power will coupled into the third order mode. In our case, $0.2 < ff < 0.3$. The simulated transmission spectra from the cross ports for SWG DCs with $\Lambda = 285$ nm, and various ff values are shown in Fig. 4.6(b). It can be seen that SWG DCs with larger ff values have stronger coupling, which results in smaller L_π. For a given Λ, ff determines n_{eff}, which in turn determines λ_B. By comparing the wavelength dependent δn, over the wavelength range from 1500 nm to 1600 nm, we can find the SWG DC with an optimized ff, with the least wavelength dependency. In our case, $ff = 0.28$.

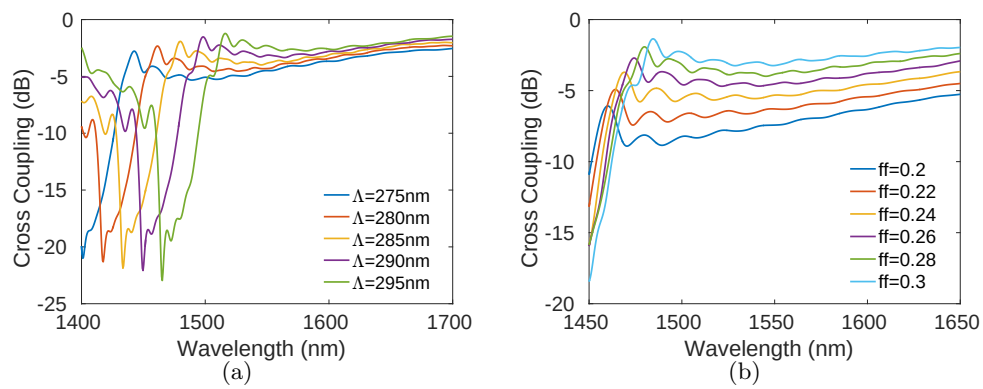

Figure 4.6: (a) Simulated transmission spectra from the cross ports of SWG DCs with $ff = 0.25$, $NG = 47$, and various Λ values, (b) simulated transmission spectra from the cross ports of SWG DCs with $\Lambda = 285$ nm, $NG = 47$, and various ff values.

From the band structure diagram, we can extract n_{eff1} and n_{eff2} values as functions of λ. Therefore, L_π can be calculated. The n_{eff1} and n_{eff2} values, as functions of λ for the SWG DC with $\Lambda = 285\,\text{nm}$ and $ff = 0.28$, are shown in Fig. 4.7(a) and the corresponding L_π, as a function of λ, is shown in Fig. 4.7(b). It can be seen that by using SWGs, the wavelength dependency of L_π has been reduced from $\pm 7\,\mu\text{m}$ to $\pm 1.5\,\mu\text{m}$. The λ_{B}, determined by Λ and n_{eff}, is about 1425 nm. It should be noted that the optimized ff is for the given Λ used in our design, other combinations of Λ and ff with the same λ_{B} can provide SWG DCs with similar bandwidths. NG determines the coupling length, which in turn determines the power splitting ratio of the design.

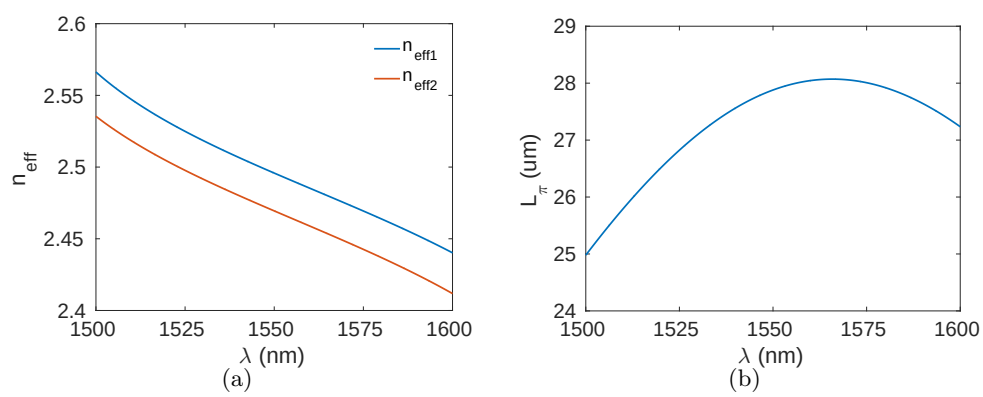

Figure 4.7: (a) n_{eff1} and n_{eff2} as functions of λ for an SWG DC with $\Lambda = 285\,\text{nm}$ and $ff = 0.28$, (b) calculated L_π as a function of λ based on the n_{neff1} and n_{eff2} shown in (a).

After we designed the SWG DC using band structure calculations, full-strucuture simulations were used to verify the design. The light was launched in the upper waveguide from the left and measured at the cross and through ports on the right. We define the normalized output power for the cross and through ports as $\eta_1 = 10 * log10(P_1/(P_1 + P_2))$ and $\eta_2 = 10 * log10(P_2/(P_1 + P_2))$, where P_1 and P_2 are the output power measured from the cross and

the through ports, respectively. Figure 4.8(a) shows the full-structure FDTD simulation results for the SWG DC with a device length of 13.4 µm, which was designed to have a power splitting ratio of 50/50. The designed SWG DC covers a bandwidth of 100 nm, from 1500 nm to 1600 nm, with an imbalance of ±0.55 dB. The simulated insertion loss, IL, as a function of λ for the SWG DC with the designed power splitting ratio of 50/50 is shown in Fig. 4.8(b). The IL as a function of ff for SWG DCs with $\Lambda = 285$ nm is shown in Fig. 4.9. It should be noted that there is a trade-off between the bandwidth and IL and here we chose bandwidth over IL. In addition, by using a large ff for our design, we also benefit from a small L_π, which means that the design is space efficient.

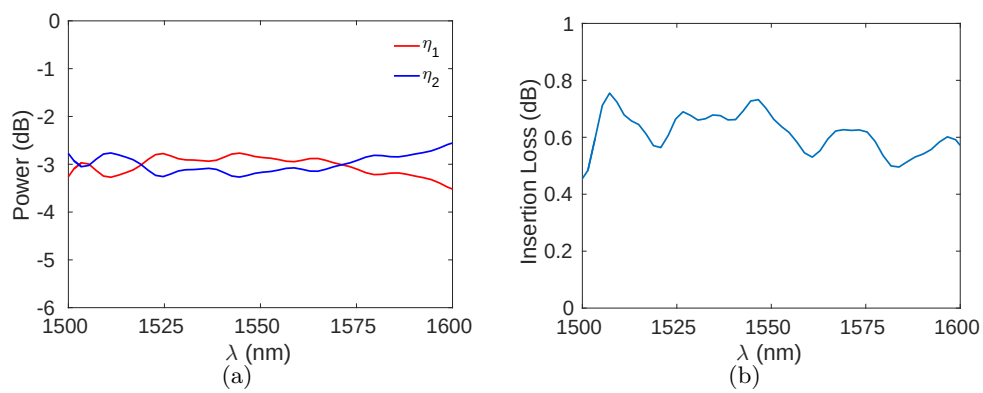

Figure 4.8: (a) Simulated spectra for an SWG DC with a designed power splitting ratio of 50/50 (η_1 and η_2 are the normalized output power for the cross and through ports, respectively), (b) simulated IL as a function of λ for the SWG DC with a designed power splitting ratio of 50/50.

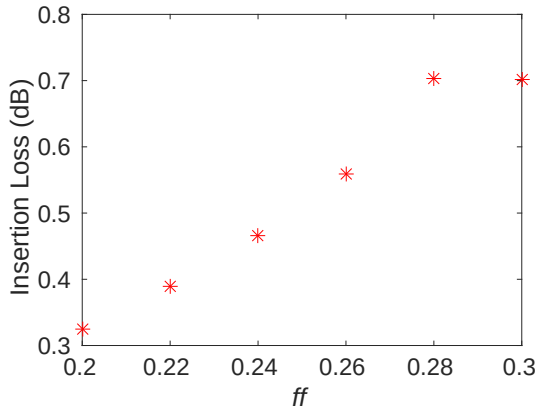

Figure 4.9: Simulated ILs as a function of ff for SWG DCs with $\Lambda = 285\,\text{nm}$.

4.3 Measurement Results

A waveguide-based Mach-Zehnder interferometer (MZI) was used to measure the wavelength dependent power coupling coefficient, K, of the designed SWG DCs. The mask layout of the test structure is shown in Fig. 4.10. Broadband SWG grating couplers [83] were used to couple the light into and out of the test structures. Identical SWG DCs were used as the power splitter and the combiner in the MZI and were connected by two waveguides with a δL of $250\,\mu\text{m}$. When both the splitter and the combiner have a power splitting ratio of 50/50, complete destructive interference occurs when the optical waves from the two arms of the MZI are out of phase. In the case in which the splitting or combining ratios are not 50/50, K can be extracted from adjacent maxima and minima of the spectrum [10], assuming that the SWG DCs are lossless.

For a real field coupling coefficient, k, for both the splitter and the combiner, and lossless waveguide, the transfer matrix of the test structure

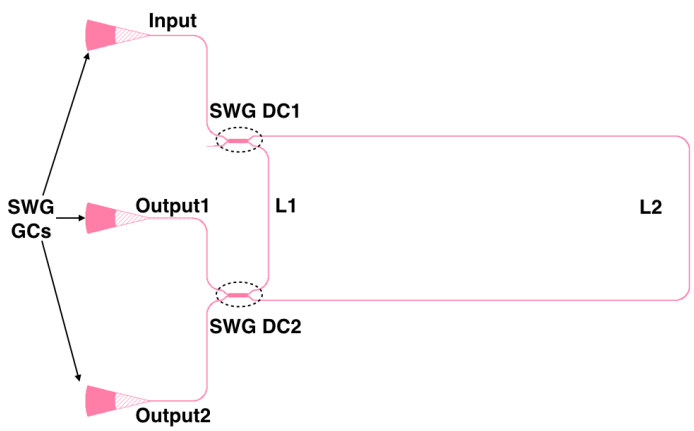

Figure 4.10: Mask layout of the test structure for SWG DCs.

shown in Fig. 4.10 is [96]:

$$\begin{bmatrix} E_{out1} \\ E_{out2} \end{bmatrix} = \begin{bmatrix} \sqrt{1-k^2} & jk \\ jk & \sqrt{1-k^2} \end{bmatrix} \begin{bmatrix} e^{-j\phi_1} & 0 \\ 0 & e^{-j\phi_2} \end{bmatrix} \begin{bmatrix} \sqrt{1-k^2} & jk \\ jk & \sqrt{1-k^2} \end{bmatrix} \begin{bmatrix} E_{in} \\ 0 \end{bmatrix}$$

where $\phi_1 = \beta L_1$, $\phi_2 = \beta L_2$, L_1 and L_2 are the lengths of the waveguides comprising the two arms of the MZI. E_{out1} and E_{out2} are the output electric fields from the two output ports of the MZI, which can be calculated from the above matrix to be:

$$E_{out1} = [(1-k^2) \cdot e^{-j\phi_1} + (jk)^2 \cdot e^{-j\phi_2}] \cdot E_{in} \tag{4.2}$$

and

$$E_{out2} = [jk\sqrt{1-k^2} \cdot e^{-j\phi_1} + jk\sqrt{1-k^2} \cdot e^{-j\phi_2}] \cdot E_{in} \tag{4.3}$$

From the electric fields, we can obtain the ERs of the normalized power

intensity for the two output ports as:

$$ER_1 = 10log_{10}(\frac{1}{1-4k^2(1-k^2)}) \tag{4.4}$$

$$ER_2 = 10log_{10}(\frac{4k^2(1-k^2)}{0}) = \infty \tag{4.5}$$

From Eq. 5 we can see that ER_2 is independent of the splitting ratio, and K can only be extracted from ER_1 and is given by:

$$K = k^2 = \frac{1}{2} \pm \frac{1}{2}\sqrt{\frac{1}{10^{\frac{ER_1}{10}}}} \tag{4.6}$$

SWG DC test structures, with various power splitting ratios, were fabricated on an SOI wafer with a 220 nm silicon layer on a 3 µm silicon dioxide. A JEOL JBX-6300FS system, operating at 100 keV energy, and with an 8nA beam current and a 500 µm exposure field was used to perform electron beam lithography [11]. The samples were on 25 mm squares diced from 150 mm wafers. The machine grid used for shape placement was 1 nm, while the beam stepping grid, the spacing between dwell points during the shape writing, was 6 nm. To characterize the devices, a custom-built automated test setup [19] was used. An Agilent 81600B tunable laser, with a PM fiber, was used as the input source, and Agilent 81635A optical power sensors, also with PM fibers, were used as the output detectors. A wavelength sweep from 1500 nm to 1600 nm in 10 pm steps was performed. SEM images of a fabricated SWG DC are shown in Fig. 4.11.

Due to the fact that the actual thickness of the silicon layer for the SOI wafer used in our fabrication was 206 nm, the optical modes were less confined within the waveguides. Thus, the coupling between the two waveg-

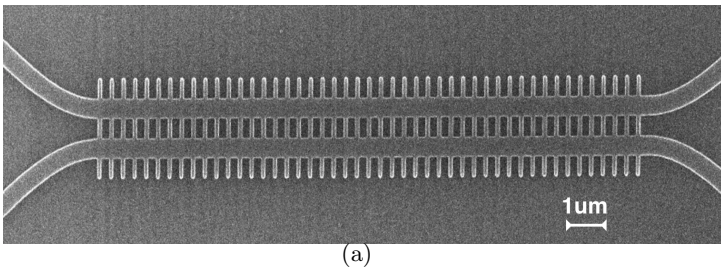

(a)

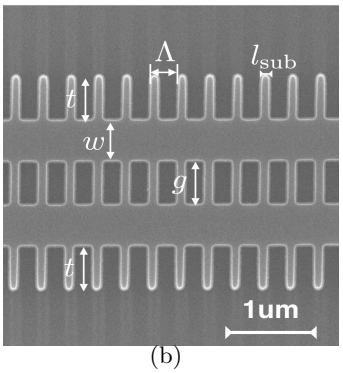

(b)

Figure 4.11: SEM images of (a) a fabricated SWG DC, (b) a zoom-in of the central portion of the fabricated SWG DC with the design parameters labelled.

uides of the fabricated SWG DCs was stronger than the design values. Figure 4.12(a) shows the measured spectra for a fabricated test structure with SWG DCs which had power splitting ratios close to 50/50. The measured SWG DCs had $g = 540\,\text{nm}$, $\Lambda = 285\,\text{nm}$, $ff = 0.28$, and $NG = 47$. The g of the fabricated SWG DCs with power splitting ratio close to 50/50 was 40 nm larger than the designed value, which compensated for the increased coupling resulting from the reduced thickness of the silicon layer. Output 1 and Output 2 denote the two output ports of the MZI as shown in Fig. 4.10. Figure 4.12(b) shows the normalized powers from the two ports of a fabricated SWG DC, which were calculated using Eq.(6) and the maxima and minima shown in Fig. 4.12(a). The ILs from the input and output grat-

ing couplers have been calibrated out. The measured SWG DC covered a bandwidth of 100 nm with an imbalance of ±0.7 dB, which agrees with the simulation results shown in Fig. 4.8. The power splitting ratios of an SWG DC can be controlled by either changing NG or ff. However, as we mentioned earlier, increasing ff may results in power coupling into the higher order mode of the SWG DC, which is unwanted. Therefore, we used NG to control K. Test structures for SWG DCs with power spitting ratios of 40/60, 30/70, and 20/80 have also been fabricated and measured, with their measurement results shown in Figs. 4.13(a)-(c), respectively.

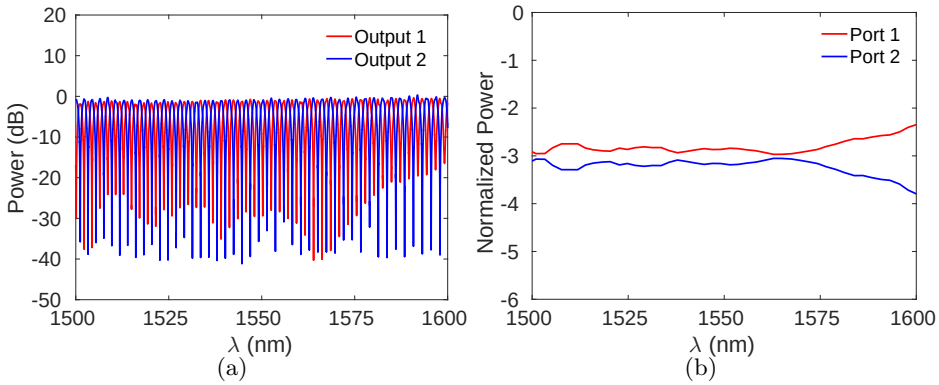

Figure 4.12: (a) Measured spectra for a test structure with SWG DCs which had power splitting ratios close to 50/50, and (b) normalized optical powers for a fabricated SWG DC using the measurement data shown in (a).

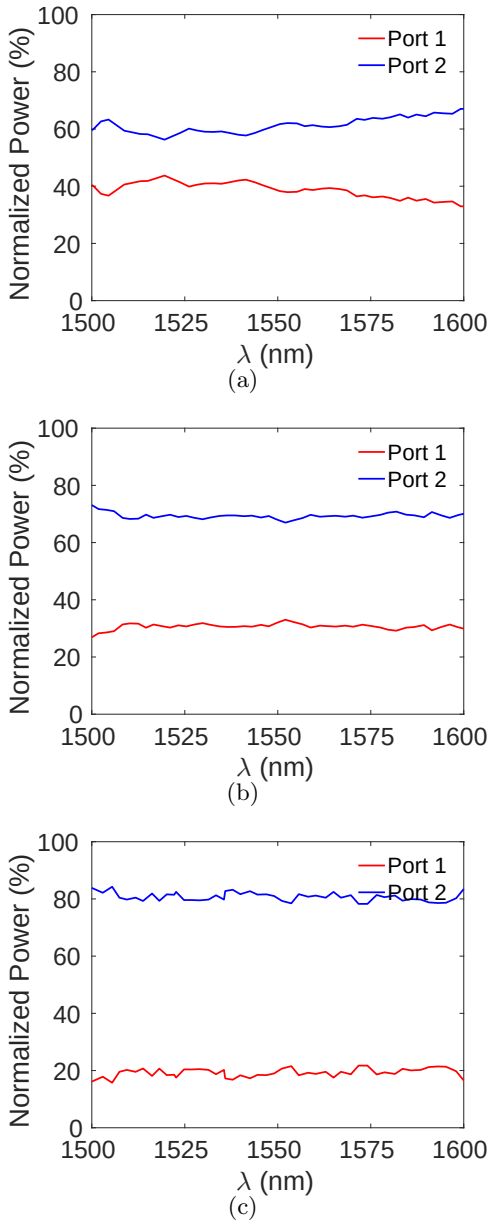

Figure 4.13: Normalized optical powers for fabricated SWG DCs with power splitting ratios of (a) 40/60, (b) 30/70, and (c) 20/80.

Chapter 5

Sub-wavelength Polarization Splitter Rotator

The polarization splitter-rotator (PSR) demonstrated in this chapter is a component that changes the polarization of the TM input mode to the TE mode, i.e., polarization rotated by 90 degrees, while maintaining the polarization of the TE input mode as the same. The TE and TM input modes inject into the PSR from the same input port and split into two output ports as two TE modes. PSRs have been used to construct polarization-insensitve PICs [3] in the strong confinement limit. Mode-evolution-based PSRs have been demonstrated [20, 23, 65, 81, 97], in which the TM_0 mode was first converted to the first order quasi-transverse electric, TE_1, mode, and then the TE_1 mode and the TE_0 modes were coupled into the TE_0 modes of two separate waveguides, using an asymmetric directional coupler [20], an asymmetric Y-branch [81, 97], a phase-shifted Y-branch and an MMI [23], or an adiabatic coupler [65]. The mode-evolution-based devices are less sensitive to fabrication imperfections and have broad operating bandwidths, but at the cost of large device footprints, typically on the order of a few hundred micrometers. Mode-coupling-based devices are more compact in size [45, 80], but the requirement of phase-matched modes makes such devices sensitive to both fabrication imperfections and wavelength. A mode-coupling-based

SWG PSR has been theoretically proposed [91], where SWGs were used to reduce the sensitivity to manufacturing variations of the waveguides widths. Although improved stability was quoted as the advantage of such device, the effects that induces the greatest variability, i.e., change in the fill factor of the SWG waveguide and the gap between the waveguides were ignored. In addition, the SWG taper and S bend waveguide used in [91] were much larger than the PSR itself, which significantly increases the overall size of the proposed device.

In this chapter, we extend the idea proposed in [91]. First, we explore the fabrication tolerance of our SWG PSR to various parameter variations, including the gap variations between the waveguides and the fill factor variations of the SWG waveguide; second, we design a high-efficiency and compact SWG taper that couples the optical modes from the SWG waveguide in our PSR into a strip waveguide without significant increase of the device footprint; third, we engineer the SWG PSR for broader operating bandwidth; fourth, the experimentally demonstrate the SWG PSR. In addition, an efficient modelling methodology based ons FDTD band structure calculations is presented in this chapter to design the coupling section of our SWG PSR, which dramatically reduced the computation time and design effort as compared to brute-force simulations of the full device using 3D FDTD simulations.

5.1 Design of SWG PSR

A schematic of our SWG PSR is shown in Fig. 5.1, which consists of three parts: a coupling section consisting of two parallel waveguides, one strip waveguide with a width, W_{A} and an SWG waveguide with a width, W_{B},

which separated by a gap, g; an SWG taper which couples the light from the SWG waveguide into the strip waveguide; and an S bend waveguide which decouples the two output waveguides. The SWG waveguide consists of SWGs with period, Λ, and fill factor, ff, which is defined as the ratio of l to Λ, as shown in Fig. 5.1. Again, our SWG PSR was designed for an SOI platform having silicon layers of 220 nm on a 3 µm BOX layer. The design of our SWG PSR was carried out by following a four-step process as described below.

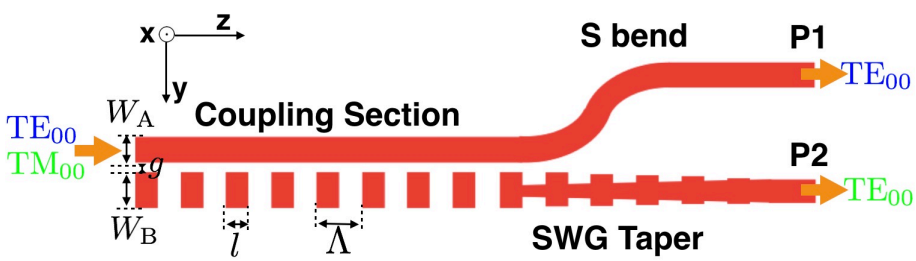

Figure 5.1: Schematic of the top view of an SWG PSR.

In the first step, we calculate the effective index of the TM_0 mode, $n_{\text{eff-TM}}$, for the strip waveguide as a function of W_A, which is denoted by the blue curve shown in Fig. 5.2. The dimensions of the strip waveguide we used is 450 nm x 220 nm, which has $n_{\text{eff-TM}} = 1.545$ at 1550 nm. In the second step, we treat the SWG waveguide as an equivalent wire waveguide with a refractive index of n_B and a width of W_B. The effective index of the TE_0 mode for the equivalent waveguide, $n_{\text{eff-TE}}$, is calculated as a function of W_B and n_B using *MODE Solutions* (an eigenmode solver from *Lumerical Solutions, Inc.*). An SWG waveguide is then found that has the same n_{eff} (i.e., $n_{\text{eff-TE}} = n_{\text{eff-TM}}$) and slope of n_{eff} (i.e., $\delta n_{\text{neff-TE}}/\delta W_B = \delta n_{\text{neff-TM}}/\delta W_A$) at 1550 nm as the TM_0 mode of the strip waveguide that we calculated in the first step. This SWG waveguide has an $n_B = 2.43$ and a $W_B = 670$ nm. The

simulated $n_{\text{eff-TE}}$ as a function of W_{B} for this SWG waveguide is denoted by the red curve in Fig. 5.2. Due to the fact that the n_{eff} for the strip and the SWG waveguides have the same slopes, the phase-match condition will be preserved if the waveguide widths are changed by the same amounts during fabrication. Here, in the first two steps, we used the phase-match condition of the two local normal modes in the strip and the SWG waveguide to obtain preliminary design parameters for the SWG waveguide given the dimensions of the strip waveguide. The design will be further optimized using supermodes theory, which is presented below.

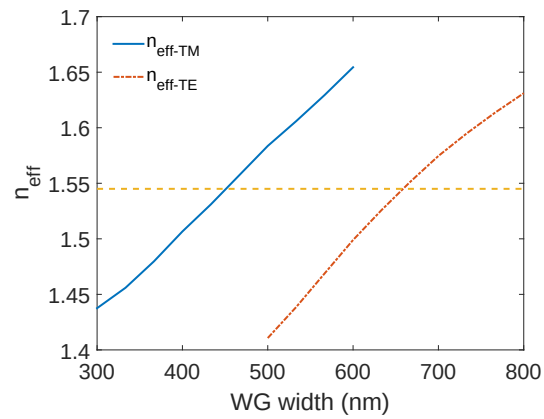

Figure 5.2: $n_{\text{eff-TM}}$ as a function of W_{A} for a strip waveguide and $n_{\text{eff-TE}}$ as a function of W_{B} for an SWG waveguide.

In the third step, we determine the Λ and the ff of the SWG waveguide based on the n_{B} we obtained from the previous two steps. FDTD band structure calculations are used to obtain the band diagram of the SWG waveguide, from which we extract $n_{\text{eff-TE}}$ as a function of λ for the SWG waveguide. For these calculations, we use *FDTD Solutions*. We set $\Lambda = 300\,\text{nm}$ in our simulation and by varying ff, we obtained SWG waveguides equivalent to wire waveguides with various values of n_{B}. In our case, $ff = 0.5$ for $n_{\text{B}} = 2.43$, calculated using three dimensional FDTD simulations.

The field distributions of the first three supermodes for the two waveguide systems comprising our SWG PSR are shown in Fig. 5.3, where the red dash lines denote the edges of the waveguides and the top of the BOX layer. Due to the fact that the supermodes are hybrid modes, and have electric fields in both the X and Y directions, we refer to the first three supermdoes as E_0^{xy}, E_1^{xy}, and E_2^{xy}.

In the fourth step, we calculate the length of the coupling section for the PSR. When the TE_0 mode is launched into the two waveguide system, it couples to the highly asymmetric E_0^{xy} mode (shown in Figs. 5.3(a)-(b)), in which the power is primarily confined to the strip waveguide and which propagates to the output of the two waveguide system with minimum power in the SWG waveguide. When the TM_0 mode is launched into the two waveguide system, it couples into both the E_1^{xy} (shown in Figs. 5.3(c)-(d)) and the E_2^{xy} (shown in Figs. 5.3(e)-(f)) modes in nearly equal portions so that after propagating one beat length, or L_π, in the two waveguide system, the Y-polarized electric fields in the two modes destructively interfere on the strip waveguide side of the two waveguide system while the X-polarized electric fields constructively interfere on the SWG waveguide side of the two waveguide system. The effective indices of the E_1^{xy} and the E_2^{xy} modes, $\mathrm{n}_{\mathrm{eff},1}$ and $\mathrm{n}_{\mathrm{eff},2}$, as functions of λ are shown in Fig. 5.4. The length of the coupling section for our SWG PSR is equal to L_π of the E_1^{xy} and the E_2^{xy} modes, which is calculated using:

$$L_\pi = \frac{\lambda/2}{n_{\mathrm{eff},1} - n_{\mathrm{eff},2}} \tag{5.1}$$

A $g = 100\,\mathrm{nm}$ was used in our simulation to achieve a comparatively short L_π and a larger L_π will be required for a coupling section with a larger g. In our case, $n_{\mathrm{eff},1} = 1.5843$ and $n_{\mathrm{eff},2} = 1.5528$, which lead to a $L_\pi = 24.6\,\mu\mathrm{m}$.

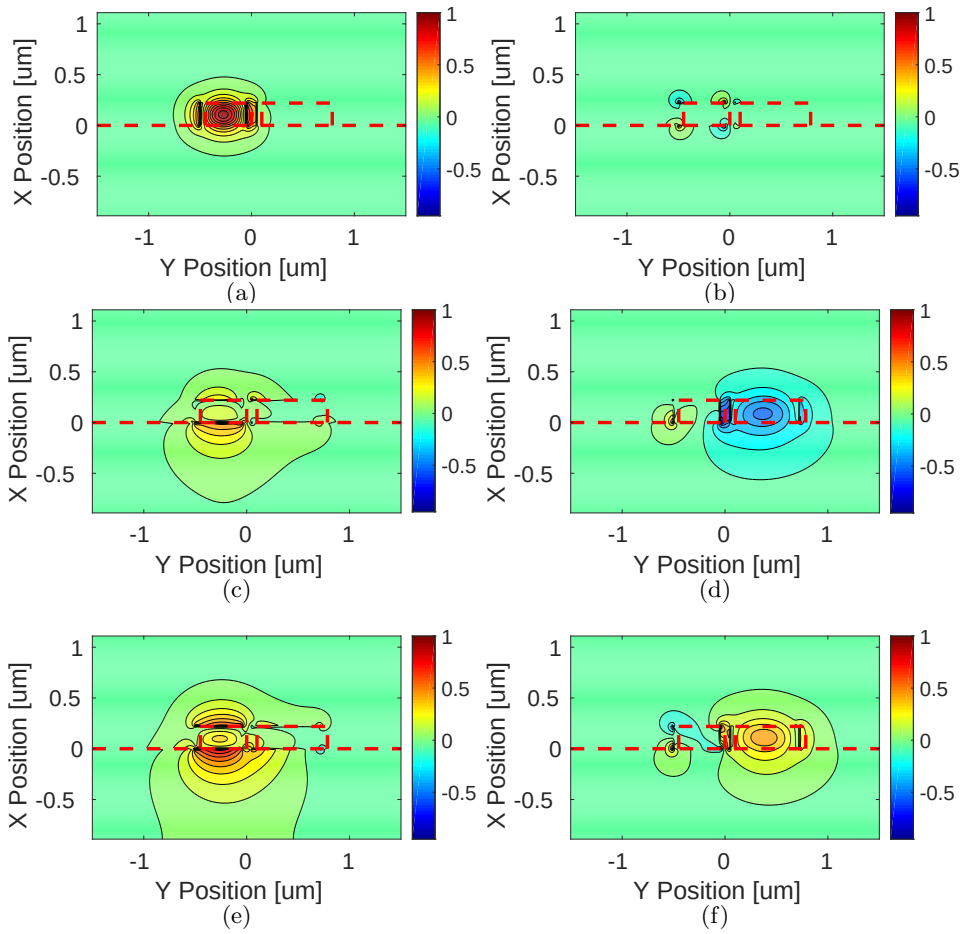

Figure 5.3: The X and Y field distributions for the first three supermodes. (a) Y component of the E_0^{xy} mode, (b) X component of the E_0^{xy} mode; (c) X component of the E_1^{xy} mode, (d) Y component of the E_1^{xy} mode; (e) X component of the E_2^{xy} mode, (f) Y component of the E_2^{xy} mode.

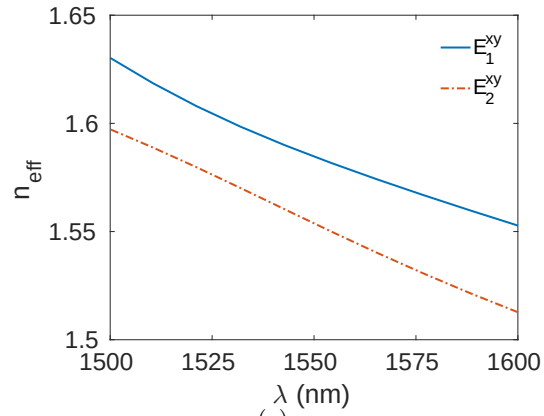

(a)

Figure 5.4: n_{eff} as a function of λ for the E_1^{xy} and the E_2^{xy} modes of the two waveguide system comprising the coupling section of the SWG PSR.

A high-efficiency, space-efficient SWG taper is required to couple the optical mode from the SWG waveguide into the strip waveguide. As shown in Fig. 5.5, our SWG taper consists of two parts: SWGs with period, Λ_{t}, and fill factor, $ff_{\mathrm{t}} = l_{\mathrm{t}}/\Lambda_{\mathrm{t}}$ and tapered bridge sections connecting the SWGs. In order to suppress the reflection at the interface of the SWG waveguide and the SWG taper, we use $\Lambda = \Lambda_{\mathrm{t}}$ and $ff = ff_{\mathrm{t}}$ in our design. The widths of the SWGs comprising the taper linearly decrease from $W_{\mathrm{B}} = 670\,\mathrm{nm}$ to $W_{\mathrm{A}} = 450\,\mathrm{nm}$. The bridge sections are used between the SWGs to reduce the effective index differences between adjacent sections, hence, to suppress the reflections between adjacent SWGs. The widths of the bridge sections are linearly increased from t_1 to W_{A}, where t_1 is the minimum feature size provided by the fabrication process. In our case, $t_1 = 60\,\mathrm{nm}$. We use an SWG taper with 30 periods, which has a simulated IL of less than 0.02 dB over the wavelength range from 1500 nm to 1600 nm using 3D FDTD simulation. The test structure of our design were fabricated

using electron beam lithography [11], which has an achievable minimum feature size of about 40 nm. In order to make the structure compatible with CMOS technology using optical lithography via MPW foundry services [43], which have minimum feature sizes of about 100 nm, t_1 can be increased at a cost of larger ILs. For $t_1 = 100$ nm and other parameters stay the same, the simulated IL of the taper increased from 0.02 dB to 0.04 dB over the wavelength range from 1500 nm to 1600 nm.

Figure 5.5: Schematic of the top view of an SWG taper.

Finally, the full structure of the designed SWG PSR is verified using 3D FDTD simulation, maintaining the SWG structure in the simulation and using SWG taper described above. The S bend waveguide used in the simulation has a height of 3 µm and a length of 5 µm. For the TE_0 mode input, we define the IL at $P1$ (shown in Fig. 5.1) as $IL_{TE\text{-}TE} = P1_{out,TE}/P_{in,TE}$ and the crosstalk (XT) at $P2$ (shown in Fig. 5.1) as $XT_{TE\text{-}TE} = P2_{out,TE}/P_{in,TE}$. For the TM_0 mode input, we define the polarization conversion efficiency (PCE) at $P2$ as $PCE_{TM\text{-}TE} = P2_{out,TE}/P_{in,\,TM}$ and the XT at P1 as $XT_{TM\text{-}TM} = P1_{out,TM}/P_{in,TM}$. The most important FOMs for a PSR are the $IL_{TE\text{-}TE}$ and the $PCE_{TM\text{-}TE}$, which are shown in Fig. 5.6(a). The simulated PSR has a negligible $IL_{TE\text{-}TE}$, a peak $PCE_{TM\text{-}TE}$ of -0.46 dB at 1550 nm with a 1dB bandwidth in excess of 80 nm. The PCE is limited by the mode distributions of the E_1^{xy} and the E_2^{xy} modes as shown in Fig.5.3(c)-(f). Due to the fact that the X and Y components of the E_1^{xy} and the E_2^{xy} modes are not fully overlapped, when the X components of E_1^{xy} and the E_2^{xy} modes are

out of phase, there is still a small portion of optical power resides on the strip waveguide side of the two waveguide system, which cause the loss of PCE. The PCE can be improved by optimizing the mode overlaps between the E_1^{xy} and the E_2^{xy} modes. The simulated $XT_{TM\text{-}TM}$ and $XT_{TE\text{-}TE}$ of the designed PSR are shown in Fig. 5.6(b).

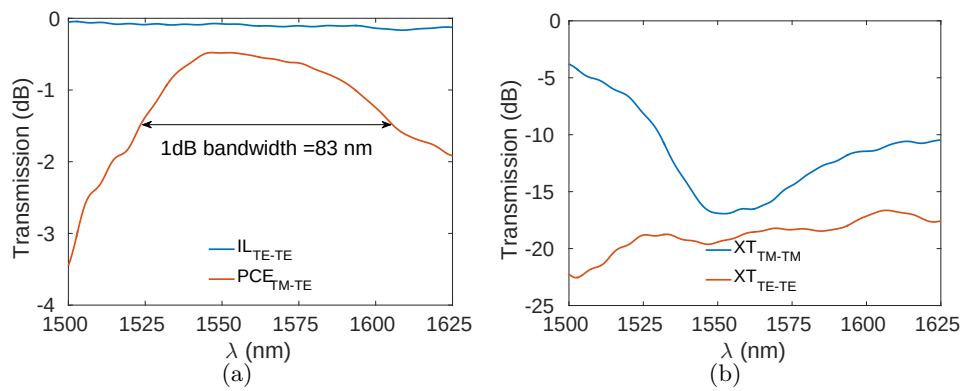

Figure 5.6: (a) Simulated $IL_{TE\text{-}TE}$ and $PCE_{TM\text{-}TE}$ as functions of λ, and (b) simulated $XT_{TE\text{-}TE}$ and $XT_{TM\text{-}TM}$ as functions of λ.

The fabrication tolerance of the designed SWG PSR, with the parameter variations shown in Table 5.1, has also been explored. The silicon layer thickness variation is denoted by δW_X and the variations in the other two dimensions are denoted by $\delta W_{Y\text{-}Z}$. δW_X is decided by the wafer uniformity used for fabrication. We used SOI wafers with silicon layers of 220 nm on a 3 µm BOX, provide by SOITEC, which has a guaranteed $3\sigma = \pm 10$ nm [92]. However, the central thickness of the wafer is not necessary to be 220 nm. Based on our experiences, the thickness of the silicon layer is 220±15 nm, and we used a variation range of ±20 nm to predict the worst possible situation in our simulations. When we explored the design tolerance to $\delta W_{Y\text{-}Z}$, we used $\pm\delta W_{Y\text{-}Z} = \pm\delta W_A = \pm\delta W_B = \mp\frac{1}{2}\delta g = \pm\delta l = \pm\delta l_t$ to mimic the

situation during fabrication. The simulated $\mathrm{PCE_{TM\text{-}TE}}$ as functions of δW_{X} and δW_{X} are shown in Fig. 5.7 as the green and the red curves. It has been discussed earlier that the designed SWG PSR has a high tolerance to δW_{A} and δW_{B}, which is achieved by designing the SWG waveguide to maintain the phase-match condition as the waveguide width varies. Therefore, the reduced $\mathrm{PCE_{TM\text{-}TE}}$ caused by $\delta W_{\mathrm{Y\text{-}Z}}$ is mainly the result of the variations in g and l (or ff), which have a strong impact on the coupling strength of the designed SWG PSR.

Table 5.1: Parameter Variations.

Parameters	δW_{X}	$\delta W_{\mathrm{Y\text{-}Z}}$
Variation Range	$\pm 20\,\mathrm{nm}$	$\pm 20\,\mathrm{nm}$

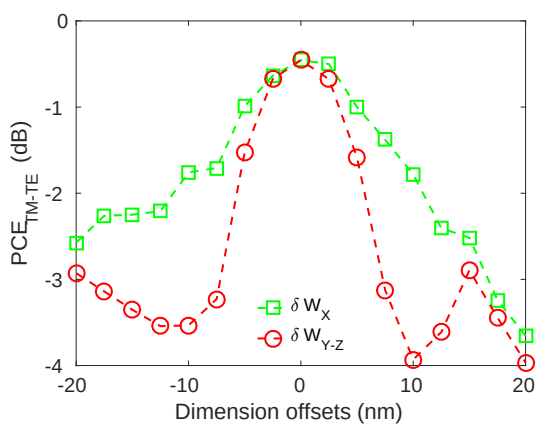

Figure 5.7: $\mathrm{PCE_{TM\text{-}TE}}$ as functions of δW_X and $\delta W_{\mathrm{Y\text{-}Z}}$.

5.2 Fabrication and Measurement

Test structures of the designed PSR, using broadband SWGCs as the input/output [83], were fabricated by electron beam lithography [11]. SEM images of a fabricated SWG PSR are shown in Fig. 5.8. Due to the fact that grating couplers are polarization sensitive, we designed grating couplers with

the same θ to couple the TE_0 and the TM_0 modes into the test structures, respectively. To characterize the devices, a custom-built test setup [19] was used. An Agilent 81600B tunable laser was used as the light source and Agilent 81635A optical power sensors were used as the output detectors. A wavelength sweep from 1500 nm to 1600 nm in 10 pm steps was performed.

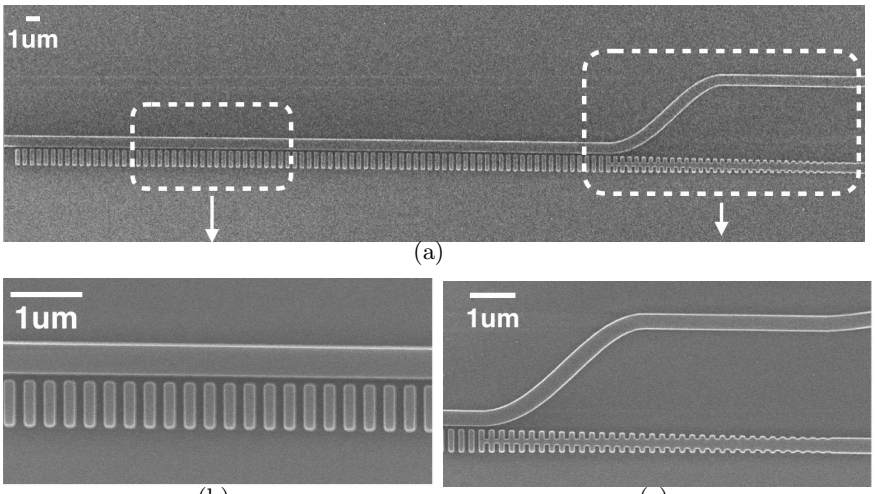

Figure 5.8: SEM images of a fabricated SWG PSR with zoomed images of the coupling section, the SWG taper, and the S bend waveguide.

The measured transmission spectra of a fabricated SWG PSR is shown in Fig. 5.9, where the ILs from the input and output grating couplers have been calibrated out. The measured $IL_{TE\text{-}TE}$ and $PCE_{TM\text{-}TE}$ are denoted by the blue and red curves shown in Fig. 5.9(a), respectively. The measured SWG PSR had an $IL_{TE\text{-}TE}$ close to 0dB over most of the wavelength range from 1500 nm to 1600 nm, and the ripples shown in the curve was caused by the non-uniformity of the grating couplers. The fabricated SWG PSR had a peak $PCE_{TM\text{-}TE}$ of -0.3 dB at 1538 nm and a 1-dB bandwidth over 50 nm. The measured XTs of the SWG PSR are shown in Fig. 5.9(b) by the red and blue curves, respectively. The $XT_{TE\text{-}TE}$ is below -15 dB over

the wavelength range from 1500 nm to 1600 nm, and the $XT_{TM\text{-}TM}$ is below -10 dB over the wavelength range from 1503 nm to 1588 nm.

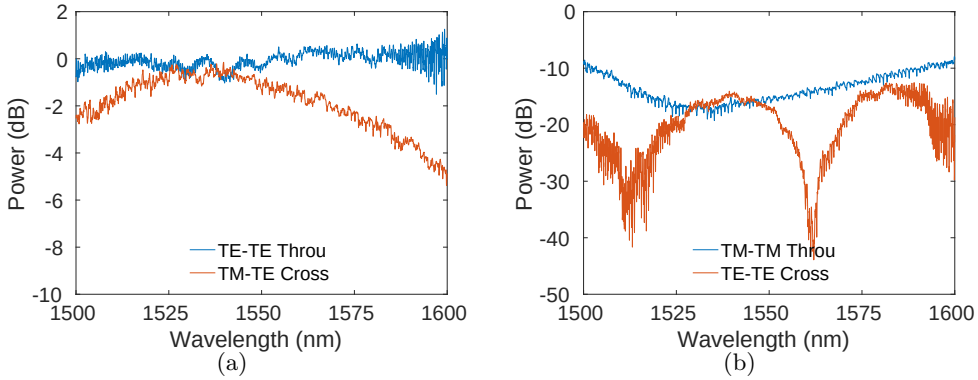

Figure 5.9: (a) Measured $IL_{TE\text{-}TE}$ and $PCE_{TM\text{-}TE}$ as functions of λ, and (b) measured $XT_{TE\text{-}TE}$ and $XT_{TM\text{-}TM}$ as functions of λ.

To summarize, in this chapter, we have experimentally demonstrated a compact SWG PSR for an SOI platform with a peak $PCE_{TM\text{-}TE}$ of -0.3 dB, a 1-dB bandwidth over 50 nm. The designed SWG PSR had a compact size of about 35 µm x 5 µm, which was achieved by using a space-efficient SWG taper with a length less than 10 µm. The fabrication tolerance of the designed SWG PSR to the waveguide width variations have been improved and the fabrication tolerance to the dimension variations and wafer thickness variations have been studied.

Chapter 6

Conclusion and Future Work

6.1 Conclusion

To conclude, we will summarize the contributions of the works shown in this dissertation from three aspects: the technical contributions, design methodology contributions, and the theoretical contributions.

6.1.1 Technical Contributions

- First demonstration of compact, high-efficiency SWGCs using one-dimensional SWGs for both the TE_0 mode and the TM_0 modes with suppressed back reflections. Our SWGCs for the TE and TM SWGCs show respective measured coupling efficiencies of -4.1 dB and -3.7 dB with 1-dB bandwidths of 30.6 nm (3-dB bandwidth of 52.3 nm) and 47.5 nm (3-dB bandwidth of 81.5 nm), respectively. The back reflections for the TE_0 and TM_0 modes have been significantly suppressed to -16.2 dB and -20.8 dB, respectively.

- Demonstration of apodized focusing SWGCs with improved coupling efficiencies for both the TE and TM modes. A measured measured coupling efficiency of -3.2 dB with a 1-dB bandwidth of 36 nm has been obtained for the TE SWGC and a measured coupling efficiency of -3.3 dB with a 1-dB bandwidth of 37 nm has been obtained for the

TM SWGC. Back reflections for the TE SWGC and TM SWGC have been suppressed to −24 dB and -21 dB, respectively.

- Demonstration of broadband sub-wavelength grating couplers with 1-dB bandwidths ranging from 50 nm to 90 nm. Our designed SWGCs have competitive coupling efficiency, as high as −3.8 dB for the TE mode, and state-of-the-art back reflections, as low as −23 dB. The comparisons of the SWGCs shown in this dissertation with the state-of-the-art SWGCs demonstrated by other research groups are listed in Table. 6.1.

- First experimental demonstration of broadband directional couplers using sub-wavelength gratings. The dispersion properties of the optical modes are engineered using sub-wavelength gratings, which allows broadband operation. Compact broadband direction couplers, with device lengths shorter than 14 µm, which cover a bandwidth of 100 nm, for power splitting ratios of 50/50, 40/60, 30/70, and 20/80, are designed and fabricated for the TE_0 mode with a central operating wavelength of 1550 nm.

- First experimental demonstration of polarization splitter-rotator (PSR) on a silicon-on-insulator platform based on an asymmetric directional coupler using sub-wavelength gratings. A measured peak TM-TE polarization conversion efficiency of −0.3 dB was achieved with TE-TE crosstalks below −15 dB and TM-TM crosstalks below −10 dB over C-band. The designed SWG PSR has a compact size of 35 µm x 5 µm.

Table 6.1: Comparison of SWGCs for the SOI platform. CE, coupling efficiency; BW, bandwidth.

Ref.	Year	CE (dB)	3-dB BW (nm)	Remarks
[15]	2009	-4.7	40	DUV fabrication
[46]	2010	-3.8	60	
[29]	2010	-4.2	60	TM pol.
[29]	2010	-3.7	55	TM pol.; apodized
[31]	2012	-5	55	TM pol.; DUV fabrication
[73]	2012	-2.4	60	optimized BOX
[94]	2012	-5.6	100	reduced index
[16]	2012	-3.5	80	reduced index
[17]	2012	-3	50	TM pol.; apodied; focusing
[95]	2013	-5.1	115	reduced index and SWG pitch
[22]	2013	-1.8	60	apodized; optimized BOX
[84]	2014	-3.7	52	focusing; TE pol.
[84]	2014	-4.1	82	focusing; TM pol.
[85]	2014	-3.2	59	focusing; apodized; TE pol.
[85]	2014	-3.3	72	focusing; apodized; TM pol.
[6]	2014	-2.16	64	apodized
[24]	2014	-0.58	71	apodized; mirror; 250nm Si
[83]	2014	-5.5	>120	focusing; TE pol.
[5]	2015	-0.69	60	apodized; mirror
[24]	2014	-0.43	76	mirror; 250nm Si, TE pol. (simu.)
[5]	2015	-0.67	NA	mirror; TE pol. (simu.)
[85]	2014	-0.34	85	focusing; mirror; TE pol. (simu.)
[85]	2014	-0.41	85	focusing; TM pol.; mirror(simu.)

6.1.2 Design Methodology Contributions

In the processes of my research on various projects, including the ones shown in this dissertation, the goal was not only getting one or several hero devices for publications, but also summarizing the design steps that I have been followed and refining them to solid design methodologies that can be shared and used by other researchers in this field. The major contributions of this dissertation from the methodology perspective include:

- Design methodology for high-efficiency sub-wavelength grating couplers (SWGCs) using one-dimensional sub-wavelength gratings as shown in Chapter 2. Compared to the commonly used simulation method in which the high and low index regions in an SWGC were treated as homogeneous materials using EMT, our method have several advantages. Firstly, our method simulates the cross-section of the actual sub-wavelength structures, which include both the material and structure dispersion from an SWGC for more accurate simulation results. Secondly, our design methodology was based on two-dimensional simulations, which is very efficient for design parameter optimization. In contrast, when using EMT method, SWGCs are first optimized with virtual refractive indices using 2D simulations. Then, EMT is used to calculate the dimensions of the SWG structures, i.e., either 2D SWGs or 1D SWGs, where time-consuming and computational intensive 3D simulations are required for 2D SWGs. In case where 1D SWGs are used, using EMT is redundant in the design process since the structure can be directly optimized using 2D simulations, as shown in this dissertation. The validity of the design methodology has been verified by experimental demonstration of high-efficiency uniform and apodized SWGCs for both the TE_0 and the TM_0 modes. Finally, it is easier and more straightforward to set the thresholds, minimum and maximum dimension values, for the SWGs using our method than using EMT. Because the optimized virtual refractive indices may require feature sizes that are smaller than the minimum feature sizes of the fabrication.

- Design methodology for broadband SWGCs. A four-step design pro-

cess has been demonstrated in Chapter 3 of this dissertation on how to design broadband SWGCs with design intent 1-dB bandwidths ranging from 50 nm to 90 nm. Again, the design methodology is based on the actual sub-wavelength structure, which provides more accurate simulation results and also less computationally intensive. The validity of the design methodology has been verified by successful experimental demonstration of both straight and focusing SWGCs with measured 1-dB bandwidths ranging from 50 nm to 90 nm.

- Design methodology for broadband SWG DCs using FDTD band structure calculations. Compared to the commonly used method, in which the SWGs are estimated by the effective medium theory (EMT), our approach has the following advantages. Firstly, FDTD-based band structure calculations simulate the actual structure and take the material dispersion, the structure dispersion, and the Bragg effect into consideration. The Bragg effect from the SWGs was used to engineer the dispersion properties of the optical modes within our SWG DCs, which was omitted by the EMT where SWGs are treated as uniform material with equivalent refractive indices. Secondly, band structure calculations only require simulations of one unit cell of the structure, which significantly reduces simulation times as compared to full-structure FDTD simulations, i.e., hours versus minutes, and make efficient device optimization possible. In addition, this FDTD band structure based simulation method has also been extended to design the polarization splitter-rotator (PSR) shown in Chapter 5 of this dissertation.

6.1.3 Theoretical Contributions

The major theoretical contribution of this dissertation is the study on the operating bandwidth of a grating coupler. When I first started working on the topic of broadband grating couplers, I found that the existing theoretical study was not straightforward to be used as practical guidelines from the design perspective. In various research papers, authors normally show the analytical equations for the operating bandwidth of a grating coupler and then optimizing their designs using brute-force numerical simulations that were not related to the analytical equations shown in their papers. We derived the operating bandwidth of a grating coupler based on the wavelength-dependent diffraction angle and related the bandwidth of a grating coupler to only three design parameters: the refractive index of the cladding material, the incident angle, and the group index of the grating coupler. Due to the fact that index of the cladding is a known constant for a specific fabrication process, the bandwidth of a grating coupler is only related to the incident angle and the group index of the grating coupler. And for a given indent angle, the bandwidth is only related to the group index of a grating coupler. The above conclusions made from our analytical model provide technical guidelines on designing broadband grating couplers in general and also provide the possibility to design grating couplers with design intent operating bandwidths.

6.2 Future Work

With the demonstrated works in this dissertation, suggested future work includes:

- SWGCs with coupling efficiencies below -0.5dB may be achieved by adding bottom mirrors. The major loss of the existing grating couplers, including the high-efficiency sub-wavelength grating couplers shown in this dissertation, is the penetration loss into the substrate. The penetration loss can be highly reduced, i.e., more than 90%, by adding a bottom mirror. The bottom mirror can obtained either by using SOI wafers with distributed Bragg reflector at the bottom of the wafer or by deposition of a metal layer at the interface of the buried oxide and silicon substrate.

- SWGCs with ultra-low back reflections can be obtained by replacing the taper regions of the SWGCs shown in Chapter 2 of this dissertation with sub-wavelength structures. Schematic of the cross-section of a sub-wavelength grating coupler with sub-wavelength structures comprising both the coupling region and the taper region is shown in Fig. 6.1. The comparatively large index contrast at the interface of the coupling region, i.e., consisting of sub-wavelength gratings, and the taper region, i.e., consisting of silicon slab, leads to a Fresnel reflection at the interface, which results in oscillation ripples in the transmission spectrum. By designing a taper region with SWGs which have a similar effective index as the coupling region, the Fresnel reflection can be highly suppressed. With the SWG taper, the optical mode can be coupled directly into an SWG waveguide. For bio-sensing application, where SWG waveguide and SWG ring resonators are used for enhanced sensitivity, using the proposed SWGCs can avoid extra couplers that are required to coupled light between the SWG waveguides and the strip waveguides. Therefore, the system can be more space

efficient and power efficient.

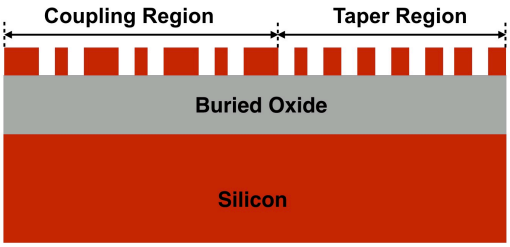

Figure 6.1: Schematic of the cross-section of an SWGC with sub-wavelength structures comprising both the coupling region and the taper region.

- A CMOS-compatible broadband sub-wavelength grating directional coupler can be made by modifying the period and fill factor of the design demonstrated in Chapter 4. The minimum feature size of the broadband sub-wavelength grating directional coupler is about 80 nm, which is not compatible with the 193 nm optical lithography provided by the MPW foundries using CMOS fabrication process. The minimum feature size of the device can be increased by using a smaller grating period with a larger fill factor for the sub-wavelength gratings used in the design, thus, the modified design can be fabricated through MPW foundries using CMOS-compatible fabrication process.

- A more compact polarization splitter-rotator (PSR) can be made by replacing the strip waveguide in the PSR demonstrated in Chapter 5 with a sub-wavelength grating waveguides. By using sub-wavelength grating waveguides, the effective index of the waveguide can be reduced, therefore, the optical modes are less confined within the waveguide, which will lead to stronger coupling between the two waveguides. Such a design also have better fabrication tolerance to the fill factor changes as compared to the design demonstrated in Chapter 5.

- A sub-wavelength grating PSR with suppressed crosstalk can be made by further optimizing the mode distributions of the supermodes, i.e., E_1^{xy} and E_2^{xy}, to equalize the power in the strip waveguide side of the two waveguide system demonstrated in Chapter 5. By optimizing the geometry of the two waveguide system, the optical power can be completely transferred from the strip waveguide side to the sub-wavelength grating waveguide side when the two modes are destructively interfered on the strip waveguide side, therefore, the crosstalk can be suppressed.

Bibliography

[1] Technology Agency for Science and Research (A*STAR) Institute of Microelectronics (IME) Silicon Photonics. https://www.a-star.edu.sg/ime/.(2016-06-01)

[2] Ryan Aguinaldo, Alex Forencich, Christopher DeRose, Anthony Lentine, Douglas C Trotter, Yeshaiahu Fainman, George Porter, George Papen, and Shayan Mookherjea. Wideband silicon-photonic thermo-optic switch in a wavelength-division multiplexed ring network. *Optics Express*, 22(7):8205–8218, 2014.

[3] Tymon Barwicz, Michael R Watts, Miloš A Popović, Peter T Rakich, Luciano Socci, Franz X Kärtner, Erich P Ippen, and Henry I Smith. Polarization-transparent microphotonic devices in the strong confinement limit. *Nature Photonics*, 1(1):57–60, 2007.

[4] Daniel Benedikovic, Carlos Alonso-Ramos, Pavel Cheben, Jens H Schmid, Shurui Wang, Dan-Xia Xu, Jean Lapointe, Siegfried Janz, Robert Halir, Alejandro Ortega-Moñux, et al. High-directionality fiber-chip grating coupler with interleaved trenches and subwavelength index-matching structure. *Optics Letters*, 40(18):4190–4193, 2015.

[5] Daniel Benedikovic, Pavel Cheben, Jens H Schmid, Dan-Xia Xu, Boris Lamontagne, Shurui Wang, Jean Lapointe, Robert Halir, Alejandro

Ortega-Moñux, Siegfried Janz, et al. Subwavelength index engineered surface grating coupler with sub-decibel efficiency for 220-nm silicon-on-insulator waveguides. *Optics Express*, 23(17):22628–22635, 2015.

[6] Daniel Benedikovic, Pavel Cheben, Jens H Schmid, Dan-Xia Xu, Jean Lapointe, Shurui Wang, Robert Halir, Alejandro Ortega-Moñux, Siegfried Janz, and Milan Dado. High-efficiency single etch step apodized surface grating coupler using subwavelength structure. *Laser & Photonics Reviews*, 8(6):L93–L97, 2014.

[7] JA Besley, NN Akhmediev, and PD Miller. Modes of periodic waveguides. *Optics Letters*, 22(15):1162–1164, 1997.

[8] Przemek J Bock, Pavel Cheben, Jens H Schmid, Jean Lapointe, André Delâge, Siegfried Janz, Geof C Aers, Dan-Xia Xu, Adam Densmore, and Trevor J Hall. Subwavelength grating periodic structures in silicon-on-insulator: a new type of microphotonic waveguide. *Optics Express*, 18(19):20251–20262, 2010.

[9] Przemek J Bock, Pavel Cheben, Jens H Schmid, Jean Lapointe, André Delâge, Dan-Xia Xu, Siegfried Janz, Adam Densmore, and Trevor J Hall. Subwavelength grating crossings for silicon wire waveguides. *Optics Express*, 18(15):16146–16155, 2010.

[10] Wim Bogaerts, Peter De Heyn, Thomas Van Vaerenbergh, Katrien De Vos, Shankar Kumar Selvaraja, Tom Claes, Pieter Dumon, Peter Bienstman, Dries Van Thourhout, and Roel Baets. Silicon microring resonators. *Laser & Photonics Reviews*, 6(1):47–73, 2012.

[11] Richard J Bojko, Jing Li, Li He, Tom Baehr-Jones, Michael Hochberg,

and Yukinori Aida. Electron beam lithography writing strategies for low loss, high confinement silicon optical waveguides. *Journal of Vacuum Science & Technology B*, 29(6):06F309, 2011.

[12] Charles Brackett et al. Dense wavelength division multiplexing networks: Principles and applications. *Selected Areas in Communications, IEEE Journal on*, 8(6):948–964, 1990.

[13] Pavel Cheben, Przemek J Bock, Jens H Schmid, Jean Lapointe, Siegfried Janz, Dan-Xia Xu, Adam Densmore, André Delâge, Boris Lamontagne, and Trevor J Hall. Refractive index engineering with subwavelength gratings for efficient microphotonic couplers and planar waveguide multiplexers. *Optics letters*, 35(15):2526–2528, 2010.

[14] Xia Chen and Hon K Tsang. Polarization-independent grating couplers for silicon-on-insulator nanophotonic waveguides. *Optics Letters*, 36(6):796–798, 2011.

[15] Xia Chen and Hon Ki Tsang. Nanoholes grating couplers for coupling between silicon-on-insulator waveguides and optical fibers. *Photonics Journal, IEEE*, 1(3):184–190, 2009.

[16] Xia Chen, Ke Xu, Zhenzhou Cheng, Christy KY Fung, and Hon K Tsang. Wideband subwavelength gratings for coupling between silicon-on-insulator waveguides and optical fibers. *Optics Letters*, 37(17):3483–3485, 2012.

[17] Zhenzhou Cheng, Xia Chen, Chi Yan Wong, Ke Xu, and Hon Ki Tsang. Apodized focusing subwavelength grating cou-

plers for suspended membrane waveguides. *Applied Physics Letters*, 101(10):101104, 2012.

[18] Lukas Chrostowski, Jonas Flueckiger, Charlie Lin, Michael Hochberg, James Pond, Jackson Klein, John Ferguson, and Chris Cone. Design methodologies for silicon photonic integrated circuits. In *SPIE OPTO*, pages 89890G–89890G. International Society for Optics and Photonics, 2014.

[19] Lukas Chrostowski and Michael Hochberg. *Silicon Photonics Design: From Devices to Systems*. Cambridge University Press, 2015.

[20] Daoxin Dai and John E Bowers. Novel concept for ultracompact polarization splitter-rotator based on silicon nanowires. *Optics Express*, 19(11):10940–10949, 2011.

[21] Katrien De Vos. *Label-Free Silicon Photonics Biosensor Platform with-Microring Resonators.* PhD thesis, Ghent University, 2010.

[22] Yunhong Ding, Haiyan Ou, and Christophe Peucheret. Ultrahigh-efficiency apodized grating coupler using fully etched photonic crystals. *Optics Letters*, 38(15):2732–2734, 2013.

[23] Yunhong Ding, Haiyan Ou, and Christophe Peucheret. Wideband polarization splitter and rotator with large fabrication tolerance and simple fabrication process. *Optics Letters*, 38(8):1227–1229, 2013.

[24] Yunhong Ding, Christophe Peucheret, Haiyan Ou, and Kresten Yvind. Fully etched apodized grating coupler on the SOI platform with -0.58 dB coupling efficiency. *Optics Letters*, 39(18):5348–5350, 2014.

[25] Valentina Donzella, Ahmed Sherwali, Jonas Flueckiger, Sahba Talebi Fard, Samantha M Grist, and Lukas Chrostowski. Sub-wavelength grating components for integrated optics applications on SOI chips. *Optics Express*, 22(17):21037–21050, 2014.

[26] Valentina Donzella, Ahmed Sherwali, Jonas Flueckiger, Samantha M Grist, Sahba Talebi Fard, and Lukas Chrostowski. Design and fabrication of SOI micro-ring resonators based on sub-wavelength grating waveguides. *Optics Express*, 23(4):4791–4803, 2015.

[27] Jonas Flueckiger, Shon Schmidt, Valentina Donzella, Ahmed Sherwali, Daniel M Ratner, Lukas Chrostowski, and Karen C Cheung. Sub-wavelength grating for enhanced ring resonator biosensor. *Optics Express*, 24(14):15672–15686, 2016.

[28] Charles W Haggans, Raymond K Kostuk, and Lifeng Li. Effective-medium theory of zeroth-order lamellar gratings in conical mountings. *JOSA A*, 10(10):2217–2225, 1993.

[29] R Halir, P Cheben, JH Schmid, R Ma, D Bedard, S Janz, D-X Xu, A Densmore, J Lapointe, and I Molina-Fernández. Continuously apodized fiber-to-chip surface grating coupler with refractive index engineered subwavelength structure. *Optics Letters*, 35(19):3243–3245, 2010.

[30] R Halir, A Maese-Novo, A Ortega-Moñux, I Molina-Fernández, JG Wangüemert-Pérez, P Cheben, D-X Xu, JH Schmid, and S Janz. Colorless directional coupler with dispersion engineered subwavelength structure. *Optics Express*, 20(12):13470–13477, 2012.

[31] R Halir, L Zavargo-Peche, D-X Xu, P Cheben, R Ma, JH Schmid, S Janz, A Densmore, A Ortega-Moñux, Í Molina-Fernández, et al. Single etch grating couplers for mass fabrication with duv lithography. *Optical and Quantum Electronics*, 44(12-13):521–526, 2012.

[32] Robert Halir, Przemek J Bock, Pavel Cheben, Alejandro Ortega-Moñux, Carlos Alonso-Ramos, Jens H Schmid, Jean Lapointe, Dan-Xia Xu, J Gonzalo Wangüemert-Pérez, Íñigo Molina-Fernández, et al. Waveguide sub-wavelength structures: a review of principles and applications. *Laser & Photonics Reviews*, 9(1):25–49, 2015.

[33] Robert Halir, Pavel Cheben, Siegfried Janz, Dan-Xia Xu, Íñigo Molina-Fernández, and Juan G Wangüemert-Pérez. Waveguide grating coupler with subwavelength microstructures. *Optics Letters*, 34(9):1408–1410, 2009.

[34] http://genisys gmbh.com/. (2016-06-01)

[35] Marc Ibrahim, Jens H Schmid, Alireza Aleali, Pavel Cheben, Jean Lapointe, Siegfried Janz, Przemek J Bock, Adam Densmore, Boris Lamontagne, Rubin Ma, et al. Athermal silicon waveguides with bridged subwavelength gratings for te and tm polarizations. *Optics express*, 20(16):18356–18361, 2012.

[36] IHP. https://www.ihp-microelectronics.com. (2016-06-01)

[37] John D Joannopoulos, Steven G Johnson, Joshua N Winn, and Robert D Meade. *Photonic crystals: molding the flow of light*. Princeton University Press, 2011.

[38] Raman Kashyap. *Fiber Bragg gratings*. Academic Press, 1999.

[39] Amit Khanna, Youssef Drissi, Pieter Dumon, Roel Baets, Philippe Absil, J Pozo, DMR Lo Cascio, M Fournier, JM Fedeli, L Fulbert, et al. epixfab: the silicon photonics platform. In *SPIE Microtechnologies*, pages 87670H–87670H. International Society for Optics and Photonics, 2013.

[40] Philippe Lalanne and Jean-Paul Hugonin. High-order effective-medium theory of subwavelength gratings in classical mounting: application to volume holograms. *JOSA A*, 15(7):1843–1851, 1998.

[41] Philippe Lalanne and Dominique Lemercier-Lalanne. On the effective medium theory of subwavelength periodic structures. *Journal of Modern Optics*, 43(10):2063–2085, 1996.

[42] LETI. http://www-leti.cea.fr/en/how-to-collaborate/focus-on-technologies/integrated-silicon-photonics. (2016-06-01)

[43] Andy Eu-Jin Lim, Junfeng Song, Qing Fang, Chao Li, Xiaoguang Tu, Ning Duan, Kok Kiong Chen, Roger Poh-Cher Tern, and Tsung-Yang Liow. Review of silicon photonics foundry efforts. *Selected Topics in Quantum Electronics, IEEE Journal of*, 20(4):405–416, 2014.

[44] Brent E Little and Tom Murphy. Design rules for maximally flat wavelength-insensitive optical power dividers using mach-zehnder structures. *IEEE Photonics Technology Letters*, 9(12):1607–1609, 1997.

[45] Liu Liu, Yunhong Ding, Kresten Yvind, and Jørn M Hvam. Silicon-on-insulator polarization splitting and rotating device for polarization diversity circuits. *Optics Express*, 19(13):12646–12651, 2011.

[46] Liu Liu, Minhao Pu, Kresten Yvind, and Jørn M Hvam. High-efficiency, large-bandwidth silicon-on-insulator grating coupler based on a fully-etched photonic crystal structure. *Applied Physics Letters*, 96(5):051126, 2010.

[47] Zeqin Lu, Han Yun, Yun Wang, Zhitian Chen, Fan Zhang, Nicolas A. F. Jaeger, and Lukas Chrostowski. Broadband silicon photonic directional coupler using asymmetric-waveguide based phase control. *Optics Express*, 23(3):3795–3808, 2015.

[48] A Maese-Novo, R Halir, S Romero-García, D Pérez-Galacho, L Zavargo-Peche, A Ortega-Moñux, I Molina-Fernández, JG Wangüemert-Pérez, and P Cheben. Wavelength independent multimode interference coupler. *Optics Express*, 21(6):7033–7040, 2013.

[49] Robert Magnusson, Mehrdad Shokooh-Saremi, and Eric G Johnson. Guided-mode resonant wave plates. *Optics Letters*, 35(14):2472–2474, 2010.

[50] Attila Mekis, Sherif Abdalla, Peter M De Dobbelaere, Dennis Foltz, Steffen Gloeckner, Steven Hovey, Steven Jackson, Yi Liang, Michael Mack, Gianlorenzo Masini, et al. Scaling CMOS photonics transceivers beyond 100 Gb/s. In *SPIE OPTO*, pages 82650A–82650A. International Society for Optics and Photonics, 2012.

[51] Attila Mekis, Steffen Gloeckner, Gianlorenzo Masini, Adithyaram Narasimha, Thierry Pinguet, Subal Sahni, and Peter De Dobbelaere. A grating-coupler-enabled CMOS photonics platform. *Selected Topics in Quantum Electronics, IEEE Journal of*, 17(3):597–608, 2011.

[52] Jurgen Michel, Jifeng Liu, and Lionel C Kimerling. High-performance Ge-on-Si photodetectors. *Nature Photonics*, 4(8):527–534, 2010.

[53] James G Mutitu, Shouyuan Shi, Caihua Chen, Timothy Creazzo, Allen Barnett, Christiana Honsberg, and Dennis W Prather. Thin film silicon solar cell design based on photonic crystal and diffractive grating structures. *Optics Express*, 16(19):15238–15248, 2008.

[54] Neil Na, Harel Frish, I-Wei Hsieh, Oshrit Harel, Roshan George, Assia Barkai, and Haisheng Rong. Efficient broadband silicon-on-insulator grating coupler with low backreflection. *Optics Letters*, 36(11):2101–2103, 2011.

[55] J Niklas Caspers and Mo Mojahedi. Measurement of a compact colorless 3dB hybrid plasmonic directional coupler. *Optics Letters*, 39(11):3262–3265, 2014.

[56] Régis Orobtchouk, Abdelhalim Layadi, Hamid Gualous, Daniel Pascal, Alain Koster, and Suzanne Laval. High-efficiency light coupling in a submicrometric silicon-on-insulator waveguide. *Applied Optics*, 39(31):5773–5777, 2000.

[57] Konstantinos E Parsopoulos. *Particle swarm optimization and intelligence: advances and applications: advances and applications*. IGI Global, 2010.

[58] James Pond, Chris Coneb, Lukas Chrostowskic, Jackson Kleina, Jonas Flueckigerc, Amy Liua, Dylan McGuirea, and Xu Wanga. A complete design flow for silicon photonics.

[59] Kun Qin, Dingshan Gao, Changjing Bao, Zhe Zhao, Xu Zhou, Tingting Lu, and Lin Chen. High efficiency and broadband two-dimensional blazed grating coupler with fully etched triangular holes. *Journal of Lightwave Technology*, 30(14):2363–2366, 2012.

[60] Daniel H Raguin and G Michael Morris. Antireflection structured surfaces for the infrared spectral region. *Applied Optics*, 32(7):1154–1167, 1993.

[61] Graham T Reed, G Mashanovich, FY Gardes, and DJ Thomson. Silicon optical modulators. *Nature Photonics*, 4(8):518–526, 2010.

[62] Jacob Robinson and Yahya Rahmat-Samii. Particle swarm optimization in electromagnetics. *Antennas and Propagation, IEEE Transactions on*, 52(2):397–407, 2004.

[63] Günther Roelkens, Diedrik Vermeulen, Frederik Van Laere, S Selvaraja, S Scheerlinck, D Taillaert, W Bogaerts, P Dumon, D Van Thourhout, and R Baets. Bridging the gap between nanophotonic waveguide circuits and single mode optical fibers using diffractive grating structures. *Journal of nanoscience and nanotechnology*, 10(3):1551–1562, 2010.

[64] SM Rytov. Electromagnetic properties of a finely stratified medium. *SOVIET PHYSICS JETP-USSR*, 2(3):466–475, 1956.

[65] Wesley D Sacher, Tymon Barwicz, Benjamin JF Taylor, and Joyce KS Poon. Polarization rotator-splitters in standard active silicon photonics platforms. *Optics Express*, 22(4):3777–3786, 2014.

[66] JH Schmid, M Ibrahim, P Cheben, J Lapointe, S Janz, PJ Bock, A Densmore, B Lamontagne, R Ma, WN Ye, et al. Temperature-independent silicon subwavelength grating waveguides. *Optics Letters*, 36(11):2110–2112, 2011.

[67] Wei Shi, Han Yun, Charlie Lin, Mark Greenberg, Xu Wang, Yun Wang, Sahba Talebi Fard, Jonas Flueckiger, Nicolas A. F. Jaeger, and Lukas Chrostowski. Ultra-compact, flat-top demultiplexer using anti-reflection contra-directional couplers for CWDM networks on silicon. *Optics Express*, 21(6):6733–6738, 2013.

[68] Mehrdad Shokooh-Saremi and Robert Magnusson. Leaky-mode resonant reflectors with extreme bandwidths. *Optics Letters*, 35(8):1121–1123, 2010.

[69] Wojciech Śmigaj, Philippe Lalanne, Jianji Yang, Thomas Paul, C Rockstuhl, and F Lederer. Closed-form expression for the scattering coefficients at an interface between two periodic media. *Applied Physics Letters*, 98(11):111107, 2011.

[70] Lucas B Soldano and Erik Pennings. Optical multi-mode interference devices based on self-imaging: principles and applications. *Journal of Lightwave Technology*, 13(4):615–627, 1995.

[71] Kimmo Solehmainen, Markku Kapulainen, Mikko Harjanne, and Timo Aalto. Adiabatic and multimode interference couplers on silicon-on-insulator. *Photonics Technology Letters, IEEE*, 18(21):2287–2289, 2006.

[72] FDTD Solutions. https://www.lumerical.com/tcad-products/fdtd/. (2016-06-01)

[73] Harish Subbaraman, Xiaochuan Xu, John Covey, and Ray T Chen. Efficient light coupling into in-plane semiconductor nanomembrane photonic devices utilizing a sub-wavelength grating coupler. *Optics Express*, 20(18):20659–20665, 2012.

[74] Dirk Taillaert, Peter Bienstman, and Roel Baets. Compact efficient broadband grating coupler for silicon-on-insulator waveguides. *Optics Letters*, 29(23):2749–2751, 2004.

[75] R Takei, M Suzuki, E Omoda, S Manako, T Kamei, M Mori, and Y Sakakibara. Silicon knife-edge taper waveguide for ultralow-loss spot-size converter fabricated by photolithography. *Applied Physics Letters*, 102(10):101108, 2013.

[76] PD Trinh, S Yegnanarayanan, F Coppinger, and B Jalali. Silicon-on-insulator (SOI) phased-array wavelength multi/demultiplexer with extremely low-polarization sensitivity. *Photonics Technology Letters, IEEE*, 9(7):940–942, 1997.

[77] Frederik Van Laere, Tom Claes, Jonathan Schrauwen, Stijn Scheerlinck, Wim Bogaerts, Dirk Taillaert, Liam O'Faolain, Dries Van Thourhout, and Roel Baets. Compact focusing grating couplers for silicon-on-insulator integrated circuits. *Photonics Technology Letters, IEEE*, 19(23):1919–1921, 2007.

[78] Diedrik Vermeulen, Yannick De Koninck, Yanlu Li, Emmanuel Lambert, Wim Bogaerts, Roel Baets, and Günther Roelkens. Reflectionless

grating couplers for silicon-on-insulator photonic integrated circuits. *Optics Express*, 20(20):22278–22283, 2012.

[79] Diedrik Vermeulen, S Selvaraja, Pl Verheyen, G Lepage, W Bogaerts, P Absil, D Van Thourhout, and G Roelkens. High-efficiency fiber-to-chip grating couplers realized using an advanced CMOS-compatible silicon-on-insulator platform. *Optics Express*, 18(17):18278–18283, 2010.

[80] Diedrik Vermeulen, Peter Verheyen, Philippe Absil, Wim Bogaerts, Dries Van Thourhout, Günther Roelkens, et al. Silicon-on-insulator polarization rotator based on a symmetry breaking silicon overlay. *IEEE Photonics Technology Letters*, 24(6):482–484, 2012.

[81] Jing Wang, Ben Niu, Zhen Sheng, Aimin Wu, Wei Li, Xi Wang, Shichang Zou, Minghao Qi, and Fuwan Gan. Novel ultra-broadband polarization splitter-rotator based on mode-evolution tapers and a mode-sorting asymmetric y-junction. *Optics Express*, 22(11):13565–13571, 2014.

[82] Junjia Wang, Ivan Glesk, and Lawrence R Chen. Subwavelength grating filtering devices. *Optics Express*, 22(13):15335–15345, 2014.

[83] Yun Wang, Wei Shi, Xu Wang, Zeqin Lu, Michael Caverley, Richard Bojko, Lukas Chrostowski, and Nicolas A. F. Jaeger. Design of broadband subwavelength grating couplers with low back reflection. *Optics Letters*, 40(20):4647–4650, 2015.

[84] Yun Wang, Xu Wang, Jonas Flueckiger, Han Yun, Wei Shi, Richard Bojko, Nicolas A. F. Jaeger, and Lukas Chrostowski. Focusing sub-

wavelength grating couplers with low back reflections for rapid prototyping of silicon photonic circuits. *Optics Express*, 22(17):20652–20662, 2014.

[85] Yun Wang, Han Yun, Zeqin Lu, Richard Bojko, Wei Shi, Xu Wang, Jonas Flueckiger, Fan Zhang, Michael Caverley, Nicolas A. F. Jaeger, et al. Apodized focusing fully etched subwavelength grating couplers. *Photonics Journal, IEEE*, 7(3):1–10, 2015.

[86] Michael R Watts, Jie Sun, Christopher DeRose, Douglas C Trotter, Ralph W Young, and Gregory N Nielson. Adiabatic thermo-optic mach–zehnder switch. *Optics Letters*, 38(5):733–735, 2013.

[87] MR Watts and HA Haus. Integrated mode-evolution-based polarization rotators. *Optics Letters*, 30(2):138–140, 2005.

[88] MR Watts, HA Haus, and EP Ippen. Integrated mode-evolution-based polarization splitter. *Optics letters*, 30(9):967–969, 2005.

[89] Zhe Xiao, Tsung-Yang Liow, Jing Zhang, Ping Shum, and Feng Luan. Bandwidth analysis of waveguide grating coupler. *Optics Express*, 21(5):5688–5700, 2013.

[90] Zhe Xiao, Feng Luan, Tsung-Yang Liow, Jing Zhang, and Ping Shum. Design for broadband high-efficiency grating couplers. *Optics Letters*, 37(4):530–532, 2012.

[91] Yule Xiong, J Gonzalo Wangüemert-Pérez, Dan-Xia Xu, Jens H Schmid, Pavel Cheben, and N Ye Winnie. Polarization splitter and rotator with subwavelength grating for enhanced fabrication tolerance. *Optics Letters*, 39(24):6931–6934, 2014.

[92] Dan-Xia Xu, Jens H Schmid, Graham T Reed, Goran Z Mashanovich, David J Thomson, Milos Nedeljkovic, Xia Chen, Dries Van Thourhout, Shahram Keyvaninia, and Shankar Kumar Selvaraja. Silicon photonic integration platform—have we found the sweet spot? *Selected Topics in Quantum Electronics, IEEE Journal of*, 20(4):189–205, 2014.

[93] Lin Xu, Xia Chen, Chao Li, and Hon Ki Tsang. Bi-wavelength two dimensional chirped grating couplers for low cost wdm pon transceivers. *Optics Communications*, 284(8):2242–2244, 2011.

[94] Xiaochuan Xu, Harish Subbaraman, John Covey, David Kwong, Amir Hosseini, and Ray T Chen. Complementary metal–oxide–semiconductor compatible high efficiency subwavelength grating couplers for silicon integrated photonics. *Applied Physics Letters*, 101(3):031109, 2012.

[95] Xiaochuan Xu, Harish Subbaraman, John Covey, David Kwong, Amir Hosseini, and Ray T Chen. Colorless grating couplers realized by interleaving dispersion engineered subwavelength structures. *Optics Letters*, 38(18):3588–3591, 2013.

[96] P Yeh and A Yariv. Photonics: Optical electronics in modern communication, 2007.

[97] Wangqing Yuan, Keisuke Kojima, Bingnan Wang, Toshiaki Koike-Akino, Kieran Parsons, Satoshi Nishikawa, and Eiji Yagyu. Mode-evolution-based polarization rotator-splitter design via simple fabrication process. *Optics Express*, 20(9):10163–10169, 2012.

[98] Han Yun, Wei Shi, Yun Wang, Lukas Chrostowski, and Nicolas A. F.

Jaeger. 2× 2 adiabatic 3-db coupler on silicon-on-insulator rib waveguides. In *Photonics North 2013*, pages 89150V–89150V. International Society for Optics and Photonics, 2013.

[99] Wissem Sfar Zaoui, Andreas Kunze, Wolfgang Vogel, Manfred Berroth, Jörg Butschke, Florian Letzkus, and Joachim Burghartz. Bridging the gap between optical fibers and silicon photonic integrated circuits. *Optics Express*, 22(2):1277–1286, 2014.

[100] Yi Zhang, Shuyu Yang, Andy Eu-Jin Lim, Guo-Qiang Lo, Christophe Galland, Tom Baehr-Jones, and Michael Hochberg. A compact and low loss y-junction for submicron silicon waveguide. *Optics Express*, 21(1):1310–1316, 2013.

[101] Qiuhang Zhong, Venkat Veerasubramanian, Yun Wang, Wei Shi, David Patel, Samir Ghosh, Alireza Samani, Lukas Chrostowski, Richard Bojko, and David V Plant. Focusing-curved subwavelength grating couplers for ultra-broadband silicon photonics optical interfaces. *Optics Express*, 22(15):18224–18231, 2014.

Appendix A

Publications

A.1 Book Chapters

1. Yun Wang and Lukas Chrostowki, Chapter 5.2, Grating Couplers, In *Silicon Photonics Design*, Lukas Chrostowski and Michael Hochberg, Cambridge Press, 2015. pp. 178-199.

A.2 Journal Publications

First Author

1. **Yun Wang**, Minglei Ma, Han Yun, Zeqin Lu, Xu Wang, Nicolas A. F. Jaeger, and Lukas Chrostowski. Ultra-Compact Sub-wavelength Grating Polarization Splitter-Rotator for Silicon-on-Insulator Platform *Photonics Journal, IEEE* 8(6), 2016.

2. **Yun Wang**, Zeqin Lu, Minglei Ma, Han Yun, Fan Zhang, Nicolas A. F. Jaeger, and Lukas Chrostowski. Compact Broadband Directional Couplers Using Sub-wavelength Gratings *Photonics Journal, IEEE* 8(3), 2016.

3. **Yun Wang**, Wei Shi, Xu Wang, Zeqin Lu, Michael Caverley, Richard Bojko, Lukas Chrostowski, Nicolas A. F. Jaeger. Design of Broadband

Sub-wavelength Grating Couples with Low Back Reflection. *Optics Letters* 40(20): 4647-4650, 2015

4. **Yun Wang**, Han Yun, Zeqin Lu, Richard Bojko, Wei Shi, Xu Wang, Jonas Flueckiger, Fan Zhang, Michael Caverley, Nicolas A. F. Jaeger, and Lukas Chrostowski. Apodized focusing fully etched sub-wavelength grating couplers. *Photonics Journal, IEEE*, 7(3), 2015

5. **Yun Wang**, Xu Wang, Jonas Flueckiger, Han Yun, Wei Shi, Richard Bojko, Nicolas A. F. Jaeger, and Lukas Chrostowski. Focusing sub-wavelength grating couplers with low back reflections for rapid prototyping of silicon photonic circuits. *Optics Express*, 22(17): 20652–20662, 2014.

Co-author

6. Han Yun, Zhitian Chen, **Yun Wang**, Jonas Flueckiger, Michael Caverley, Lukas Chrostowski, and Nicolas A. F. Jaeger. Polarization-rotating, Bragg-grating filters on silicon-on-insulator strip waveguides using asymmetric periodic corner corrugations *Optics Letters*, 40(23): 5578–5581, 2015.

7. Han Yun, **Yun Wang**, Fan Zhang, Zeqin Lu, Stephen Lin, Lukas Chrostowski, and Nicolas A. F. Jaeger. Broadband 2x2 Adiabatic 3-dB Coupler using Silicon-on-Insulator Sub-wavelength Grating Waveguides *Optics Letters*. 41(13): 3041–3044, 2016.

8. Zeqin Lu, Han Yun, **Yun Wang**, Zhitian Chen, Fan Zhang, Nicolas A. F. Jaeger, and Lukas Chrostowski. Broadband silicon photonic

directional coupler using asymmetric-waveguide based phase control. *Optics Express*, 23(3):3795–3808, 2015.

9. Zeqin Lu, **Yun Wang**, Fan Zhang, Nicolas A. F. Jaeger, and Lukas Chrostowski. Wideband silicon photonic polarization beamsplitter based on point-symmetric cascaded broadband couplers. *Optics Express*, 23(23):29413–29422, 2015.

10. Ahmadreza Farsaei, **Yun Wang**, Reza Molavi, Mohammad Beikahmadi, Amir Hossein Masnadi Shirazi, Michael Caverley, Hasitha Jayatilleka, Lukas Chrostowski, Shahriar Mirabbasi, A Review of Wireless Photonic Systems: Design Methodologies and Topologies, Constraints, Challenges, and Innovations in Electronics and Photonics. *Journal of Optics Communication*, 373: 16-34, 2015 (Invited).

11. Zhitian Chen, Jonas Flueckiger, Xu Wang, Fan Zhang, Han Yun, Zeqin Lu, Michael Caverley, **Yun Wang**, Nicolas A. F. Jaeger, and Lukas Chrostowski. Spiral Bragg grating waveguides for TM mode silicon photonics. *Optics Express*, 23: 25295–25307, 2015

12. Raphael Dube-Demers, Jonathan St-Yves, Antoine Bois, Qiuhang Zhong, Michael Caverley, **Yun Wang**, Lukas Chrostowski, Sophie LaRochelle, David Plant, Wei Shi. Analytical Modeling of Silicon Microring and Microdisk Modulators with Electrical and Optical Dynamics. *Journal of Lightwave Technology, IEEE*, 33: 4240-4252,2015

13. Qiuhang Zhong, Venkat Veerasubramanian,**Yun Wang**, Wei Shi, David Patel, Samir Ghosh, Alireza Samani, Lukas Chrostowski, Richard Bojko, and David V Plant. Focusing-curved subwavelength grating cou-

plers for ultra-broadband silicon photonics optical interfaces. *Optics Express*, 22(15):18224–18231, 2014.

14. Xu Wang, **Yun Wang**, Jonas Flueckiger, Richard Bojko, Amy Liu, Adam Reid, James Pond, Nicolas A. F. Jaeger, and Lukas Chrostowski. Precise control of the coupling coefficient through destructive interference in silicon waveguide bragg gratings. *Optics Letters*, 39(19):5519–5522, 2014.

A.3 Conference Proceedings

1. **Yun Wang**, Han Yun, Zeqin Lu, Nicolas A.F. Jaeger, and Lukas Chrostowski, State-of-the-art Sub-wavelength Grating Couplers for Silicon-on-insulator Platform In *IEEE, Canadian Conference on Electrical and Computer Engineering*, (Invited) 2016.

2. **Yun Wang**, Han Yun, Zeqin Lu, Nicolas A.F. Jaeger, and Lukas Chrostowski, Sub-wavelength Grating Components for the Silicon-on-insulator Platform In *International Conference on Metamaterials, Photonic Crystals and Plasmonics*, (Invited) 2016.

3. **Yun Wang**, Han Yun, Nicolas A.F. Jaeger, and Lukas Chrostowski, Broadband Bidirectional Vertical Grating Coupler In *Proc. Optical Fiber Communications (OFC) Conference*, 2016.

4. Zeqin Lu, Minglei Ma, Han Yun, **Yun Wang**, Nicolas A. F. Jaeger, and Lukas Chrostowski. Silicon Photonic Polarization Beamsplitter and Splitter-rotator for On-chip Polarization Control. In *IEEE International Conference on Group IV Photonics (GFP), 2016* (Invited).

5. Minglei Ma, Kyle Murray, Mengyuan Ye, Stephen Lin, Zeqin Lu, Han Yun, **Yun Wang**, Richy Hu, Nicolas A.F. Jaeger, and Lukas Chrostowski. Sub-wavelength Grating Components for the Silicon-on-insulator Platform In *CLEO: Science and Innovations*, pages SM1I–6. Optical Society of America, 2016.

6. **Yun Wang**, Han Yun, Zeqin Lu, Richard Bojko, Fan Zhang, Michael Caverley, Nicolas A. F. Jaeger, and Lukas Chrostowski. Apodized focusing fully etched sub-wavelength grating couplers with ultra-low reflections. In *CLEO: Science and Innovations*, pages SM1I–6. Optical Society of America, 2015.

7. **Yun Wang**, Stevan S Djordjecvic, Jin Yao, John E Cunningham, Xuezhe Zheng, Ashok V Krishnamoorthy, Michael Muller, Markus-Christian Amann, Richard Bojko, Nicolas A. F. Jaeger and Lukas Chrostowski. Vertical-cavity surface-emitting laser flip-chip bonding to silicon photonics chip. In *Optical Interconnects Conference (OI), 2015 IEEE*, pages 122–123. IEEE, 2015.

8. Han Yun, Jonas Flueckiger, Zhitian Chen, **Yun Wang**, Lukas Chrostowski, and Nicolas A. Jaeger. A Wavelength-Selective Polarization Rotating Reflector using a Partially-Etched Asymmetric Bragg Grating on an SOI Strip Waveguide. In *IEEE International Conference on Group IV Photonics (GFP), 2015*

9. Han Yun, Zeqin Lu, **Yun Wang**, Wei Shi, Lukas Chrostowski, and Nicolas A. F. Jaeger. 2x2 Broadband Adiabatic 3-dB Couplers on SOI Strip Waveguides for TE and TM modes. In *International conferences on Laser and Electro-Optics (CLEO), 2015.*

10. Zeqin Lu, Han Yun, **Yun Wang**, Zhitian Chen, Fan Zhang, Nicolas A. F. Jaeger, and Lukas Chrostowski. Asymmetric-waveguide-assisted 3-dB Broadband Directional Coupler. In *International conferences on Laser and Electro-Optics (CLEO), 2015.*

11. Zhitian Chen, Jonas Flueckiger, Xu Wang, Han Yun, **Yun Wang**, Zeqin Lu, Fan Zhang, Nicolas A. F. Jaeger, and Lukas Chrostowski. Bragg Grating Spiral Strip Waveguide Filters for TM Modes. In *International conferences on Laser and Electro-Optics (CLEO), 2015*

12. Fan Zhang, Han Yun, Valentina Donzella, Zeqin Lu, Yun Wang, Zhitian Chen, Lukas Chrostowski, and Nicolas A. F. Jaeger. Sinusoidal Anti-coupling SOI Strip Waveguides. In *International conferences on Laser and Electro-Optics (CLEO), 2015*

13. **Yun Wang**, Jonas Flueckiger, Han Yun, Richard Bojko, Nicolas A. F. Jaeger, Lukas Chrostowski, et al. Focusing sub-wavelength grating coupler. In *Photonics Conference (IPC), 2014 IEEE*, pages 552–553. IEEE, 2014.

14. J Niklas Caspers, **Yun Wang**, Lukas Chrostowski, and Mohammad Mojahedi. Active polarization independent coupling to silicon photonics circuit. In *SPIE Photonics Europe*, pages 91330G–91330G. International Society for Optics and Photonics, 2014.

15. Qiuhang Zhong, Wei Shi, **Yun Wang**, Lukas Chrostowski, and David V Plant. An ultra-broadband fiber grating coupler with focusing curved subwavelength structures. In *Proc. Optical Fiber Communications (OFC) Conference*, 2014.

16. Raphal Dub-Demers, Jonathan St-Yves, Antoine Bois, Qiuhang Zhong, Michael Caverley, **Yun Wang**, Lukas Chrostowski, Sophie LaRochelle, David Plant, and Wei Shi, Analytical Modeling for Ultra-High-Speed Microring Modulators with Electrical and Optical Dynamics in *European Conference on Optical Communication (ECOC)*, 2014

17. Lukas Chrostowski, Xu Wang, Jonas Flueckiger, Yichen Wu, **Yun Wang**, Sahba Talebi Fard, Impact of fabrication non-uniformity on chip-scale silicon photonic integrated circuits. In *Proc. Optical Fiber Communications (OFC) Conference*, 2014.

18. Michael Caverley, Hasitha Jayatilleka, **Yun Wang**, Nicolas. A. F. Jaeger, and Lukas Chrostowski, Microring Modulator Using Drop-Port Phase Interference. In *Photonics Conference (IPC), 2014 IEEE*, pages 613–614. IEEE, 2014.

19. Xu Wang, Michael Caverley, Jonas Flueckiger, **Yun Wang**, Nicolas A. F. Jaeger, and Lukas Chrostowski, Silicon Photonic Bragg Grating Modulators. In *Photonics Conference (IPC), 2014 IEEE*, pages 35. IEEE, 2014.